Jülich Centre for Neutron Science JCNS and Peter Grünberg Institut PGI

JCNS-2&PGI-4: Scattering Methods

Microstructure and elastic constants of a martensitic steel applied in the very high cycle fatigue region

Master thesis

Materials Science of Steels
Metallurgical Engineering
RWTH Aachen University, Germany

Written by
Fangtian Deng (314949)

Jülich, September 2014

IEHK, RWTH-Aachen

This master thesis is written on my own without any help and that I have quoted properly and that everyone involved has the right to look through this thesis.

Signature: ________________________

Place, Date: ________________________

This work was supervised by:

1. Prof. Dr.-Ing. Wolfgang Bleck (internal)
2. Karl Gillner (internal)
3. Dr. Klobes Benedikt (external)

Contents

1 Summary

This thesis presents an investigation of special features of the microstructure of certain structural materials, some of which are applied in wind and gas turbines under a certain fatigue load. For these structural materials, the durability and reliability of engineering properties are supposed to be two of the most important safety parameters. These components function mostly under not only high load, but also under a continuous repetition of loading. In these circumstances, cracks occur, develop und eventually turn into irreversible damages very easily even under loading stresses, which are much lower than the material yield strength. This behavior is called mechanical fatigue [Ble12].

Apart from sample dimensions and stress amplitude, the number of fatigue cycles also plays a critical role in changing significantly these materials characteristics, such as yield strength and shear strength. Generally, the mechanical fatigue is mainly divided into three regimes: low cycle fatigue (LCF, up to 10^6 cycles to failure), high cycle fatigue (HCF, 10^6 to 10^8 cycles to failure) and very high cycle fatigue (VHCF, more than 10^8 cycles to failure) [Mar03].

Since the capital lost and life danger caused by other fracture mechanism under very high cycle is inestimable, the fatigue failure now has become a major concern in engineering research field. Therefore, steels, which can be applied in the VHCF (VHCF-Very High Cycle Fatigue, more than 10^8 cycles to failure) regime, are of interest, as they might be helpful to increase material lifetime and maintenance periods, thus contributing to energy efficiency.

In this thesis, the martensitic 12% structural steel X10CrNiMoV12-2-2, i.e. about 12 wt-% Cr, 2.5 wt-% Ni and 1.75 wt-% Mo, which is usually processed into the turbine blades for power plant applications [Til13], is studied in the VHCF regime. Using small angle neutron scattering (SANS), the incipient fatigue processes due to cyclic loading, especially nanometer sized cracks formation in X10CrNiMoV12-2-2 steel, are investigated non-destructively in real specimens. Moreover, microstructural changes during crack formation will be further assessed with Grazing-incidence small angle X-ray scattering (GISAXS). Meanwhile with the resonant ultrasound spectroscopy, the elastic

constants of specimens in different crack formation stages are measured in order to find out the relationship between elastic constants and load cycle numbers. Additionally, more methods of material characterization, e.g. Mössbauer spectroscopy, are applied to study this steel in different stages.

The specimens' microstructures transformations are followed and recorded, when the specimens are through different load cycle numbers in the VHCF regime. When the specimen is with the cycle number larger than 2.7×10^7, some conclusions can be reached with SANS method. In SANS analysis, not only the parameters of the crack geometries but also an overview on microstructural changes are attained. Aspect of the microstructure of original specimen is significantly changed with respect to those with certain cycle number, since under 2.7×10^7 load cycle the SANS profile shows a big different from that of "pristine" steel. Furthermore, the SANS curve are fitted to attain specific surface areas associated with the microstructure, including fatigue effects. Since SANS is sensitive only to a certain length scale as determined by accessible Q or angular range, attained parameters cannot be exactly describe the real situation when the sizes of researched subjects are out of the length scales limitation. However, the decline of the specific surface area values indicate that void coalescence exists in the procedure of forming a crack during the fatigue test. Due to only few examples for investigations of early stage crack propagation in fatigue test using SANS and less investigation with respect to steel behavior in fatigue test using SANS, the conclusion derived from SANS is mostly based on assumptions and real mechanisms are difficult to discover.

Furthermore, the elastic moduli measured from ultrasonic spectroscopy prove the inverse trend for load cycle number. Between 0 and 2.6×10^7 load cycle, the higher cycle number the sample goes through, the bigger the elastic moduli's value is. This phenomenon can be explained with the strain hardening mechanism. Additionally, the shear moduli trends to reduce earlier than elastic moduli, in the sample under 2.6×10^7 load cycle, the decline trend of shear moduli is already observed in this work.

2 Introduction

In structural material application cases, under a series of cyclic load, cracks occur, develop und eventually turn into irreversible damage very easily even under a loading stress, which is much lower than this material's yield strength. This behavior is called fatigue [Ble12]. The fatigue fracture behavior of materials under cyclic loading causes a significant decrease of the energy efficiency in industries as devices need to be maintained. In reality, most applied loads for structural materials, especially iron and steel, possess not only high amplitude but also high repetition numbers. In general, the material damages are caused by repeated load which a high cycle, which happens more often than merely a high unrepeated load. Therefore, the fatigue behavior, not only its macro-structural deformation but also its microstructural transformation are attracting more and more attention in the public as well as in research.

Besides sample dimensions and some other loading variables, the number of fatigue plays a critical role in changing significantly these materials characteristics, such as strength. Here the microstructural transformations in the regime of very high cycle fatigue (VHCF, more than 10^8 cycles to failure) are of interest in this work.

In this study, the structural steel X10CrNiMoV12-2-2, i.e. about 12 wt-% Cr, 2.5 wt-% Ni and 1.75 wt-% Mo, which is typically supposed for turbine blade application, is studied within VHCF regime. Further, the early stages of nanometer sized fatigue crack formation in VHCF steel are investigated with small angle neutron scattering non-destructively in real specimens. Particularly, this thesis aims to investigate whether these early stages can be probed by neuron scattering techniques at all. In that way, the investigated micro-structure will be further qualified with grazing-incidence small-angle X-ray scattering and build a relationship with the relevant material properties. Meanwhile the relationship between load cycle and elastic constant of the specimen is investigated with the method of resonant ultrasound spectroscopy. Additionally, further methods of material characterization, e.g. Mössbauer spectroscopy, will be applied and learned in order to characterize the steel under investigation.

In this work, main tasks include:

1. Analysis and evaluation of small angle neutron scattering
2. Prepare specimen for the grazing-incidence small-angle X-ray scattering and conduct the experiment
3. Process specimen for the resonant ultra-sound spectroscopy and conduct the experiment
4. Correlation micro-structure and elastic constant with the relationship state
5. Overview on chemical components by means of Mössbauer spectroscopy

Through these measurements, the microstructure properties can be measured and determined, furthermore through the literature investigation, the relevant physical mechanism and other theories will be also discussed in detail in the work, these measured phenomena can be explained, specially focusing on crack formation at the early stage in the microstructure.

3 State of the art

For steels, which are applied in wind and gas turbines, the resistance against fatigue of these devices is supposed to be one of the most important safety parameters. Such components are mostly applied not only under high load, but also under a continuous repetition of loading. In these circumstances, even when the loading stress is much lower than under this material yield strength, cracks might propagate und turn into the irreversible damages, which can become a sudden catastrophe. This behavior is called mechanical fatigue [Ble12].

There are various factors which affect material fatigue behavior, the number of fatigue is one of these factors, and can influence significantly these materials properties. In general, the mechanical fatigue is divided into three regimes (see **image 1**): low cycle fatigue (LCF, up to 10^6 cycles to failure), high cycle fatigue (HCF, 10^6 to 10^8 cycles to failure) and very high cycle fatigue (VHCF, more than 10^8 cycles to failure) [Mar03].

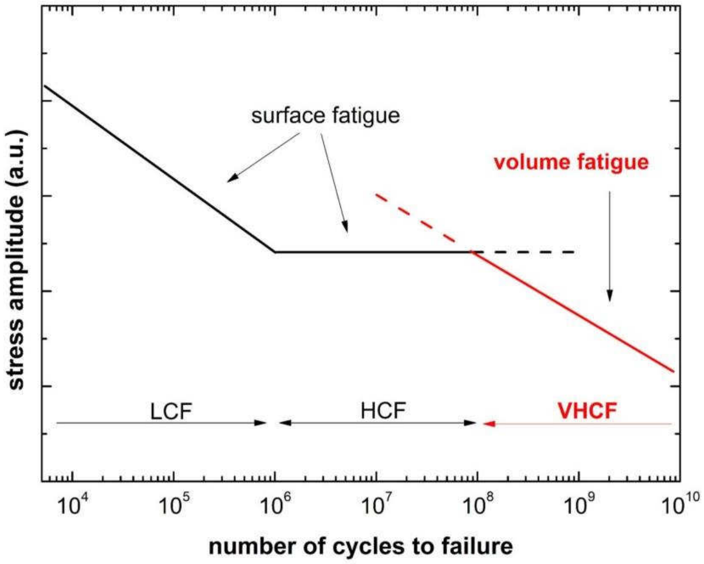

Image 1: Stress amplitude vs. number of cycles to failure for typical steels

However, fatigues with a change of crack initiation mechanism can occur to specimens when fatigue tests are carried out at even higher numbers of load cycles. While the LCF as well as HCF fatigue usually occurs at the surface, fatigue in the VCHF regime is initiated within the material matrix, especially at oxide or intermetallic inclusions [Bay06,Wang02]. Therefore, the initial stages of the VHCF regime, i.e. the early stages of crack initiation are hard to investigate. Particularly, as these processes occur inside the volume of the material, “unconventional” methods of void detection could contribute significantly to a further understanding of VHCF.

In this work, the microstructure transformation of the martensitic steel applied in the VCHF regime, particularly crack formation due to the fatigue behavior, is of interest. Here the structural steel X10CrNiMoV12-2-2 is chosen to study the microstructural transformation. In the following part, the microstructural and mechanical properties of this material and the fatigue test parameters will be described.

3.1 Materials

Here the structural steel X10CrNiMoV12-2-2, i.e. about 12 wt-% Cr, 2.5 wt-% Ni and 1.75 wt-% Mo, which is usually applied in wind and gas turbines, is studied.

3.1.1 Chemical Composition

Steel X10CrNiMoV12-2-2 chemical composition is shown in **table 1**, referred to the literature [Til13].

Table 1: Chemical composition of X10CrNiMoV12-2-2

Element	C	Cr	Ni	Mo	Mn	V	Si
Weight-%	0.117	11.4	2.70	1.64	0.70	0.31	0.23

3.1.2 Heat treatment

The steel was hardened by annealing at 1040 ℃ for 60 min and subsequently cooled by compressed air. In this way, a microstructure with a relatively high martensitic component microstructure is obtained, In order to relieve the inner stress, this material was subsequently tempered at 660 ℃ for 3 h followed by annealing at 640 ℃ for 4 h., The heat treatment scheme, see **image 2**, ended with very slow furnace cooling [Til13].

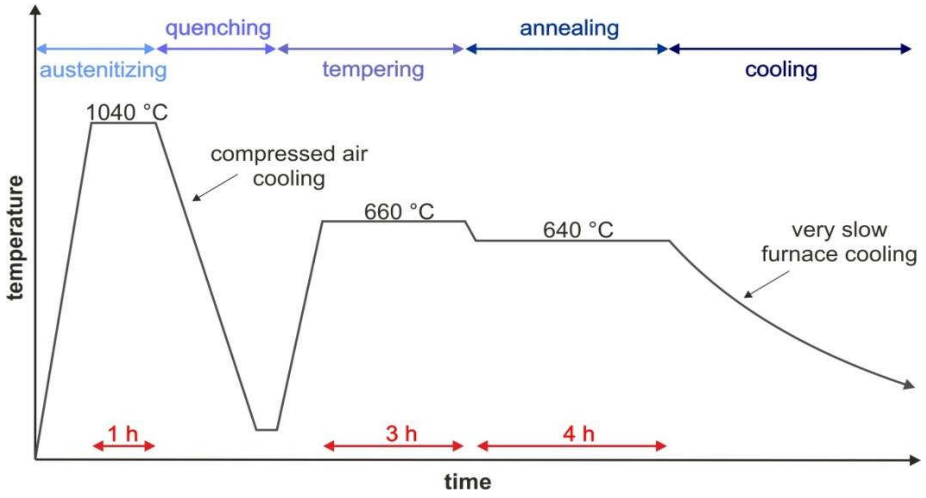

Image 2: The heat treatment scheme of X10CrNiMoV12-2-2 Steel

The resulting highly tempered martensitic microstructure has finely distributed Cr-carbides with diameters of around 100 nm along the martensite laths and the former austenite grain boundaries [Til13], which will be verified using Mößbauer spectroscopy (referred to section 4.2).

3.1.3 Mechanical Properties

Precipitation-hardening caused by the finely distribution of Cr-carbides results in high ultimate tensile strength combined with a relatively high elongation at fracture (see **table 2**).

Table 2: Mechanical properties of X10CrNiMoV12-2-2 at room temperature [Til13]

Vickers hardness	334 HV
Yield strength	843 MPa
Ultimate tensile strength	1001 MPa
Elongation at fracture	17.7 %
Contraction at fracture	58 %
Young´s Modulus	213 GPa

3.2 Fatigue testing

3.2.1 Testing system

The Ultrasonic Fatigue Testing Equipment (UFTE) was in this fatigue testing developed and manufactured by Boku Wien company. An Instron 5967 load frame was attached to this equipment. As a benefit, the instrument was able to apply this fatigue tests with superimposed mean stresses. The experimental setup is similar to that described in [Bat97]. The UFTE system working principle and working condition can be found in detail in the literature [Til13].

3.2.2 Samples for the fatigue testing

Subsequently, cylindrical rods were eroded from the blade root by electro-discharge-machining and turned to the final specimen geometry with cylindrical gauge length and a diameter of 3 mm. **Image 3** shows the specimen shape for tests with superimposed mean stresses (R > 0) [Til13].

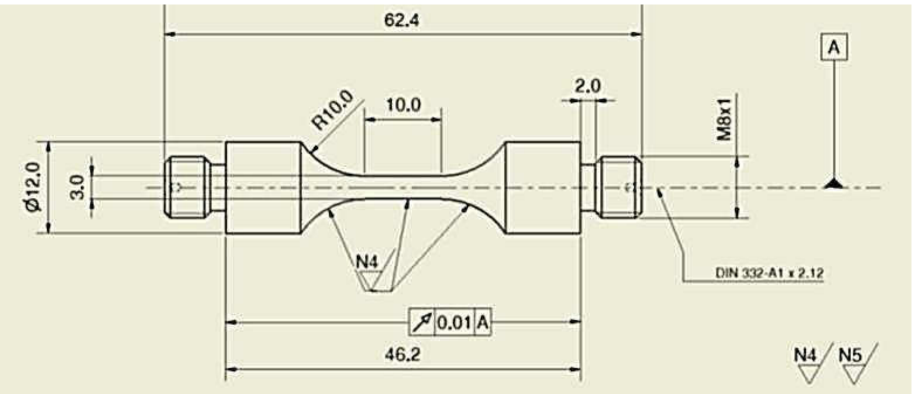

Image 3: Specimen geometry for R > 0 fatigue tests. [Til13]

Finally, the samples were ground with SiC abrasive paper and subsequently mechanically polished.

In **image 4**, the relevant fatigue data of X10CrNiMo12-2-2 are shown with load ratios ranging between R = -1 and R = 0.7. In the S-N curves, no “two step” behavior indicating separate fatigue limits for surface and sub-surface cracks could be observed.

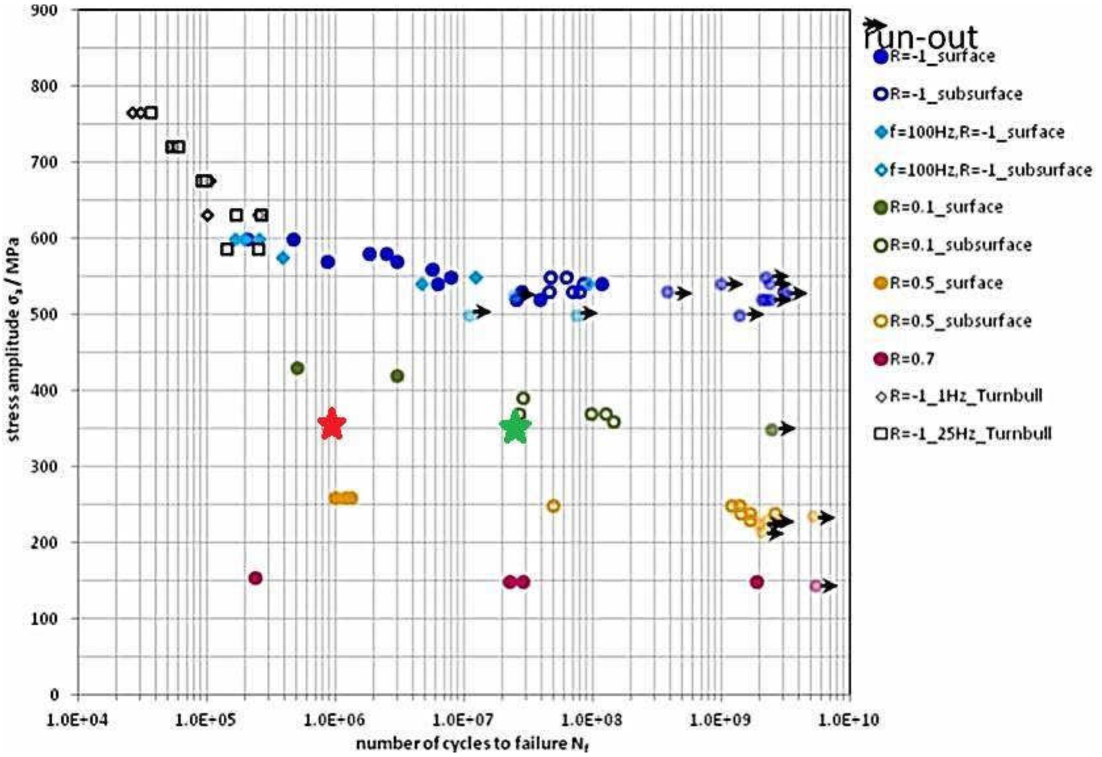

Image 4: Stress amplitude vs. number of cycles to failure for load ratios R = -1, 0.1, 0.5 and 0.7 at RT. [Til13]

In **image 4**, filled symbols mark fractures originating from the surface (persistent slip bands or surface inclusions) and open symbols indicate volume fractures of subsurface inclusions. A quite narrow transition band from surface to internal fractures between approximately 2×10^7 and 4×10^7 load cycles is shown. Furthermore, for R = 0.1, the fatigue strength was 350 Mpa from the literature data by Tilmann et al. [Til13]

In this work, three samples are chosen to be investigated by using the following measurements. All the specimens were prepared in the geometry, which can be present in **image 3**. A specimen, which was not loaded, is labeled with “pristine”, one other specimen, which was loaded with R = 0.1, σ_a = 370 Mpa, at 10^6 load cycles, is marked with “10 to 6” One of these specimens, the other specimen, which was loaded with R = 0.1, σ_a = 370 Mpa, at 2.691×10^6 load cycles, labeled with “fail”. Due to a subtle change of sample length in tensile stress direction, crack formation, i.e. fatigue failures, is supposed to occur in the “fail” specimen with deformation. And then the fatigue mechanism is illustrated later.

3.2.3 Fatigue failures

For fatigue failures developed on the steel specimen there are some arguments with different views. One view, which is accepted commonly in science field, is that fatigue failure is supposed to start at dislocations where the stresses are concentrated [Dav01]. And then the failures are initiated mainly by the shear movement along the slip planes. After a certain number of cyclic loading, the intrusions and extrusions, which are generated by the slipping, result later in cracks. Subsequently, the cracks will propagate along the slip planes, running to the inside of the fracture phase. Finally, the cracks will be present perpendicular to the principal normal stress (see **image 5**).

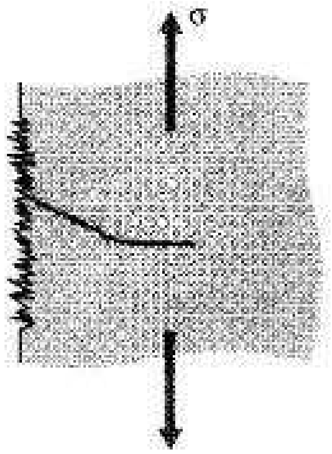

Image 5: Model of fatigue crack initiation [Dav01]

Moreover, the cyclic loading number plays an important role in the fatigue position. In literature [Bay06,Wan02] , one view is presented, that fatigue in the VCHF regime starts usually at oxide or intermetallic inclusions within the steel matrix (see **image 6**), comparing to the surface fatigue position with load cycles of LCF (low cycle fatigue) and HCF (high cycle fatigue).

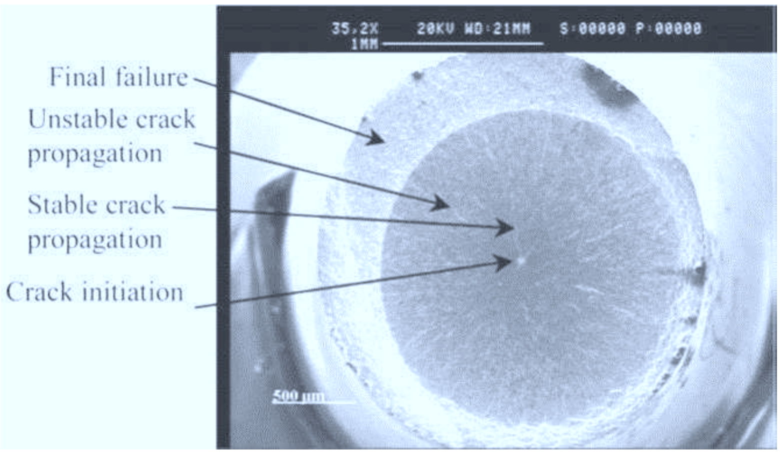

Image 6: Overview of the gigacycle fatigue fracture surface [Wan02].

According to literature [Wan02], for S-N curve of high strength steels there is a plateau between 10^6 and 10^8 cycles and a drop in gigacycle regime, i.e. high than 10^7 or 10^8 cycles. In his work, subsurface crack initiation mechanism for HCF steels is confirmed. However, there are only few studies are on relevant cracks initiation mechanisms in VHCF steel [Wan02].

In order to determine the component phases and their corresponding amount in the steel, the Mössbauer spectroscopy was applied to analyze the phases. Here the physical theory and its application will be introduced.

3.3 Mössbauer spectroscopy

3.3.1 Fundamental principles of Mössbauer spectroscopy

The recoil-free resonance fluorescence and absorption of γ-photons, which occurs in certain atomic nuclei, is the principle of Mössbauer spectroscopy. Mössbauer spectroscopy illustrates details in the electronic, magnetic, geometric, or defect structure as well as in lattice vibrations. The item “Mössbauer Effect” is the name for recoilless γ-ray emission and absorption. After its discoverer Rudolph Mössbauer, who first observed the effect in 1957 [Rud14] and received the Nobel Prize in Physics in 1961 for his work [Fra62].

A free nucleus recoils during emission or absorption of a γ-ray. Due to conservation of momentum the recoil is associated with a certain energy E. This recoil is shown schematically in **image 7**. The emitted γ-ray has an energy expressed below:

$$E = E_0 - E_R \tag{3.3.1}$$

Where E_0 is the energy between the first excited state and the ground state of the nucleus and E_R is the recoil energy.

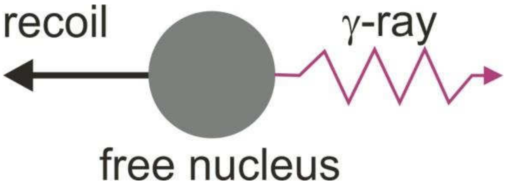

Image 7: Recoil of free nuclei in emission of a $\boldsymbol{\gamma}$-ray

The movement of the atoms in a crystal with random thermal motion results into γ-ray energy with a spread of values E_D, due to the Doppler effect. The resulting γ-ray energy profile is shown in **image 8**. The red-shaded area stands for the overlapping energy from two different energies, producing a resonant signal. This area is shown exaggerated as in reality it is extremely small, a millionth or less of the γ-rays are in this region [Fra62].

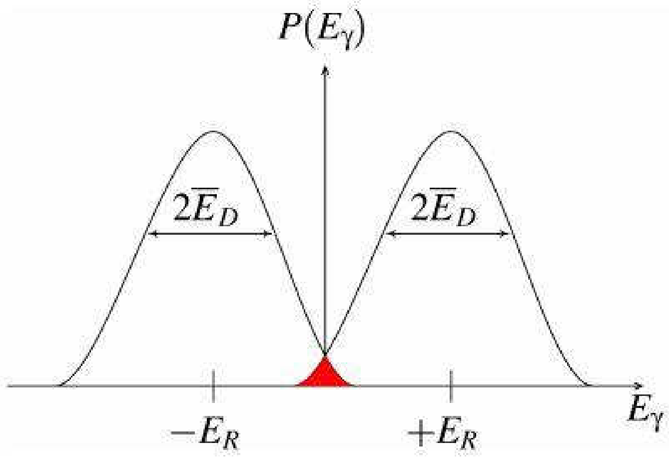

Image 8: Resonance absorption (red) of $\boldsymbol{\gamma}$-rays emitted from a recoiling, free nucleus.

However, the effective mass of the nucleus is much greater when the atoms are embedded in a solid matrix, which is what Mössbauer had firstly discovered. The recoiling mass then presents the mass of the whole system, which leads to a very low value of E_R.

$$E_R = \frac{{E_r}^2}{2Mc^2} \tag{3.3.2}$$

Where E_r is the energy of the nuclear transition and of the γ-ray and M is the mass of the solid.

Upon emission and absorption of γ-rays the recoil effect will be virtually eliminated: a recoil-free event. In this case, if the emitting and absorbing nuclei are in a solid matrix the emitted and absorbed γ-ray are of the same energy, which is referred to as a resonance absorption phenomenon [Gol68].

When emitting and absorbing nuclei are in an identical environment, then the transition energies are exactly identical, which results in a spectrum as shown in **image 9**: a single absorption curve.

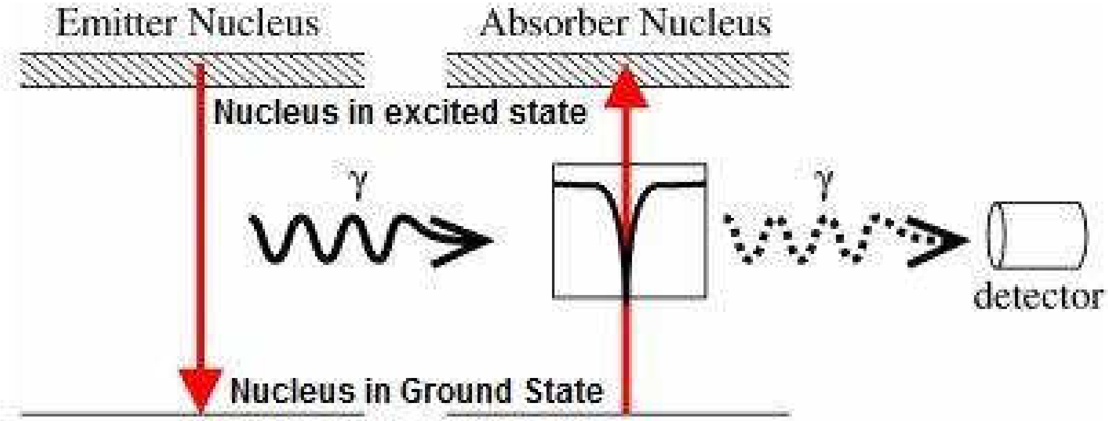

Image 9: Simple Mössbauer spectrum from recoilless nuclear resonance absorption and fluorescence of γ-radiation.

Using the Doppler effect, the frequency of a wave changes for a detector moving relative to the wave source. In that way the obtained energy of the investigated wave can be adjusted through relative movement, which is the Doppler effect Therefore, in order to find the hyperfine interactions, the γ-ray source can be periodically moved towards and away from the researched specimen. In order to make the record more practical and convenient, the energy scale of a Mössbauer spectrum is thus calculated, exchanged and presented in terms of the source velocity, as shown in **image 10**.

Based on the Doppler effect, the energy of the γ-ray can be further modulated in very small increments using a mechanically oscillating source. The energy of a nuclear transition in the absorber can match precisely to the modulated γ-ray energy. When the γ-rays are resonantly absorbed, then an absorption peak will be recorded. In **image 10** the absorption peak occurs at 0 mm/s with identical source and absorber.

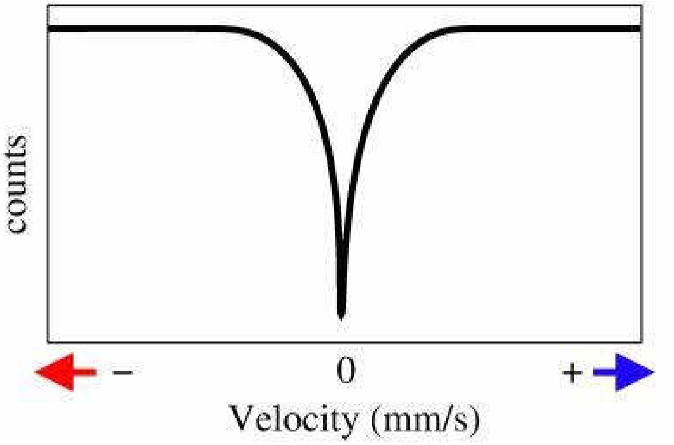

Image 10: Simple spectrum showing the velocity scale due to the motion of source relative to the absorber

The energy levels in the absorbing nuclei experience their different environments. The observables of Mössbauer spectroscopy can thus be classified into three main classes: the isomer shift, quadrupole splitting and magnetic splitting.

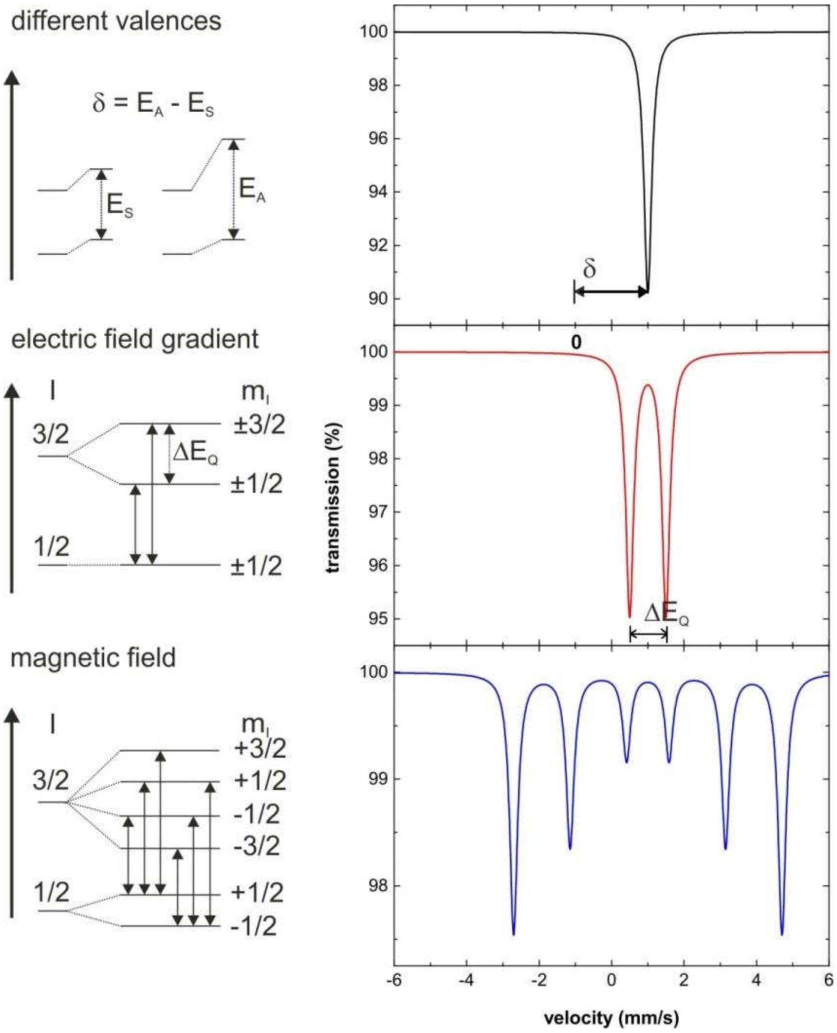

Image 11: The schema of the isomer shift, quadrupole splitting and magnetic splitting.

Image 11 shows a schema of source and absorber atoms in different local environment with different nuclear energy levels. In the first transmission spectrum, there is a shift from zero velocity regarding to isomer shift. In the second profile, the nuclear spin of the Mössbauer nucleus is represented with I label, i.e. 1/2 and 3/2 and its sublevels m_I. The nuclear quadrupole moments will interact with a potential due to the electric field gradient, which leads to splitting of the nuclear energy levels, as shown in the middle of **Image 11**. Here this phenomenon is referred to quadrupole splitting. The third sextet spectrum is yielded with Zeeman splitting, when a magnetic field is present at the nucleus and lifts the degeneracy of the m_I starts completely. More details are illustrated below.

Isomer Shift:

The volume of the nucleus and the electron charge density due to s-electrons give rise to the isomer shift phenomenon. Therefore, the difference in the s-electron difference between the source and absorber thus result in a shift in the resonance energy of the transition. This shifts the whole spectrum away from the peak at 0 mm/s (see **image 11**), whose offset degree is depending on the s-electron density. And the isomer shift is given by the following expression:

$$\delta = E_A - E_S = C\{|\Psi(0)|_A{}^2 - |\Psi(0)|_S{}^2\}(R_e{}^2 - R_g{}^2) \tag{3.4.1}$$

Where $E_A - E_S$ stands for the difference of the transition energy, $|\Psi(0)|_A{}^2 - |\Psi(0)|_S{}^2$ is the difference of the electron density, R_e is the nuclear radius of the source, R_g is the nuclear radius of the absorber, C is a proportionality constant.

The $|\Psi(0)|^2$ primarily comes from the ability of penetrating the nuclear field, which is mainly contributed by the s-electrons. Nevertheless, the shift depend indirectly on p-, d- and f-electrons due to their shield effects, such as oxidation state given by the valence electrons in these not s-orbitals.

Quadrupole Splitting

Nuclei with an angular momentum quantum number I > 1/2 have a non-spherical charge distribution [Phi11]. This charge distribution result in a nuclear quadrupole moment. Moreover, a non-spherical electronic charge distribution leads to an electric field gradient, splitting the nuclear energy levels due to the interaction with the nuclear quadrupole moment. The charge distribution is characterised by a single quantity referred to as the Electric Field Gradient (EFG, V_{zz}). Take an example, an isotope with a I = 3/2 excited state, such as ^{57}Fe, the excited state is split into two substates m_I = ±1/2 and m_I = ±3/2. This is shown in **image 11**, giving a spectrum with two peaks, which is expressed and quantified later with “doublet” formula. And the eigenvalues of quadrupole splitting is given by the following expression:

$$E_Q(I,m_I) = \frac{eQV_{zz}}{4I(2I-1)}[3m_I{}^2 - I(I+1)](1+\frac{\eta^2}{3})^{\frac{1}{2}} \quad (3.4.2)$$

where $m_I = +I, +I\text{-}1, \ldots, \text{-}I$, V_{zz} is the main component of the electric field, Q is the nuclear quadrupole moment and η is the so called asymmetry term [Phi11].

Magnetic Splitting

A dipolar interaction occurs between the nuclear moment, which is associated with its spin and the magnetic field, i.e. a Zeeman splitting due to the presence of a magnetic field. There are many sources of magnetic fields that can have an effect on the nucleus. The total effective magnetic field at the nucleus, B_{eff} is given by:

$$B_{eff} = (B_{contact} + B_{orbital} + B_{dipolar}) + B_{applied} \quad (3.4.3)$$

The first three terms are produced by the atom's own not completely filled electron shells. This magnetic field splits nuclear levels with a spin of I into $(2I+1)$ sub-states m_I. This is shown in **image 11** for ^{57}Fe. Transitions between the excited state and ground state can only occur where m_I changes by 0 or 1. This gives six possible transitions for a 3/2 to 1/2 transition, yielding a sextet.

According to literature [Fra62], the corresponding definitions and information are summarized and listed below in **table 3**.

Table 3: Hyperfine Interactions and Mössbauer Parameters

Type of Interaction	**Interaction partner**	**Mössbauer Parameter**	**Information for Chemistry**
Electric monopole interaction	Between nucleus and electrons with respect to charge density	Isomer shift δ (mm/sec)	• Oxidation state • Electronegativity of ligands • Character of bonds • Spin state (HS, IS, LS)

Electric quadrupole interaction	Between nuclear quadrupole moment and inhomogeneous electric field	Quadruple splitting ΔE_Q (mm/sec)	• Molecular symmetry • Oxidation state • Character of bonds • Spin state (HS, IS, LS)
Magnetic dipole interaction	Between magnetic dipole moment and magnetic field	Magenetic splitting ΔE_M (mm/sec)	• Magnetic interactions e.g. ferromagnetism, antiferromagnetism

Mössbauer parameters in the fitting formula will be fitted and special values of these parameters can stand for special phase. For example, $Fe(OH)_2$ is characterized with isomer shift δ of 1.18, quadruple splitting ΔE_Q of 2.92 and no magnetic splitting component [Sei98].

3.3.2 Practical aspects of the method

In this study, both conventional Transmission Mössbauer spectroscopy (TMS) and Conversion Electron Mössbauer Spectroscopy (CEMS) were applied to analyze the relevant phenomena of the steel under investigation.

For TMS, the working principle is mostly based on the description in the previous section on Mössbauer spectroscopy. In general, it is used to provide the information about the phases in matrix and their transformation during the thermal treatment. Through detecting the change of the lattice the electric quadruple splitting (QS), the phase transformation can be followed [Lar06]. In most cases, the powdered form is used in order to record the transmission of Mössbauer quanta. Moreover, in this work, only the phase record and analysis were carried out.

In CEMS theory, the energy of the nuclear excited state is transferred to the atomic electrons the electrons. In that way, electrons leave the atom or rearrange their atomic states to emit an X-ray. These electrons and conversion X-ray can be used for measuring a Mössbauer spectrum to analyze surface phenomena [Fal94,Kru97], which in this work complement the information obtained by TMS.

3.4 Small angle neutron scattering (SANS)

The small-angle neutron scattering (SANS) technique can be applied to investigate the structure of a material on length scale from the $\dot{A}$ to the μm regime. SANS is used to study the details of the particles or voids dispersed in homogeneous medium, especially the information on shapes and sizes. However, small angle neutron scattering is supposed to be one of the very few damage-free methods with which nanometer sized cracks can be investigated within the material, i.e. without the necessity for a cross section preparation due to the long penetration length of neutrons in matter.

3.4.1 Nuclear and magnetic scattering

There are two scattering contributions for the small angle neutron scattering intensity: nuclear scattering, which measures fluctuations in atomic number density, and magnetic scattering, which measures both fluctuations of amplitude and fluctuations of orientation of the local magnetization density [Koh97].

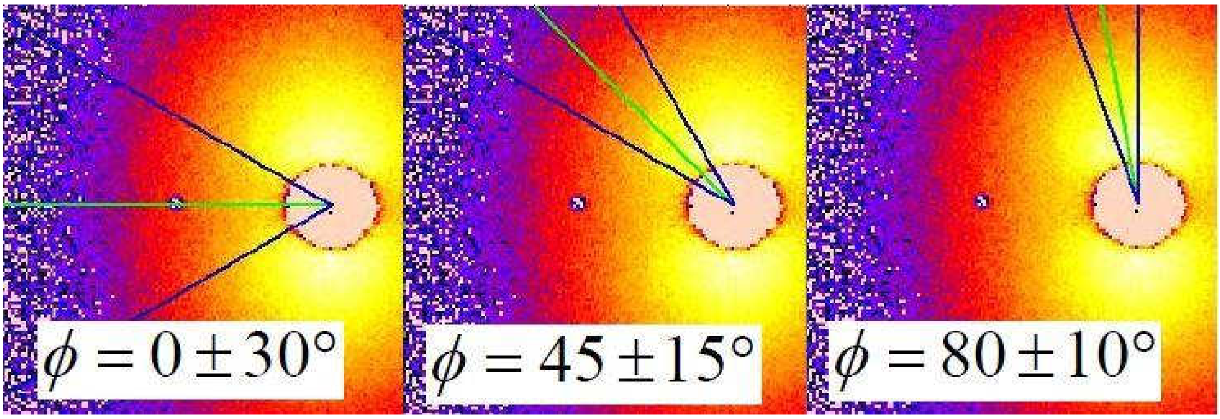

Image 12: Typical 2D SANS pattern with the mask Φ=0±30°, Φ=45±30°, Φ=80±30° [Koh97].

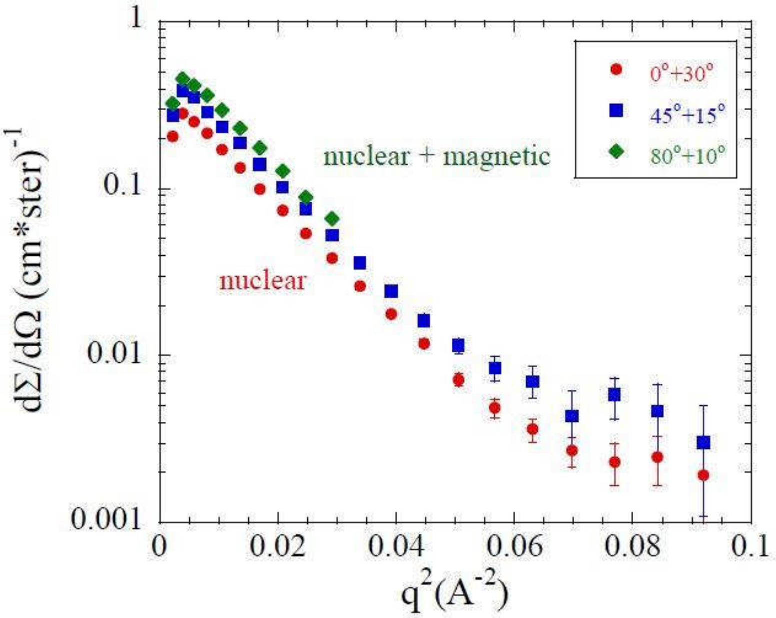

Image 13: The scattering differs from the angle [Koh97].

In this example, the direction of the magnetic field is Φ = 90°. Combining **image 12** with **image 13**, the total scattering cross section can be changed along the angle with outer magnetic field. For Φ = 80±30° angle, the total scattering is displayed the highest cross section compared to other two scatterings with Φ = 0±30° and Φ = 45±30°angle.

The total scattering consists of constant nuclear scattering I_{nur} and magnetic scattering I_{mag}, which can be expressed in a formula:

$$\mathrm{I(Q)} = \mathrm{I}_{nur}(Q) + \overline{sin^2\phi} \cdot \mathrm{I}_{mag}(Q) \tag{3.2.8}$$

where ϕ is the angle between the scattering direction and the magnetization vector, Q is the scattering vector, $\mathrm{I(Q)}$ is the differential scattering cross section (explained later),

From Equation 3.2.8, we can see that the nuclear scattering is the same regardless of the mask position, while the magnetic part changes along with mask angle. Further it can be derived that the intensity stands only for nuclear scattering when with horizontal mask, while the intensity is the sum of the nuclear scattering and magnetic scattering when with vertical mask (seen **image 14**). In this way, the intensity difference between the two masks stands for the magnetic scattering. For the investigation of steels, this is important, in order to separate possible magnetic contributions to the scattering picture.

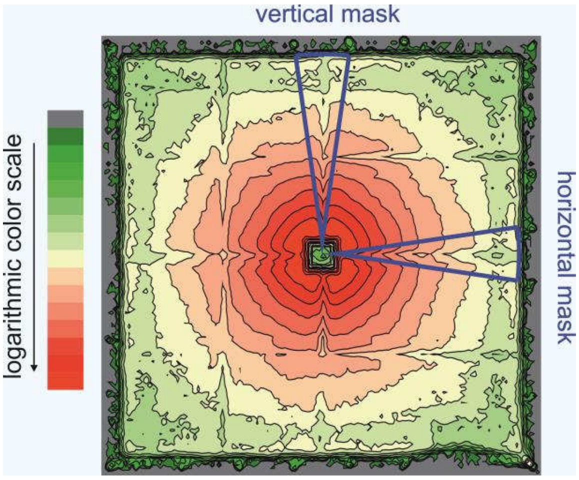

Image 14: 2D SANS image with vertical and horizontal masks

Here in this work for the SANS data reduction, the magnetic scattering differences between “pristine” and “10 to 6”, between “pristine” and “fail” are worked out by using the vertical mask and horizontal mask (see **image 14**) and the derived conclusion on the microstructure transformation between “pristine”, “10 to 6” and “fail” shown in detail in the following experiment section.

3.4.2 Basic principle of SANS measurements

SANS involves scattering of a monochromatic beam of neutrons from the sample and measuring the scattered neutron intensity as a function of the scattering angle. The basic principle of neutron scattering spectrometer is shown below in **image 15**. Incoming neutrons are monochromatized by a mechanical velocity selector. The collimation range of incoming neutrons can be adjusted at three different lengths. A sample chamber is connected to a vacuum system with the detector and collimator tubes.

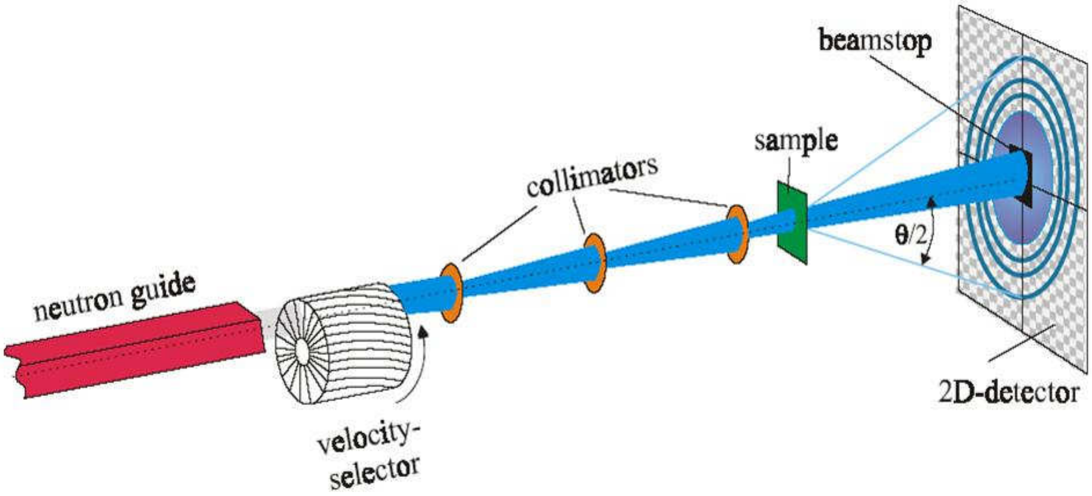

Image 15: Schematic image of the basic components of neutron scattering measure [Wil09]

When the neutron scattering comes into small angle range, the distances from the sample position to the 2D-detector and the lengths of the collimators will be both adjusted in order to attain the very small angle, which is typically 0.5-10 ° from incident beam.

3.4.3 Physical background of SANS

The neutron energy can be derived from the following two basic functions:

$$\lambda = \frac{h}{mv} \tag{3.2.1}$$

where λ is the wavelength of the neutron beams, and h is Plank's constant, m is the mass of neutron, and v is the neutron velocity.

$$E = 81.81\frac{1}{\lambda^2} \tag{3.2.2}$$

The neutron scattering includes mainly five ways as shown in the below **image 16**:

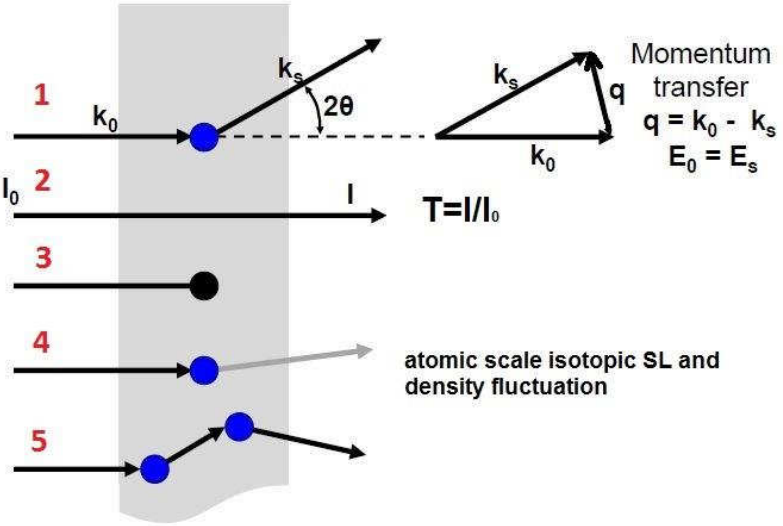

Image 16: Neutron scattering: (1) Coherent elastic scattering; (2) Transmitted beam; (3) Absorption; (4) Incoherent scattering; (5) Multiple scattering [Wil09]

Differential Scattering Cross Section dΣ/dΩ stands for the number of neutrons per second scattered into a small, solid angle dΩ at angle 2θ from incident neutron flux (see **image 17**). The angular SANS dependence is due to interference effects of the scattered neutrons. In principle, SANS and small angle scattering can be understood as the Fourier transform of the nuclear scattering length densities, i.e. of nuclear (or magnetic) correlation in a certain length scale. (In the result dΣ/dΩ is replaced with I considering convenience, q is replaced with Q)

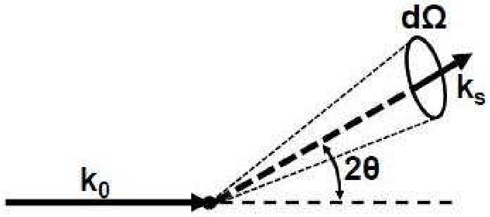

Image 17: Schematic image of solid angle dΩ

Coherent scattering is determined by nuclear properties, which can be related to of the scattering length density [Gui55], scattering length density ρ, which depends on the nuclear density.

$$\rho = \frac{\sum_i^n f_i b_i}{\bar{V}} \tag{3.2.3}$$

Where the nominator of the equation (3.2.3) is the sum of weighted scattering lengths, the denomimator stands for the average atomic volume.

dΣ/dΩ(q) varies with the scattering vector q for a neutron with wavelength λ at scattering at angle 2θ (as shown in **image 17**), the expression is shown in the below:

$$q = \frac{4\pi}{\lambda} \sin \theta \tag{3.2.4}$$

The scattering by spherical particles is expressed by the equation:

$$\frac{\mathrm{d}\Sigma(q)}{\mathrm{d}\Omega} = Nx(\Delta\rho)^2 V^2 F(q) S(q) \tag{3.2.5}$$

where N and V are the number density and volume of the particles, $\Delta\rho$ is the scattering contrast between the particles and the matrix, $F(q)$ is the particle form factor and $S(q)$ is the (interparticle) structure factor [Wil09]. The q dependence of the scattering can arise from $F(q)$, $S(q)$, or both at the same time. When the particles are randomly oriented, peaks in $d\Sigma/d\Omega(q)$ arise from $F(q)$, which, for spherical particles, is given by

$$\mathrm{F(q)} = \left[\frac{3[sin(qR) - qRcos(qR)]}{(qR)^3}\right]^2 \tag{3.2.6}$$

where R is the particle diameter, for further detail see [Wil09].

3.4.4 Data reduction and calibration

To collect a complete set of data for a given sample, it will be necessary to make several complementary measurements. They include the measurements made on the empty sample container or cell, a calibrant or standard sample, the dark count or sample-independent background and a measure of the detector response or efficiency [Adr95].

Scattering intensity is measured and corrected,

$$\mathrm{I}_{cor} = I_{sam} - I_{bgd} - \frac{T_{sam}}{T_{emp}}\left(I_{emp} - I_{bgd}\right) \tag{3.2.7}$$

Where I_{cor} is the corrected intensity, I_{sam} is the measured intensity, I_{bgd} is background, I_{emp} is the empty container intensity, and T_{sam} and T_{emp} are the transmission of sample and empty container [Adr95].

Scattering data from:

- Sample
- Absolute standard – plexiglass
- Empty beam
  - For absolute standard background – empty cell
- Electronic noise background measurement-beam blocked by cadmium or other materials

Transmission data from:

- Sample
- Empty hole –image of the direct beam on the multidetector
- Absolute standard – plxiglass

The SANS data treatment is presented in the flow chart shown in **image 18**.

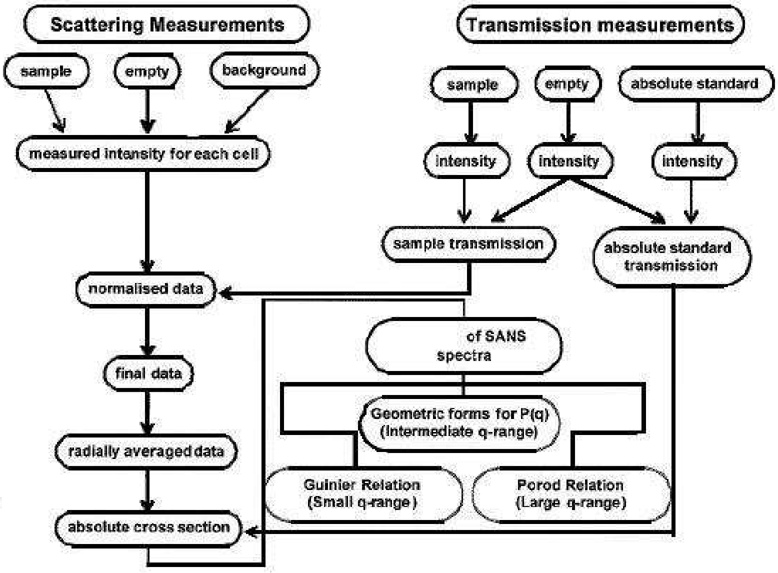

Image 18: Principle of the SANS data treatment [Wil09].

The data treatment begins with determination of detector dead time, the background and the empty cell scattering. Then the intensities for the electronic noise background and sample background can be corrected, and the differential cross section from these corrected intensities can be obtained. Additionally, one usually uses a material, which expects a single scattering intensity to be isotropically distributed in the forward direction, as an absolute standard. In this work, plexiglass has been chosen to calibrate the detector.

3.4.5 Fitting

In this work, there are two fitting models in application: absolute power law (shape-independent) and sphere model (shape-dependent).

An absolute power law analysis is done by linearizing the data at relative high Q by plotting it as $log(I)$ versus $log(Q)$. In this region we can fit the following model:

$$\mathrm{I(q)} = \frac{\mathrm{C}}{Q^m} + background = \frac{2\pi\Delta\rho S_V}{Q^m} + background \tag{3.2.9}$$

C is the scale factor and S_V is the specific surface area of the sample and $\Delta\rho$ is the contrast factor (8×10^{-6} in this SANS measure) and m is the Porod exponent. The background term is added for data analysis.

The returned value is scaled to units of [cm^{-1}] and the parameters of the sphere model are the following **table 4**:

Table 4: The returned values and the parameters of the absolute power law in SANS.

Parameter name	Units	Default value
Scale	None	0.1
m	None	4
background	cm^{-1}	0

The scattering invariant is a model-independent quantity that can be easily calculated from the scattering data. The quantity S_v is the surface area per unit volume of sample (also called the specific surface area) can be determined in cases where the volume fraction is independently known [Gui55]. With this normalization, the scattered intensity does not even need to be in absolute units (ϕ is known the volume fraction).

$$S_V = \frac{\pi\phi(1-\phi)C}{Q} \tag{3.2.10}$$

Sphere model provides the form factor, $P(q)$, for a mono-disperse spherical particle with uniform scattering length density. The form factor (see Section 3.2.2) is normalized by the particle volume as described below. The 1D scattering intensity is calculated in the following way [Gui55]:

$$\mathrm{P(q)} = \frac{\mathrm{scale}}{\mathrm{V}}\left[\frac{3V(\Delta\rho)[\sin(qr)-qr\cos(qr)]}{(qr)^3}\right]^2 + bkg \tag{3.2.11}$$

Where $scale$ is a scale factor volume fraction, V is the volume of the scatter, r is the radius of the sphere, “bkg” is the background level, and ρ is the scattering length density (SLD) of the scatterer or the solvent.

For the polydispersion distribution of Sphere model, the lognormal distribution is chosen to analysis the model’s polydispersion.

$$\mathrm{f(x)} = \frac{1}{\mathrm{Norm}}\frac{1}{xp}exp\left(-\frac{(lnx-\mu)^2}{2p^2}\right) \tag{3.2.12}$$

The $Norm$ is a normalization factor which will be determined during the numerical calculation. The median value is the value given in the size parameter. The PD (polydispersity) is given by sigma, $PD = p$. For the angular distribution: $p = \sigma/x_{med}$. The mean value is given $x_{mean} = exp(mu + p^2/2)$, and the peak value is given by $x_{peak} = exp(mu - p^2)$. This distribution function spreads more and the peak shifts to the left as the p increases.

Apart from the small angle neutron scattering, in this work the Grazing-incidence small angle X-ray scattering was also used to probe the surface of the steel specimen, in order to understand the cracks formation better. Later the working mechanism and its application area will be introduced.

3.5 Grazing-incidence small-angle X-ray scattering (GISAXS)

Grazing-Incidence Small-Angle X-ray Scattering (GISAXS) gives information on nanoscale density correlations and/or the shape of nanoscopic objects at surfaces and interfaces. GISAXS combines features from Small-Angle X-ray Scattering (the length scale, incident beam definition by multiple slits, area detector) and diffuse X-ray Reflectivity (the scattering geometry and sample goniometer). The technique was firstly introduced by Joanna Levine and Jerry Cohen [Lev89], [Lev93], but has become popular in the past decade for the study of nanostructured thin films, coatings and substrates.

3.5.1 GISAXS theory

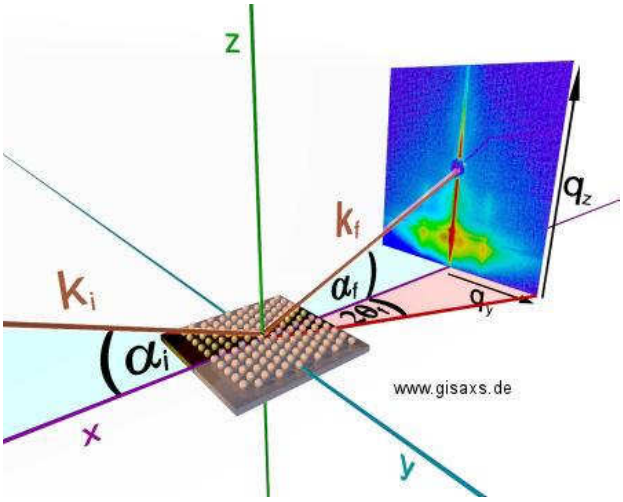

Image 19: GISAXS geometry [Mey12]

The geometry of a GISAXS experiment is illustrated in **image 19**. A monochromatic X-ray beam indicated with the wave vector k_i is directed on a surface, and the incident angle α_i respect to the surface is supposed to be very small. The z-axis shown in the image is the normal to the surface plane, the x-axis is the direction along the surface parallel to the incident beam the y-axis is along the surface and perpendicular to x-axis. The X-rays are scattered along k_f in the direction $(2\theta_f, \alpha_f)$ by any type of electron density characterization of the surface. The appearing scattering wave vector q is expressed with three spatial directions:

$$q_{x,y,z} = \frac{2\pi}{\lambda}\begin{bmatrix} \cos(a_f)\cos(2\theta_f) - \cos(a_i) \\ \cos(a_f)\sin(2\theta_f) \\ \sin(a_f) + \sin(a_i) \end{bmatrix} \tag{3.4.1}$$

In general, a 2-D detector records the scattered intensity at angles of a few degrees for the observation of lateral sizes ranging from a few up to hundreds of nanometers. The sample detector distance is normally in a range of 1 to 4 meters for GISAXS.

The scattering intensity $I(q)$ for a lateral electron density fluctuation on the surface can be described as

$$I(\vec{q}) = \langle |F|^2 \rangle S(q) \tag{3.4.2}$$

where F is the form factor and $S(q)$ is the total interference function. The interference function describes the spatial arrangement of the objects on the surface and thus their lateral correlations. It is the Fourier transform of the island position autocorrelation function. In the simple Born approximation (BA), F is the Fourier transform of the shape function of the objects and is defined as

$$F(\vec{q}) = \int_V \exp(i\vec{q} \cdot \vec{r}) d^3 r \tag{3.4.3}$$

3.5.2 Two extreme cases of GISAXS

If the two interface form lamellae parallel to the substrate, then the signature of parallel lamellae in GISAXS is supposed to present stripes of intensity at regular spacings along the q_z direction (see **image 20**).

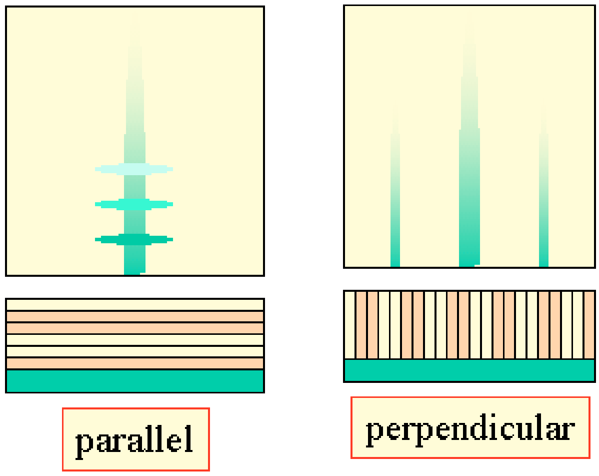

Image 20: Two scattering in the extreme cases [Smi14]

If the two interface form lamellae perpendicular to the substrate, then the signature of parallel lamellae in GISAXS is supposed to present stripes in the q_z direction at regular space.

However, in general the real scattering patterns are more complicated, which can be explained further in the studies of Distorted wave Born approximation (DBWA) theory [Bus06]. Due to the insufficiency of GISAXS measurement statistics in our experiment, it is hard to analyze and come into a conclusion, therefore the DBWA theory won't be discussed here.

In order to build the relationship between load cycle and elastic constant of the specimen, the method of ultrasonic spectroscopy is investigated to attain the specimens' elastic constants.

3.6 Resonant ultrasound spectroscopy (RUS)

Based on the mechanical resonances of small specimens with defined geometries such as cylindrical, rectangular parallelepiped or spherical samples, resonant ultrasound spectroscopy (RUS) is able to extract the elastic modulus tensor [Mig97]. Frazer and LeCraw [Fra64] and Holland [Hol68] were the first to apply the RUS method to materials-science field. The mechanical resonances solves the equations, which depend only on the density, elastic moduli and shape, in a special way [Alb96].

3.6.1 Basic set-up of RUS

Geophysicists Soga and Anderson [Sog76] improved the method of Frazer and LeCraw by developing a two-transducer setup, with the sample in-between transducers, which is still commonly applied today. The geometry of RUS can be seen in **image 21** below.

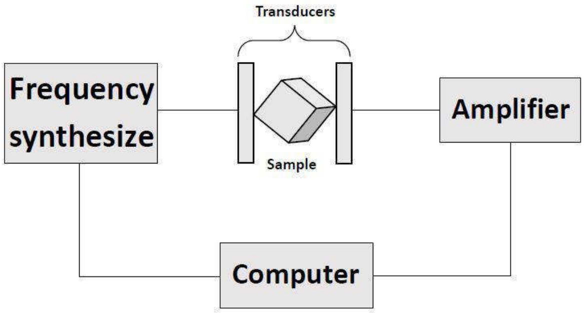

Image 21: The basic model of resonant ultrasound spectroscopy

A frequency synthesize generates a desired range of frequencies to the first piezo-electric transducer, which can transfer an elastic wave with a changing frequency in sample. Meanwhile, ultrasound frequencies resonantly transmitted through the sample and detected by the second transducer will be amplified by a lock-in amplifier, which generates many single resonant peaks in measured spectrum.

3.6.2 Data analysis of RUS

Free vibrations of a rectangular parallelepiped are mainly solved by the minimization method. By combing kinetic energy E_k and potential energy E_p, the Lagrangian L can be expressed as [Mig97]:

$$\mathrm{L} = \int_V \left(E_k - E_p\right) dV \tag{3.3.1}$$

The kinetic energy E_k and potential energy E_p can be further expressed with the volume V of the solid connected with the mass density ρ and the surface S, C_{ijkl} the tensor of elastic constants, w the angular frequency of the system and u_i the displacement along the x_i axis.

$$E_k = \frac{1}{2}\sum_i \rho w^2 {u_i}^2 \tag{3.3.2}$$

$$E_p = \frac{1}{2}\sum_{j,k,l} c_{i,j,k,l} \frac{\partial u_i}{\partial x_j}\frac{\partial u_k}{\partial x_l} \tag{3.3.3}$$

Here u_i stands for the displacement along certain directions denoted with its subscript, i.e. $i = x, y, z$. $dL = 0$ is attained due to the vibrational principle, therefore, the condition can be derived into the expression:

$$\rho w^2 u_i + \sum_{j,k,l} c_{i,j,k,l} \frac{\partial u_k}{\partial x_j}\frac{\partial u_k}{\partial x_k} = 0 \tag{3.3.4}$$

To expand the application area of the equation 3.3.4, here $\vec{a}$ is used to correspond to the displacement vector u_i . two matrices $\boldsymbol{E}$ and $\boldsymbol{\Gamma}$ stand for the two terms in equation 3.3.4. Eventually, the form of equation can be derived into:

$$\mathrm{w}^2 \mathrm{E}\vec{\mathrm{a}} = \Gamma\vec{\mathrm{a}} \tag{3.3.5}$$

The final equation 3.3.5 can be solved with standard numerical technique when given the values of the mass density, the dimensions and start estimated values of elastic constants. The result of this equation shows out the free oscillation frequencies. And then the estimated values of the elastic constants are adjusted to make the calculated frequencies match with the attained resonance frequencies in the experiment. More detail can be found in the literature [Mig97].

4 Experiments

Under the very high cycle fatigue, the fracture behaviors of the high strength partially martensitic steels are studied in this research. Here the structural steel X10CrNiMoV12-2-2, i.e. about 12 wt-% Cr, 2.5 wt-% Ni and 1.75 wt-% Mo, used typically for turbine blade application, is studied during VHCF regime. Further the early stages of nanometer sized fatigue crack formation in VHCF steel are investigated with small angle neutron scattering non-destructive in real specimen. On that, the investigated micro-structure will be further qualified with X-ray small angle scattering and build a relationship with the relevant material properties. Meanwhile the relationship between load cycle and elastic constant of the specimen is investigated with the method of ultrasonic spectroscopy. Additionally, further methods of material characterization, e.g. Mössbauer spectroscopy, will be applied and learned.

1. Analysis and evaluation of small angle neutron scattering

2. Prepare specimen for the grazing-incidence small-angle X-ray scattering and conduct the experiment

3. Process specimen for the resonant ultra-sound spectroscopy and conduct the experiment

4. Correlation micro-structure and elastic constant with the relationship state

5. Overview on chemical components through Mössbauer spectroscopy.

4.1 Material composition and fatigue test

Here the structural steel X10CrNiMoV12-2-2, i.e. about 12 wt-% Cr, 2.5 wt-% Ni and 1.75 wt-% Mo. (referring to Table)

The Steel was hardened by annealing at 1040 °C for 60 min and subsequent compressed air cooling. For stress relief purposes, in this way a relative high martensitic component microstructure is obtained, subsequently this material was tempered at

660 ℃ for 3 h followed by annealing at 640 ℃ for 4 h and ended with very slow furnace cooling [Til13], see in section 3.1.2.

Moreover, the first specimen was not under any fatigue tests, named “pristine”, the second specimen was through the fatigue test with the tensile mean load of R = 0.1, σ_a = 370 Mpa at 10^6 load cycles, is marked with “10 to 6”. The third specimen was through the same test with the same tensile load, i.e. R = 0.1, σ_a = 370 Mpa, but at 2.691×10^6 load cycles, and occurred clearly deformation, which was detected by the tensile test machine. It is labeled with “fail”.

4.2 Mössbauer spectroscopy

A dated, yet comprehensive overview over the applications of Mössbauer spectroscopy can be found in the literature [Phi11]. Mössbauer spectroscopy has already found a wide range of applications in the research concerning the physical metallurgy of steels. An example of such research is an application of his technique in the analysis transformation of retained austenite in low-alloy steel [Skr84]. However, in work [Grg04], using Mössbauer spectroscopy, thermal stability of metastable austenite, present in fast-crystallized tool steel obtained by powder metallurgy method, was described.

This procedure is to analyze and determine different phases and their corresponding content after the heat treatment of structural steel X10CrNiMoV12-2-2, and compare the result to the description in the relevant literature [Til13].

4.2.1 Mössbauer spectroscopy experiment

In this study, ^{57}Fe Mössbauer spectra were obtained on a constant-acceleration spectrometer using a ^{57}Co/Rh source. The velocity calibration was performed with α-Fe at room temperature, referred to section 4.2.3.

For TMS measurements a conventional NaI scintillation detector was used, whereas the so called CEMS-cell was a gas detector constantly floated with a gas mixture of 95% He and 5% CH_4.

4.2.2 Mössbauer spectroscopy specimen preparation

For TMS, a “pristine” steel sample was grinded into powder, which was mixed with BN_2 powder and clamped into a Ti sample holder, see **image 22**. Concerning the reference sample of α-Fe, the specimen preparation is identical. For CEMS, a polished disc was mounted within the detector.

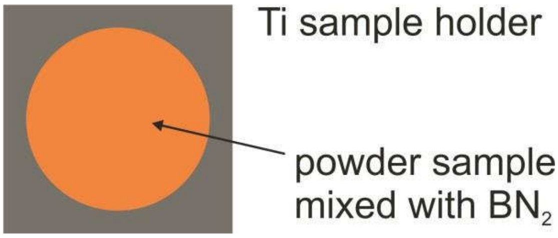

Image 22: The specimen profile of Mössbauer spectroscopy

4.2.3 Mössbauer spectroscopy validation

For the Mössbauer spectroscopy validation, a reference sample of standard α-Fe was used. For analysis of Mössbauer spectra, there are many different fitting algorithms. In general the absorption energy profile $I\ (E)$ is assumed to be a Lorentzian centered at E_0 with line intensity I_0 and full width at half-maximum Γ, see equation 4.2.3. Lorentzian line can give a good a prroximation of line shapes in spectra of parameter materials.

$$L(E, E_0, \Gamma\ ) = \frac{\left(\frac{\Gamma}{2}\right)^2}{(E-E_0)^2+\left(\frac{\Gamma}{2}\right)^2} \qquad (4.2.3)$$

The experimental data is fitted with a sextet function, as the sample is magnetic. This sextet consists of six Lorentzian lines according to following formula:

$$sextet(x, is, qs, hf, g) = 0.25 \times \left(L\left(x, is + \frac{qs}{2} - hf\frac{10.62}{660}, g\right) + L\left(x, is + \frac{qs}{2} + hf\frac{10.62}{660}, g\right)\right) + 0.1667 \times \left(L\left(x, is + \frac{qs}{2} - hf\frac{6.16}{660}, g\right) + L\left(x, is + \frac{qs}{2} + hf\frac{6.16}{660}, g\right)\right) + 0.083 \times \left(L\left(x, is + \frac{qs}{2} - hf\frac{1.68}{660}, g\right) + L\left(x, is + \frac{qs}{2} + hf\frac{1.68}{660}, g\right)\right) \qquad (4.2.3)$$

The total function is $f\ (x) = BG - A \times sextet(x, is, qs, hf, g)$

where is stands for isomer shift , qs is quadrupole splitting, hf is magnetic splitting, BG is background and $A1$ is the relative amount of the phase (here is meaningless, but necessary information in the following measurement)

4.2.4 Measurement of steel X10CrNiMoV12-2-2

Both conventional Transmission Mössbauer spectroscopy (TMS) and Conversion Electron Mössbauer Spectroscopy (CEMS) were applied to the Steel X10CrNiMoV12-2-2 specimen to investigate its phase detail and surface. For TMS, the fitted curve model is $g(x)$ with three sextet formula (see equation 4.2.3) and one doublet formula:

$$doublet(x, isd, qsd, g) = 0.5 \times \left(L\left(x, isd + \frac{qsd}{2}, g\right) + L\left(x, isd - \frac{qsd}{2}, g\right)\right) \qquad (4.2.4)$$

The total fitting function for steel X10CrNiMoV12-2-2 is

$$\begin{aligned} f\,(x) = BG - A1 \times sextet(x, is1, qs1, hf1, g1) - A2 \times sextet(x, is2, qs1, hf2, g2) \\ -A3 \times doublet(x, isd, qsd, g3) \end{aligned} \qquad (4.2.5)$$

where BG is background, and A is relative intensity.

The resulting fitting are shown and analyzed in the result section.

4.3 Small angle scattering (SANS)

4.3.1 SANS specimen

In this work, three specimens with different load cycles were chosen in order to mimic different stages of fatigue. All specimens were prepared in the geometry, see **image** 2. Moreover, the first specimen was not under any fatigue tests, named “pristine”, the second specimen was through the fatigue test with R = 0.1, σ_a = 370 Mpa at 10^6 load cycles, is marked with “10 to 6”. The third specimen was through the same test with R = 0.1, σ_a = 370 Mpa but at 2.691× 10^6 load cycles, and occurred clearly deformation, which was detected by the tensile test machine. It is labeled with “fail” (referred to section 3.1.6).

4.3.2 KWS-1 instrument

In this work, the small angle scattering instrument KWS-1 [Gil06], which is set up and commissioned in the Neutron Guide Hall West at the MLZ, was used (see **image 23**).

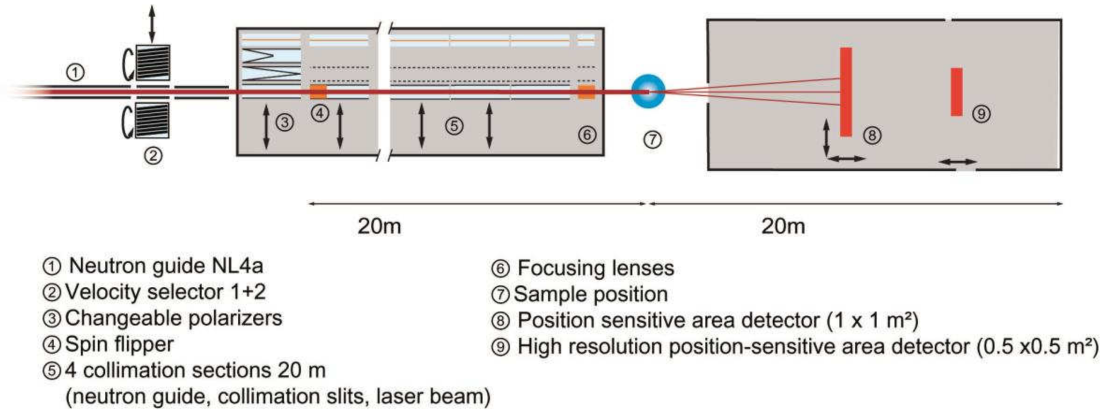

Image 23: KWS-1 scheme referring to Wenzel Schürmann/TUM

And the relevant technical data of KWS-1 refers to the below table (see **table 6**).

Table 5: Technical data of KWS-1 instrument

Primary beam
• neutron flux maximum of the source: 8×10^{14} $ncm^{-2}s^{-1}$ (thermal, undisturbed), especially broad wavelength bandwidth • S-shaped neutron guide (NL 4a), 50 mm x 50 mm cross-section with ^{58}Ni and supermirror (m = 2.0), cut-off at $\lambda c = 3$ Å • mechanical velocity selector with variable speed $\Delta\lambda/\lambda = 10\%$ and a 2nd velocity selector with higher resolution $\Delta\lambda/\lambda = 6\%$, wavelength range 3.5 Å–30 Å
Polarization
• two V-shaped Fe/Si polarisers to cover the main wavelength band from 4–12 Å. A polarization analysis by ^{3}He is under construction.
Source-to-sample distance
• 2 m to 20 m in steps of 2 m via insertion of neutron guide sections • circular pinhole collimation with four tracks in the collimation (neutron

guides, pinhole apertures, laser adjustment and optical components as lenses or elliptical guides are planned)
Sample-to-detector distance
• 1.1 m to 21 m
Sample size
• 0 to 50 mm diameter
Q-range
• $0.0010\ \text{Å}^{-1} < Q < 2\ \text{Å}^{-1}$
Detectors
• first detector with 128 ^{3}He position-sensitive proportional counter with 1000×1020 mm^2 total area and 8 mm resolution and lateral detector movement up to 0.5 m, counting rate over 1 MHz • second detector with 0.5 × 0.5 m^2, 3 mmx3 mm high resolution detector will be installed downstream of the first detector.

The photo of KWS-1 instrument, in particular the sample area, is shown in **image 24**.

Image 24: Sample location in KWS-1 real set-up (photographed by Wenzel Schürmann/TUM)

In our work, in order to facilitate a distinction between nuclear and magnetic contribution of small angle scattering, a hysteresis loop of “pristine” steel was investigated to determine the outer magnetic field when magnetic saturation is reached. In this case, masks as described in section 3.4.1 can be used to distinguish nuclear from magnetic scattering,

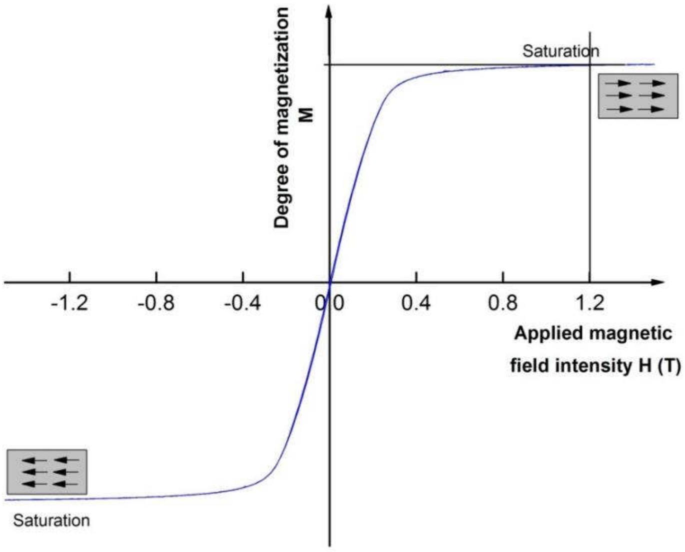

Image 25: Hysteresis loop of "pristine" steel

In **image 25**, the hysteresis loop of steel “pristine” is displayed with saturation at applied magnetic field of 1.2 T. Therefore, the SANS measurement was performed in applied vertical field of 1.2 T in order to saturate the magnetization by aligning all domains (see **image 26**). In this way, the nuclear scattering and magnetic scattering can be clearly separated to analyze, otherwise the mixture of these two scatterings will increase the difficulties to understand the results. Furthermore, in this experiment distances between sample and detector respectively of 2, 8, 20 meters were set in order to get different Q range.

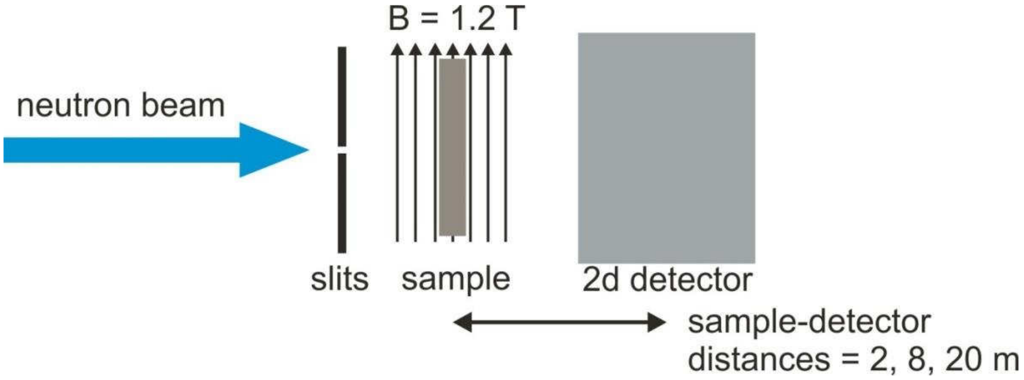

Image 26: Brief geometry of SANS procedure with certain sample-detector distances

4.3.3 SANS complementary measurements and sample measurements

To collect a complete set of data for a given sample, it will be necessary to make several complementary measurements. Generally, they include the measurements made on the empty sample container or cell, a calibrant or standard sample, the dark count or sample-independent background, a measure of the detector response or efficiency as well as one or more background samples such as pure solvent or matrix material [Adr95].

In this work, the measurements consist of those on the empty beam (EB), those on the electronic noise background measurement (B_4C) and those on absolute standard with Plexi glass material (Plexi). (See **image 27**)

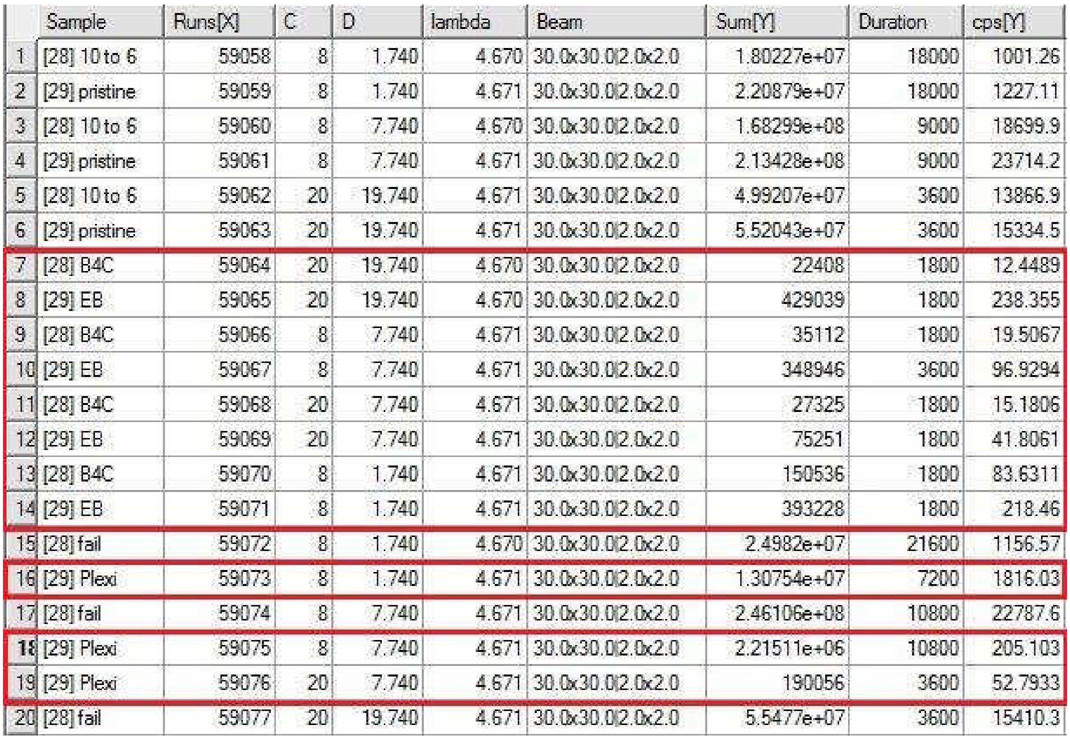

	Sample	Runs[X]	C	D	lambda	Beam	Sum[Y]	Duration	cps[Y]
1	[28] 10 to 6	59058	8	1.740	4.670	30.0x30.0|2.0x2.0	1.80227e+07	18000	1001.26
2	[29] pristine	59059	8	1.740	4.671	30.0x30.0|2.0x2.0	2.20879e+07	18000	1227.11
3	[28] 10 to 6	59060	8	7.740	4.670	30.0x30.0|2.0x2.0	1.68299e+08	9000	18699.9
4	[29] pristine	59061	8	7.740	4.671	30.0x30.0|2.0x2.0	2.13428e+08	9000	23714.2
5	[28] 10 to 6	59062	20	19.740	4.671	30.0x30.0|2.0x2.0	4.99207e+07	3600	13866.9
6	[29] pristine	59063	20	19.740	4.671	30.0x30.0|2.0x2.0	5.52043e+07	3600	15334.5
7	[28] B4C	59064	20	19.740	4.670	30.0x30.0|2.0x2.0	22408	1800	12.4489
8	[29] EB	59065	20	19.740	4.670	30.0x30.0|2.0x2.0	429039	1800	238.355
9	[28] B4C	59066	8	7.740	4.671	30.0x30.0|2.0x2.0	35112	1800	19.5067
10	[29] EB	59067	8	7.740	4.671	30.0x30.0|2.0x2.0	348946	3600	96.9294
11	[28] B4C	59068	20	7.740	4.671	30.0x30.0|2.0x2.0	27325	1800	15.1806
12	[29] EB	59069	20	7.740	4.671	30.0x30.0|2.0x2.0	75251	1800	41.8061
13	[28] B4C	59070	8	1.740	4.671	30.0x30.0|2.0x2.0	150536	1800	83.6311
14	[29] EB	59071	8	1.740	4.671	30.0x30.0|2.0x2.0	393228	1800	218.46
15	[28] fail	59072	8	1.740	4.670	30.0x30.0|2.0x2.0	2.4982e+07	21600	1156.57
16	[29] Plexi	59073	8	1.740	4.671	30.0x30.0|2.0x2.0	1.30754e+07	7200	1816.03
17	[28] fail	59074	8	7.740	4.671	30.0x30.0|2.0x2.0	2.46106e+08	10800	22787.6
18	[29] Plexi	59075	8	7.740	4.671	30.0x30.0|2.0x2.0	2.21511e+06	10800	205.103
19	[29] Plexi	59076	20	7.740	4.671	30.0x30.0|2.0x2.0	190056	3600	52.7933
20	[28] fail	59077	20	19.740	4.671	30.0x30.0|2.0x2.0	5.5477e+07	3600	15410.3

Image 27: Shortcut of the SANS measurements' information: sample measurements and complementary measurements (marked in red).

Subsequently, the "pristine", "10 to 6" and "fail" specimens went through the same measurements.

4.3.4 SANS data reduction and fitting

Through the SANS data reduction and absolute calibration, the absolute intensity is obtained to allow one to be fitted and calculated. Here we choose the masks with 5 and 7degrees angle (horizontal and vertical) to study the magnetic scattering produced by the specimens. In **image 28**, brief profiles of 7-degree horizontal and vertical masks are shown. The red areas stand for the areas where the data was accepted, while the other areas, which are represented as blue, were neglected.

Under these special masks, volume fraction and specific area of scattering element are attained to study the microstructure transformation in specimens. The relevant detail physical background is described in section 3.2.3.

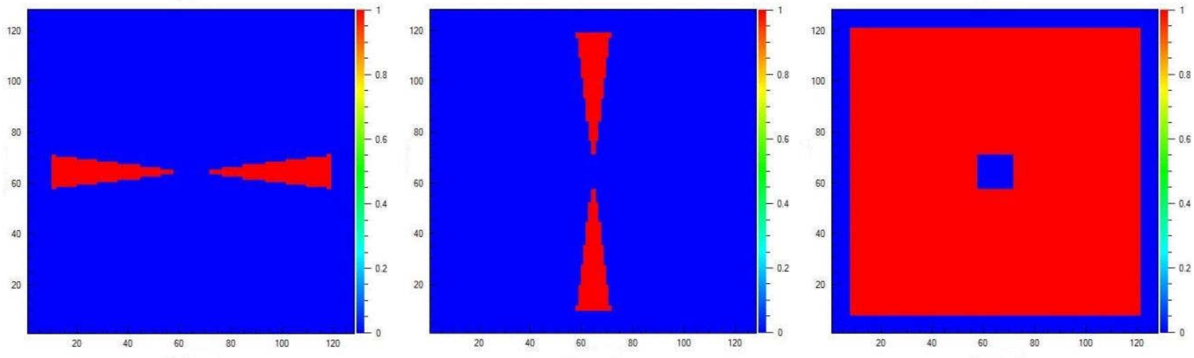

Image 28: The $\mathbf{\Phi} = \mathbf{0} \pm \mathbf{7}°$, $\mathbf{\Phi} = \mathbf{90} \pm \mathbf{7}°$ masks of and normal mask shown in QiKWS software

4.4 Grazing-incidence small-angle X-ray scattering (GISAXS)

Through the GISAX, we can get information specific to surface of specimens. Here the steel specimens are measured in the instrument described in the following part.

4.4.1 GISAXS instrument

The GISAXS instrument applied in this measurement is installed in Juelich Forschungszentrum. The relevant pictures and technical data are shown below in **image 29**, which provided by [Rüc14].

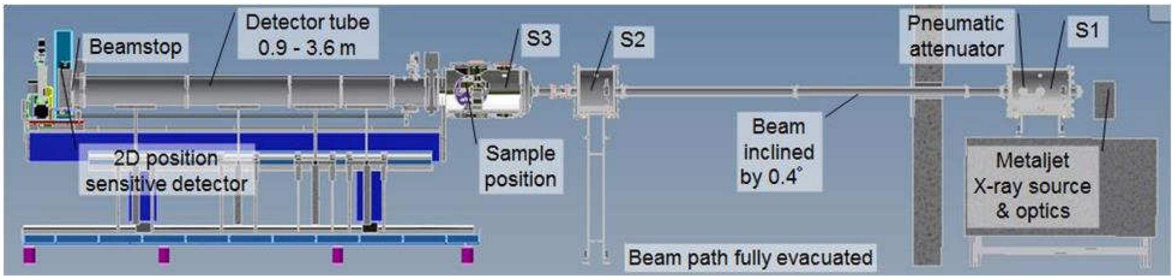

Image 29: Schematic image of X-ray diffractometer for GISAXS [Rüc14]

The detail description is listed in the bellowing **table 7**.

Table 6: Technical data of the MetalJet, Optics and X-ray beam.

MetalJet	• 400 µm thick liquid metal jet (GaInSn alloy) anode • 20 x 80 μm^2 electron beam • 20 µm ø X-ray focus • 70 kV, 200 W, Ga Kα 9240 eV, λ = 1.34 Å • Power density 10 * higher than Cu anode
Optics	• parabolic Montel mirrors, synchrotron grade quality • double reflection
X-ray beam	• 2.4 x 2.4 mm^2, divergence < 0.3 mrad • Intensity > 4×10^9 photons /s

See in **image 30**, the geometries of 2D detector used in this experiment are shown. And the details of silicon-sensor and readout-chip are amplified. And the relevant technical data are listed below.

<u>2D detector: Pilatus 1M</u>

- Detector area 169 x 179 mm^2
- Background < cosmic radiation background
- Crosstalk between pixels < 10^{-6} / 1 mm distance

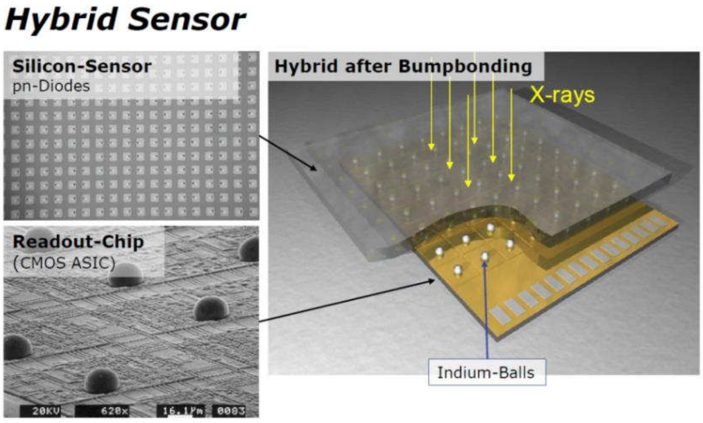

Image 30: 1 Mio Si single detectors 172×172 µm^2 pixel size up to 10^6 cps in every pixel

In **image 31**, the working theory is described and the brief electric circle is shown. Using this construction, the high sensitivity up to 94% discriminator in every pixel can be reached.

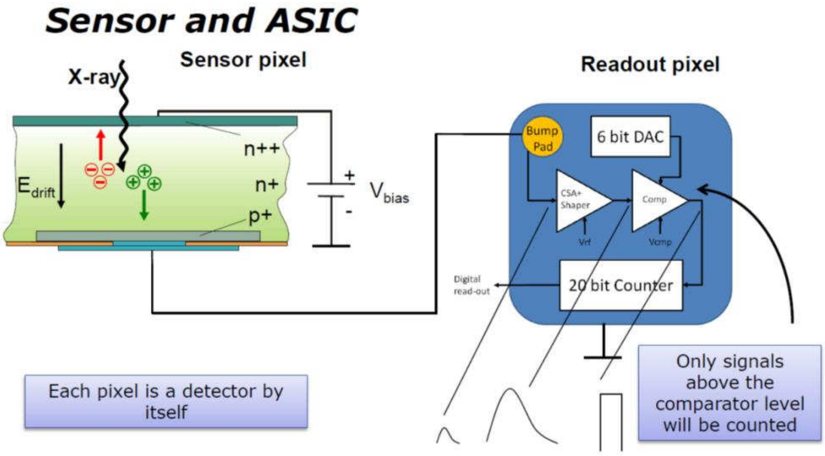

Image 31: Sensitivity 94% discriminator in every pixel

<u>Together: GALAXI</u>

- Flux at sample position > 109 photons / s (100 * higher than at DORIS III)
- Incident beam inclined by 0.4°→ GISAXS from liquid surface possible
- Collimation 0.05 mrad – 1 mrad
- Q range: 3×10^{-3} Å^{-1} – 0.8 Å-1 (in future: 1.5 Å^{-1})

- Beampath fully evacuated
- Signal / noise ratio > 10^6
- Beamline fully computer controlled

4.4.2 Measurement calibration

Thanks to the fact, that the $AgC_{22}H_{43}O_2$ can show several specific rings in the recorded GISAXS 2D pattern, the Ag compound measurement was carried out in order to calibrate the sample detector distance and the accessible Q-range accordingly.

4.5 Resonant ultrasound spectroscopy (RUS)

Migliori introduced the item “Resonant ultrasound spectroscopy” to emcompass all techniques in which ultrasonic resonance frequencies are used to determine elastic moduli.

In this work, specimens in a rectangular parallelepiped form were investigated by using RUS and fitted to obtain their elastic moduli.

4.5.1 RUS specimen preparation

Here, the specimens, which have previously been loaded in the fatigue test, were cut, into the rectangular parallelepiped form. (See **image 32**) Finally, the samples were ground with SiC abrasive paper.

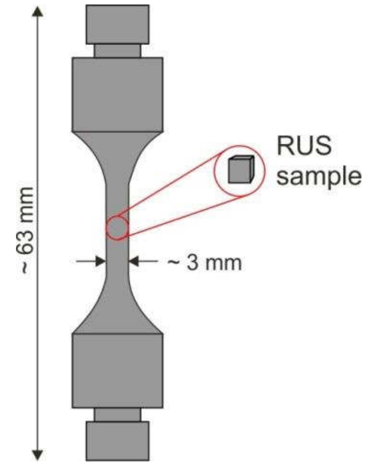

Image 32: Schematic profile of RUS specimen

4.5.2 RUS experiment

As described in section 3.6.1, the basic setup consists of two oppositely mounted PZT piezoelements (see **image 33**). Moreover, a function synthesizer and a lock-in amplifier are used. The function synthesizer generates the desired frequencies, whereas the lock-in amplifier is used to amplify and detect the transmitted signal, which is almost at noise level. A software, which is based on the algorithm developed by Migliori et al [Mig97], is used to analyze the sample spectrum. We have modified the transducer stage to reduce and to control the sample load. The lower transducer is fixed on the set-up, while the upper transducer can be moved vertically to adjust the position to the sample size (see **image 33**).

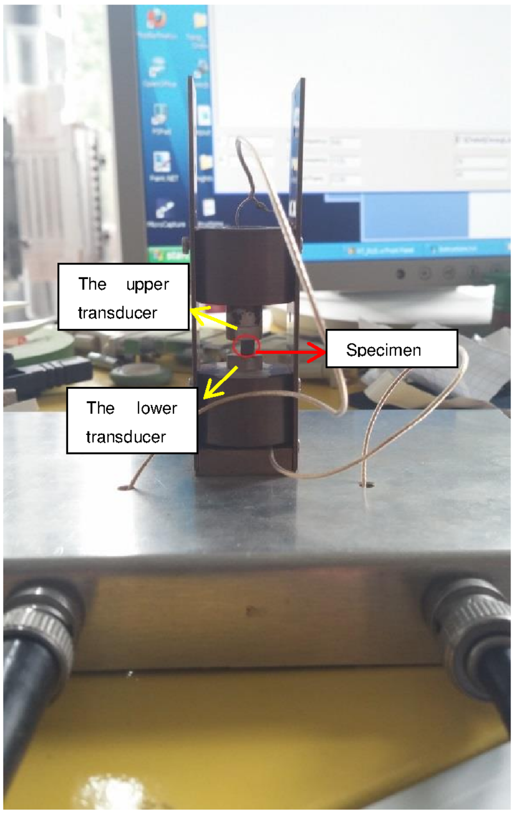

Image 33: Room temperature RUS measurement system

Ina recorded RUS spectrum, resonance frequencies can be clearly seen as peaks (see **image 34**). Then with the samples geometry and density and the estimated start values of elastic modulus and shear modulus, the elastic moduli can be fitted.

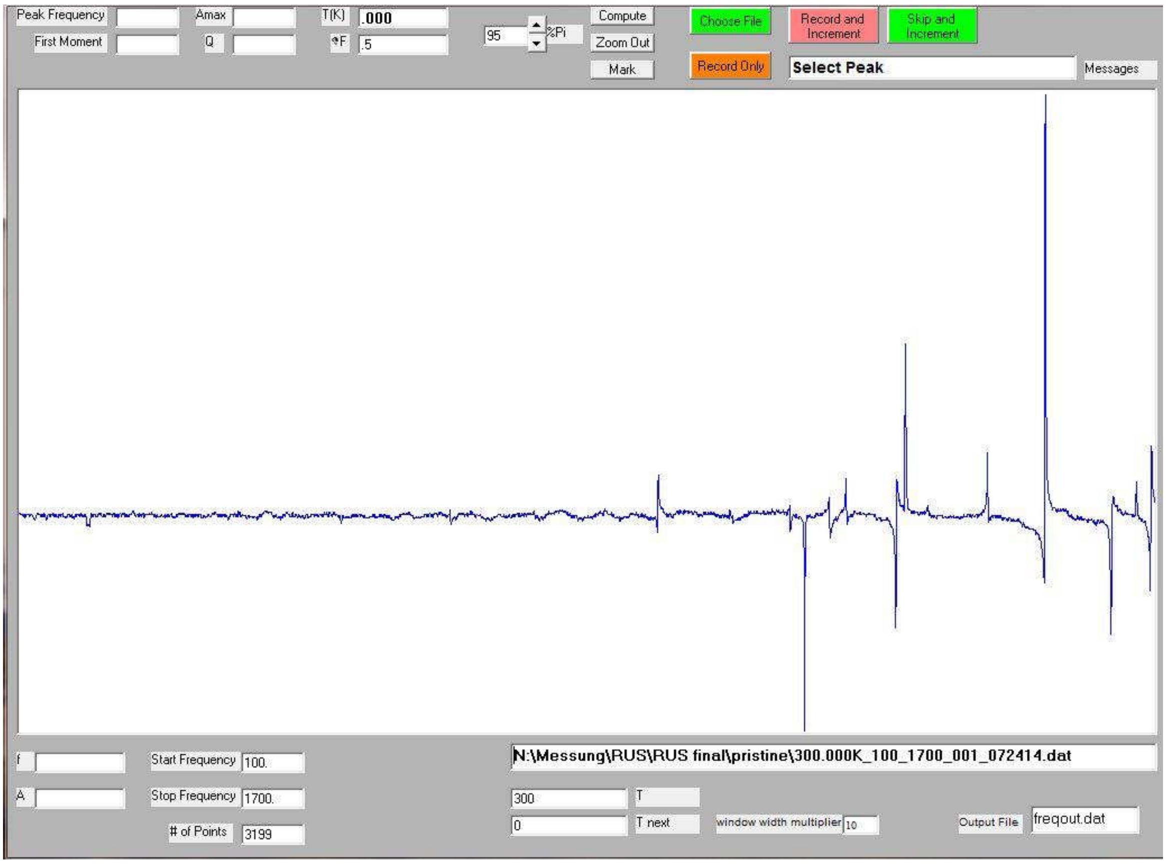

T(K) .000

δF .5

95 %Pi

Select Peak

Start Frequency 100.

Stop Frequency 1700.

# of Points 3199

N:\Messung\RUS\RUS final\pristine\300.000K_100_1700_001_072414.dat

300 T

0 T next

window width multiplier 10

Output File freqout.dat

Image 34: RUS spectrum of $MnSi_{1.85}$ shown in RUS reduction program

4.5.3 RUS validation

For the RUS validation, a reference rectangular parallelepiped sample of manganese silicide $MnSi_{1.85}$ was used. Then, measurements were performed on VHCF steel samples of different fatigue cycles to study the microstructure effect caused by the fatigue test on the elastic modulus.

The manganese silicide $MnSi_{1.85}$ was dimensions of $2.978 \times 3.101 \times 3.047$ mm^3 and a mass of 138 mg. The measurements were repeated 3 times with reattachment of the specimen after each measurement to check the reproducibility and determine the data with the smallest error. In **image 35**, the resonances are shown and in **table 13**, the ten smallest fitted resonance frequencies are listed with their corresponding error.

4.5.4 Measurement of the VHCF steels

Specimen “pristine”, “10 to 6” and “fail” were measured three times respectively. From the spectrum the resonant frequencies are computed and recorded, see **image 35**-**37**.

T(K) .000
F .5
95 %Pi
Select Peak

Image 35: RUS spectrum of "pristine" steel shown in RUS reduction program

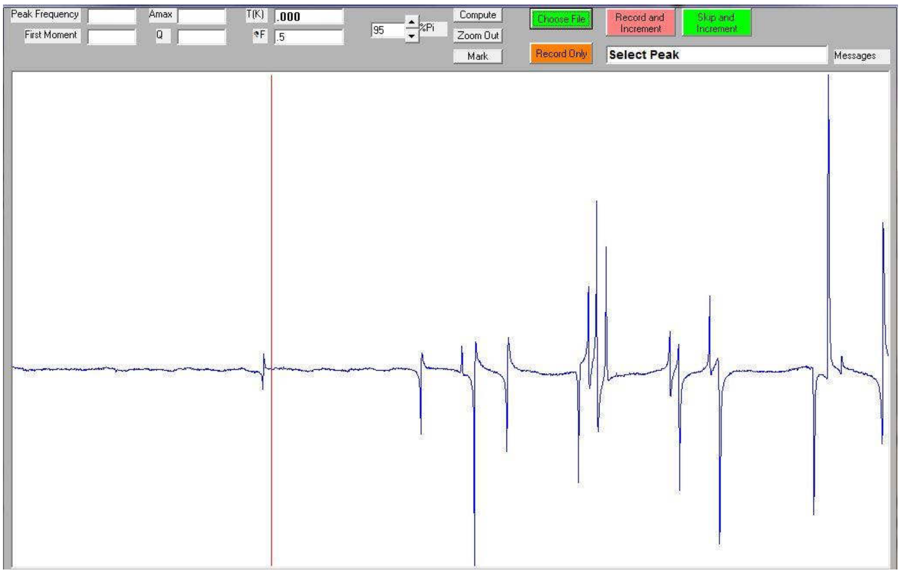

T(K) .000
F .5
95 %Pi
Select Peak

Image 36: RUS spectrum of "10 to 6" steel shown in RUS reduction program

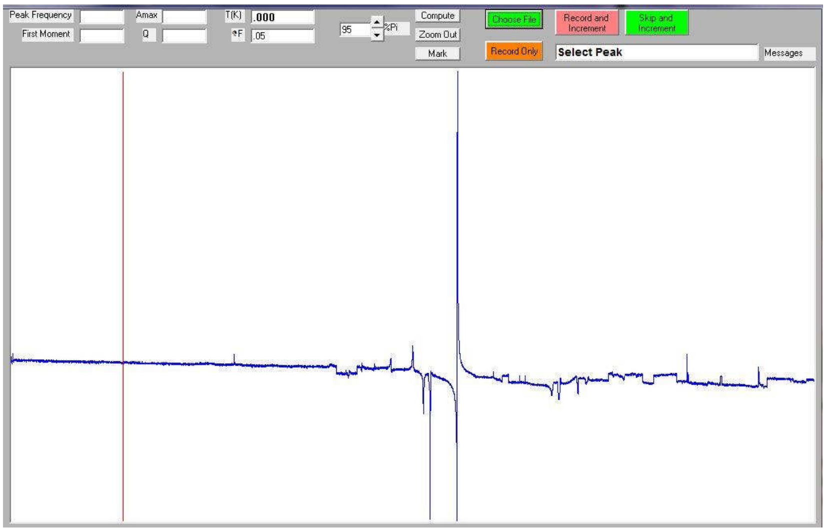

T(K) .000
°F .05
95 %Pi
Messages: Select Peak

Image 37: RUS spectrum of "fail" steel shown in RUS reduction program

In the following results, the data with the smallest error are chosen to be analyzed and fitted. The results are in the following section.

These three specimens were measured in different sizes given in **table 8**:

Table 7: Specimens of steel VHCF with their dimensions ($\boldsymbol{L} \times \boldsymbol{W} \times \boldsymbol{H}$) and densities ($\boldsymbol{\rho}$).

Specimen	**“pristine”**	**“10 to 6”**	**“fail”**
L(mm)	2.049	1.922	2.392
W(mm)	1.770	1.769	2.242
H(mm)	1.430	1.462	1.745
ρ(g/cm^3)	7.30	7.36	7.20

5 Results

5.1 Mössbauer spectroscopy

5.1.1 Mössbauer spectroscopy validation

For the Mössbauer spectroscopy validation, a reference sample of standard α-Fe was used. In **image 38**, the absorption attained from the experiment and its corresponding fitting curves are shown.

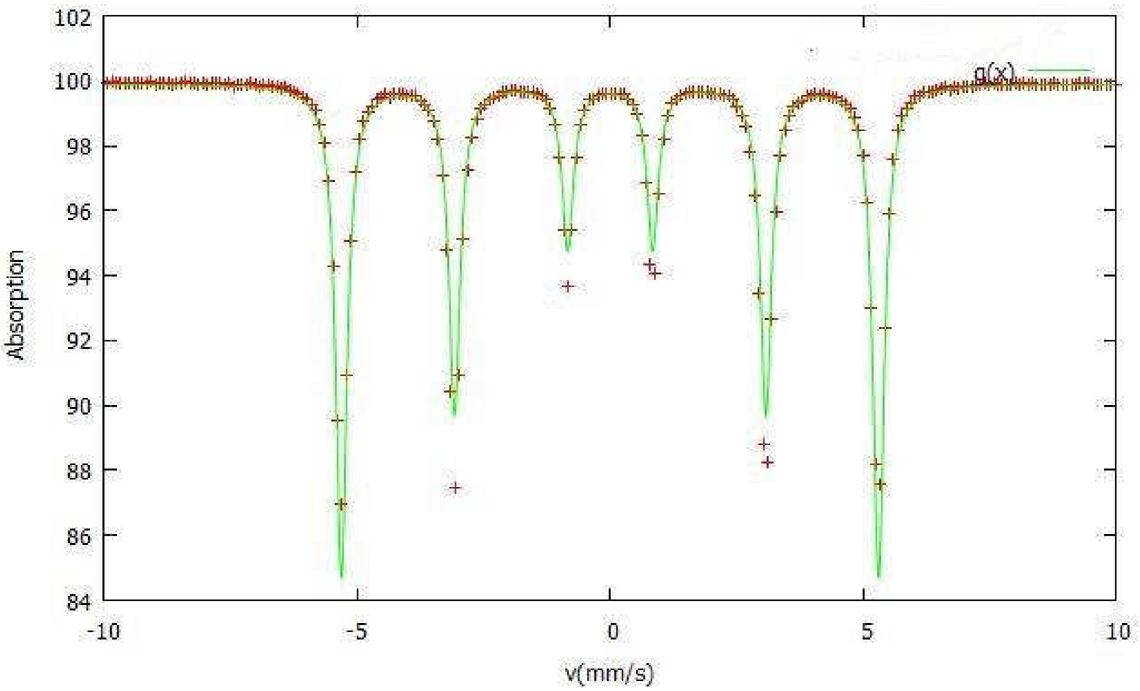

Image 38: Fitted Mössbauer spectrum for standard $\boldsymbol{\alpha}$-Fe

For standard α-Fe, the spectrum is fitted with a sextet and is, at the same time, used to calibrate the velocity scale of the measurement system. By definition, the center, i.e. the isomer shift, is then at 0 mm/s and the center lines are at ±5.312 mm/s.

The difference between the subsequently again fitted spectrum and references are very small (see **table 9**). The Mössbauer spectroscopy instrument thus works satisfactorily considering the correct hyperfine field and the small line width.

Table 8: The fitted is, qs, hf, g of sextet curve model for standard a-Fe

Symbol	meaning	Fitted value	Value in Literature[Mor68]
`is`	Isomer shift (mm/s)	0.0 (1)	0
`qs`	Quadrupol Splitting	0.0 (1)	0
`hf`	Magnetic field (T)	330 (1)	330
`g`	Line width (mm/s)	0.27 (2)	------

5.1.2 Mössbauer spectroscopy measurement of steel X10CrNiMoV12-2-2

The steel X10CrNiMoV12-2-2 specimen was measured. A comparison between the transmission and conversion electron Mössbauer spectroscopy measurements of “pristine” steel is shown in **image 39**.

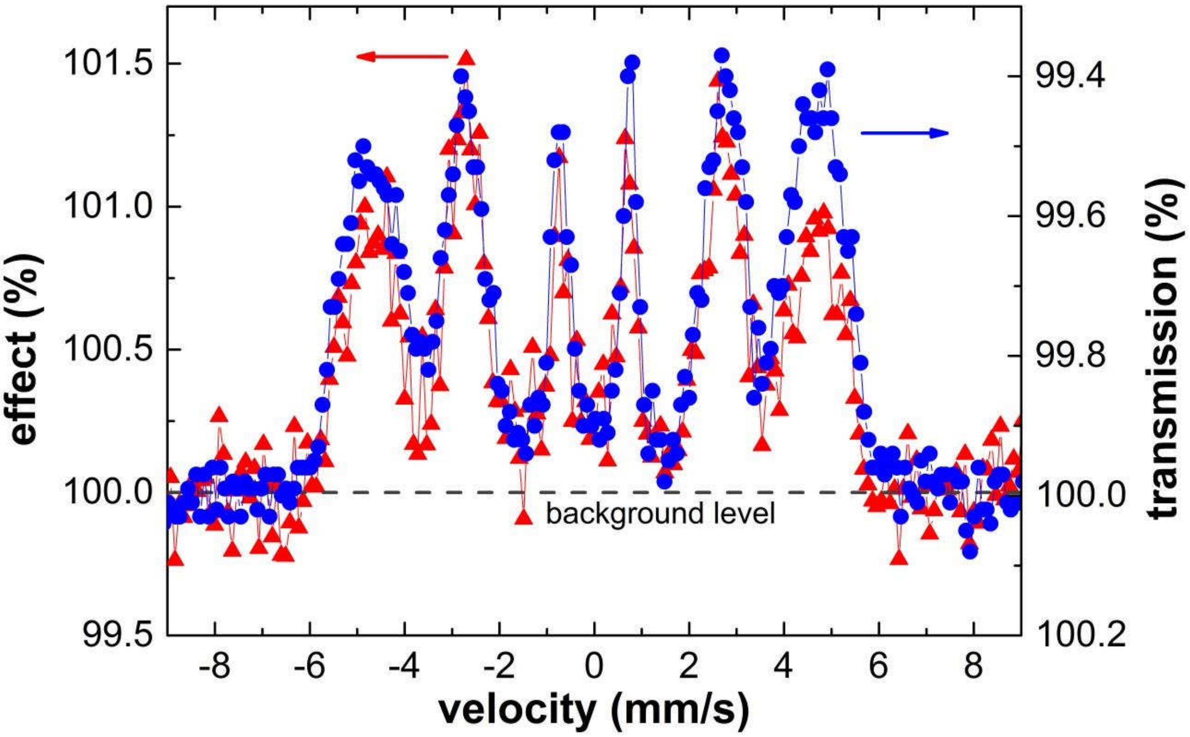

Image 39: Comparison between TEM and CEMS of "pristine" steel

Furthermore, the absorption attained from the experiment and its corresponding fitting curves from CEMS and TMS measurements are shown in **image 40**. In both fitting, two sextet formula and one doublet formula are included.

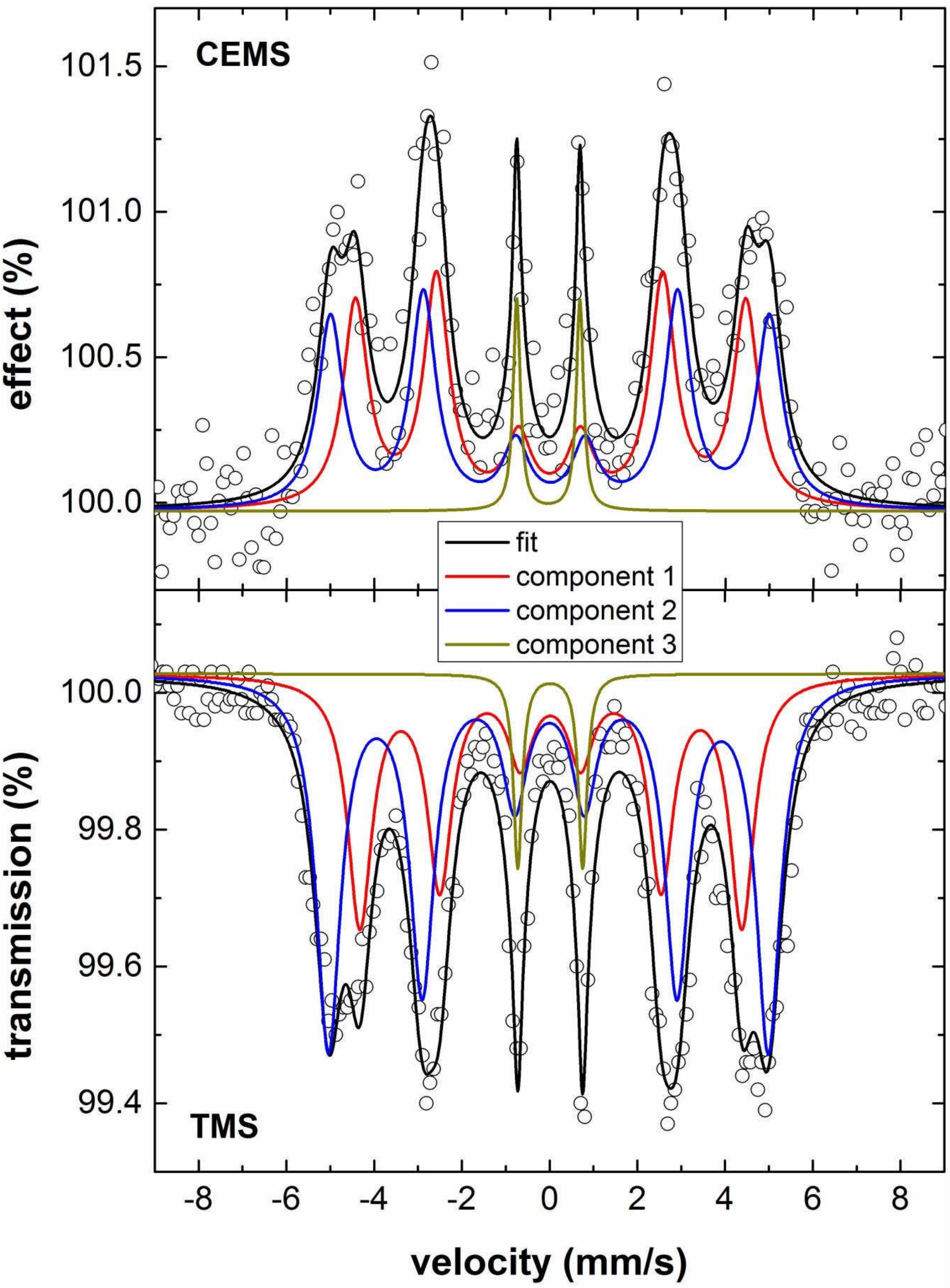

Image 40: Fitted TMS and CEMS Mössbauer spectrum for steel X10CrNiMoV12-2-2

Both the transmission Mössbauer spectroscopy and the conversion electron Mössbauer spectroscopy spectrum can be fitted with a model consisting of two sextets and one doublet (see **image 40**, components 1, 2, and 3, respectively). The fitting parameters, which are summarized in **table 10** and **table 11**, reasonably agree though there are small discrepancies due to the one differing peak. Determination of the components and their amount will be discussed in detail later in section 6.1.

Table 9: The relative fitted parameters “IS”, “QS”, “HF”, “G” and relative intensity of component 1, 2 and 3 for steel X10CrNiMoV12-2-2 sample in TMS

Component	**IS**	**QS**	**HF**	**G**	**Relative intensity(%)**
1	0.02 (1)	0.01 (2)	270 (1)	0.67 (5)	38 (4)
2	-0.01 (1)	-0.03 (2)	312 (1)	0.78 (4)	57 (2)
3	0.02 (1)	1.48 (2)	-------	0.23 (2)	5 (2)

Table 10: The relative fitted parameters “IS”, “QS”, “HF”, “G” and relative intensity of component 1, 2 and 3 for steel X10CrNiMoV12-2-2 sample in CEMS

Component	**IS**	**QS**	**HF**	**G**	**Relative intensity(%)**
1	0.005 (1)	0.03 (2)	276 (1)	0.70 (5)	49 (4)
2	0.008 (1)	-0.013 (2)	310 (1)	0.70(5)	46 (2)
3	-0.0361 (1)	1.4368 (2)	-------	0.23 (5)	5 (2)

5.2 Metallography (Optical Microscopy)

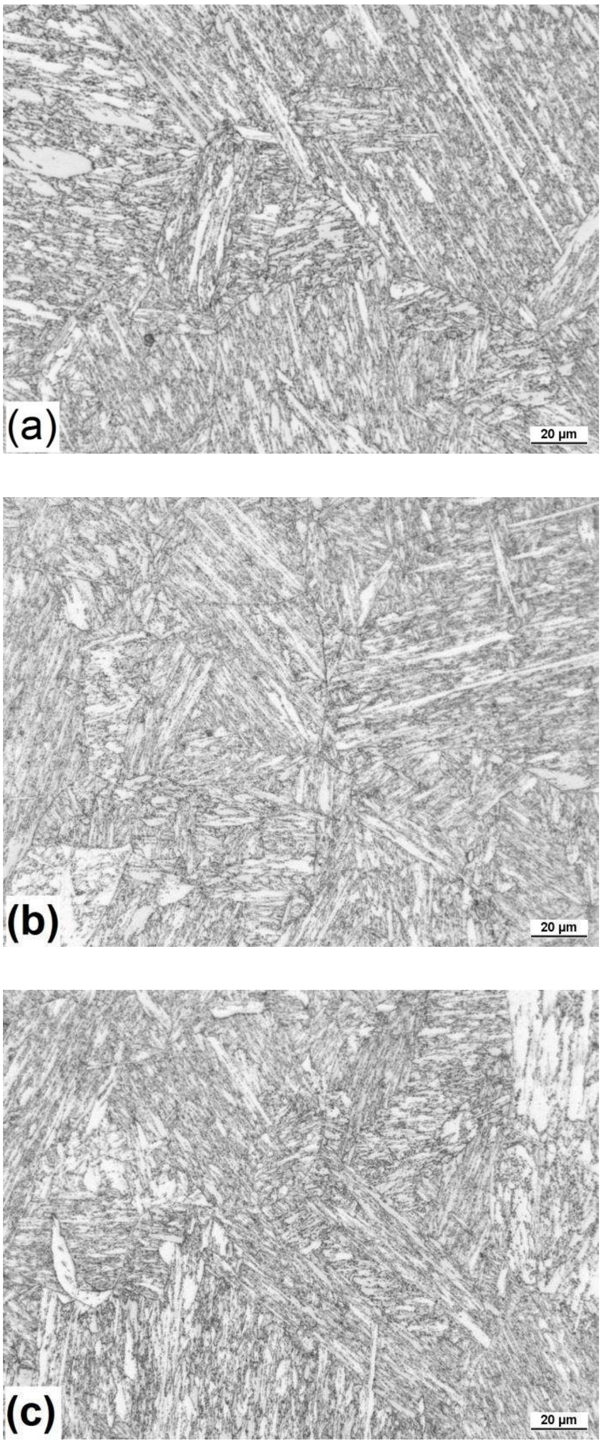

Image 41: Microstructures of: (a) "pristine"; (b) "10 to 6"; (c) "fail" specimens

By observing the microscopic structures of "pristine"; "10 to 6"; "fail" specimens, some of features are supposed to complement and explain the results of SANS measurement. In **image 41**, we can clearly see that, the lath marteinsite phase is the matrix with about more than 90% percentage content, which agrees with the analysis of Mössbauer spectroscopy (referred to section 6.1). However, due to insufficient magnification it is difficult to find out the clear microstructural differences between these specimens. Therefore, the crack formation can be analyzed only by using SANS measurement.

5.3 Small angle neutron scattering (SANS)

5.3.1 SANS cross section as a function of scattering wave vector

At first, the measured average abolute SANS cross section, I obtained using the normal mask (see **image 27**) is displayed in **image 42** as a function of scattering wave vector, Q, representative of the various important regimes, in double-logarithmic plots.

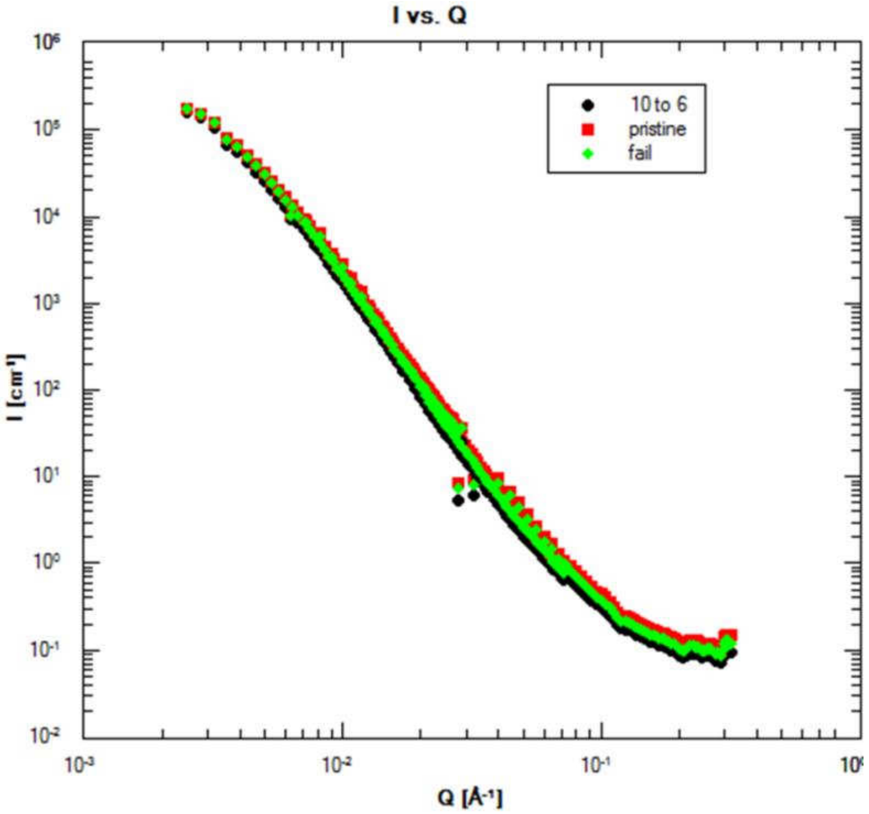

Image 42: SANS profiles of “pristine”, “10 to 6” and “fail” specimens with normal mask

Although three scattering cross sections of “pristine”, “10 to 6” and “fail” steel are clearly identfied with each other in **image 42**, the scattering cross section differences between them at normal mask are small. Moreover, nuclear and magnetic contributions to the scattering are mixed using this kind of mask. As a result, the SANS profile normal mask cannot be accurately analyzed to investigate presumably small changes of the microstructures between these specimen.

5.3.2 Nuclear scattering profiles

The nuclear scattering profiles were in this work also investigated, in order to obtain a relatively bigger scattering cross section difference between these three specimens and in order to separate nuclear and magnetic scattering contibutions.

Here masks from 5-degree to 20-degree are applied to probe the relationship between the angle Φ (refered to equation 3.2.8) and the nuclear scattering. Based on equation 3.2.8, the scattering parallel to the applied field is only of nuclear scattering. Combining with the vertical upwards applied magnetic field in the brief geometry of SANS measurement (see **image 26**), the mask, with which only the nuclear scattering can be displayed, is supposed to vertical mask with certain angle Φ . **image 43** and **image 44** show the nuclear scattering of specimens with 5-degree and 7-degree masks.

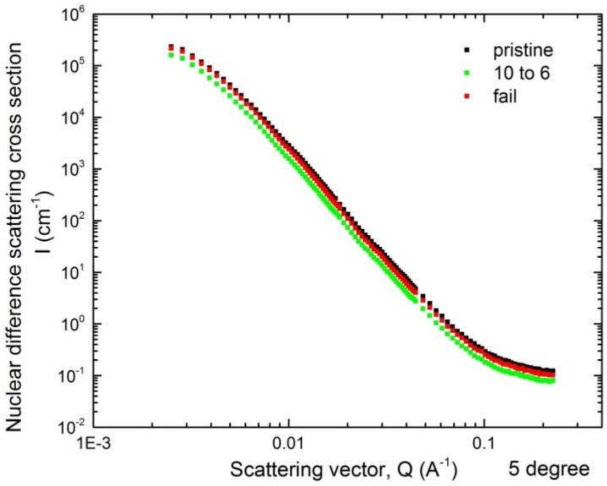

Image 43: Nuclear components of SANS profiles obtained from "pristine", "10 to 6" and "fail" steel with $\boldsymbol{\Phi = 90 \pm 5}$° angle mask

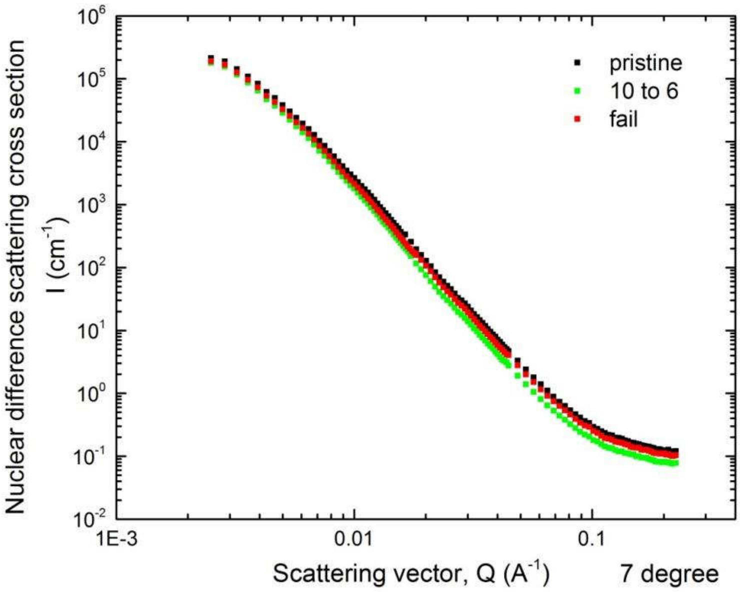

Image 44: Nuclear components of SANS profiles obtained from "pristine", "10 to 6" and "fail" steel with $\mathbf{\Phi = 90 \pm 7°}$ angle mask

However, as shown in **image 43** and **image 44**, the nuclear scattering difference between these three specimens turns out not much biger as expected. Furthermore, the magnetic scattering difference is further investigated. Through studying the magnetic scattering difference, the information on microstructural factors on magnetic scattering can be investigated. Moreover, it is difficult to rely on the absolute scaling in particular with repeat to the background, which can vary slightly from sample to sample. As the evaluation of the magnetic scattering contribution involves substraction of the background within one frame, this is investigated further.

5.3.3 Magnetic scattering profiles

Based on equation 3.2.8, prependicular to the applied field the scattering is the sum of the nuclear scattering and magnetic scattering. By substracting the nuclear scattering profile from the nuclear plus magnetic scattering profile, the magnetic scattering was obtained. Therefore, to the identical degree masks, the magnetic scattering curves of three specimens using the 5-degree and 7-degree masks are displayed in **image 45** and **image 46**.

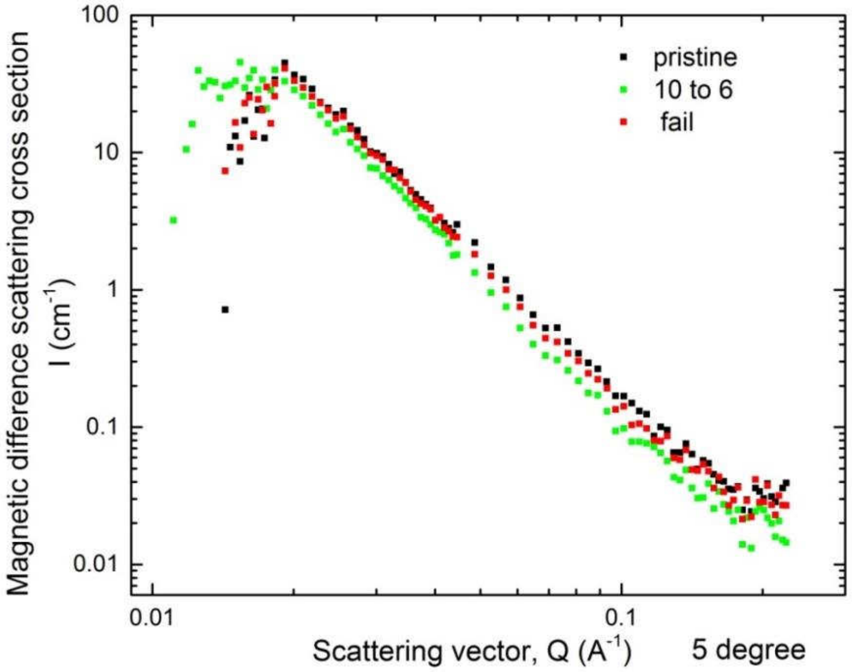

Image 45: Magnetic components of SANS profiles attained from “pristine”, “10 to 6” and “fail” specimens with 5 degree angle mask

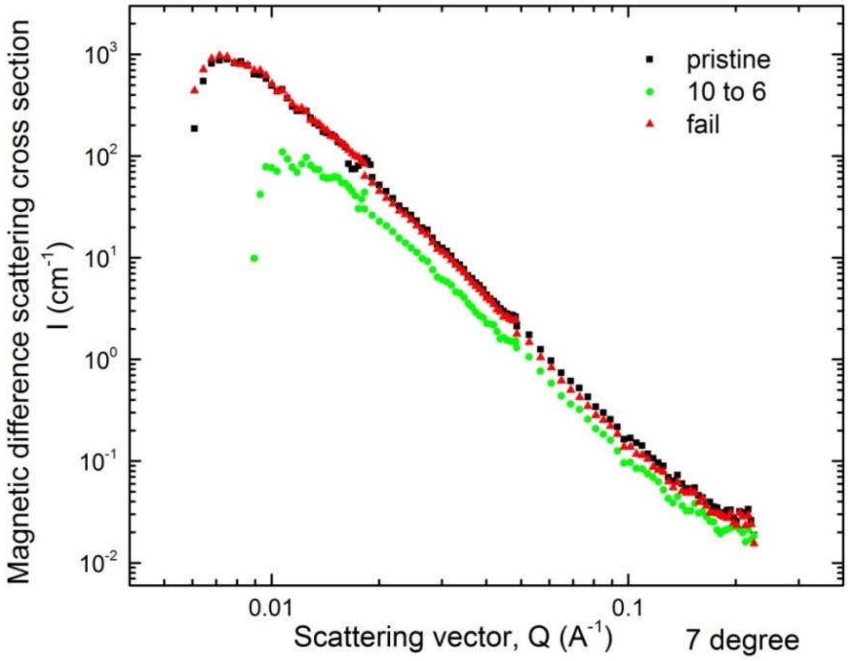

Image 46: Magnetic components of SANS profiles attained from “pristine”, “10 to 6” and “fail” specimens with 7-degree angle mask

This data treatment is more successful than the two previous tries. Especially, when at 7-degree mask, a relative big magnetic scattering difference between “10 to 6” and “pristine” steel is clearly shown in **image 46**.

At relative medium q (between from about 0.007 to 0.07), the data are well described by a straight line, indicating power-law scattering (referred to section 3.3.5), which will be discussed in detail with other fitting model later in section 6.2. In the high Q region of **image 45** and **image 46**, i.e. above about 0.1 $\dot{A}^{-1}$, the previously mentioned fitting models (referring to section 3.3.5) gives way to distinctly different behavior. According to the physcial theory, this part of Q smaller than 0.01 in **image 45** and **image 46** are supposed to be for the small size range of the microstructure, which is much smaller than void size. Therefore, this part fitting results are out of the discussion in this work.

Furthermore, for a specimen, during three different Q value range three lines with almost the same slope ratio are derived from the middle of the curves. And the vertical values (I values) of lines would be multiplied by the same number in oder to life up or lower the line to make sure that the three lines from the same specimen are connected with each other to be a whole line with a certain slope ratio. Actually, in our work, the magnetic scattering profiles at various degree masks (from 5 to 20 degrees) were tried to attain the good lines result, and the 5-degree and 7-degree masks are testified to be the two most suitable angle masks, those show the lines agreeing to a most suitable slope ratio.

In order to analyze these lines in **image 45** and **image 46** better, the ends of the lines, which don’t follow a certain slope ratio, have been cut off. In other words, the Q range from 0.019 to 0.18 of lines are conserved to be investigated further. (referred to **image 47** and **image 48**).

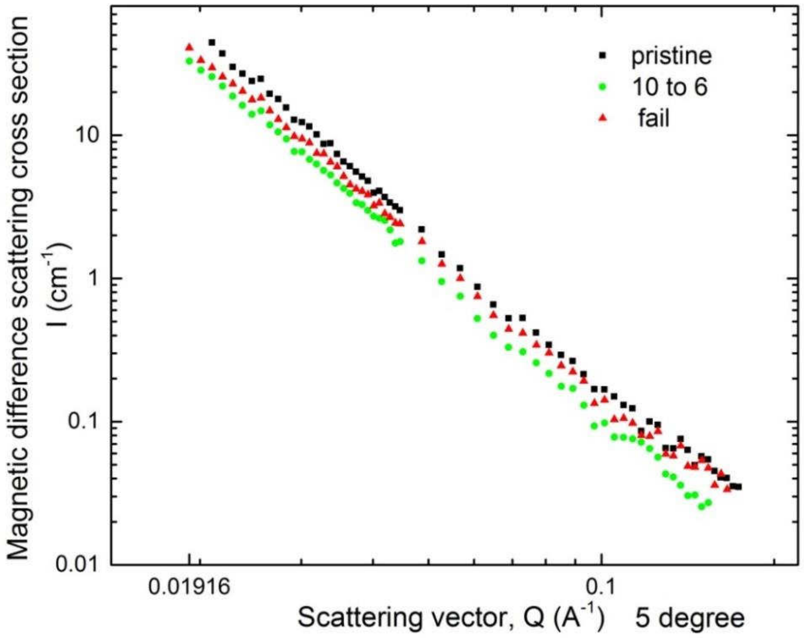

Image 47: Magnetic components of SANS profiles attained from “pristine”, “10 to 6” and “fail” specimens with 5 degree angle mask ($\mathbf{0.019 < Q < 0.18}$)

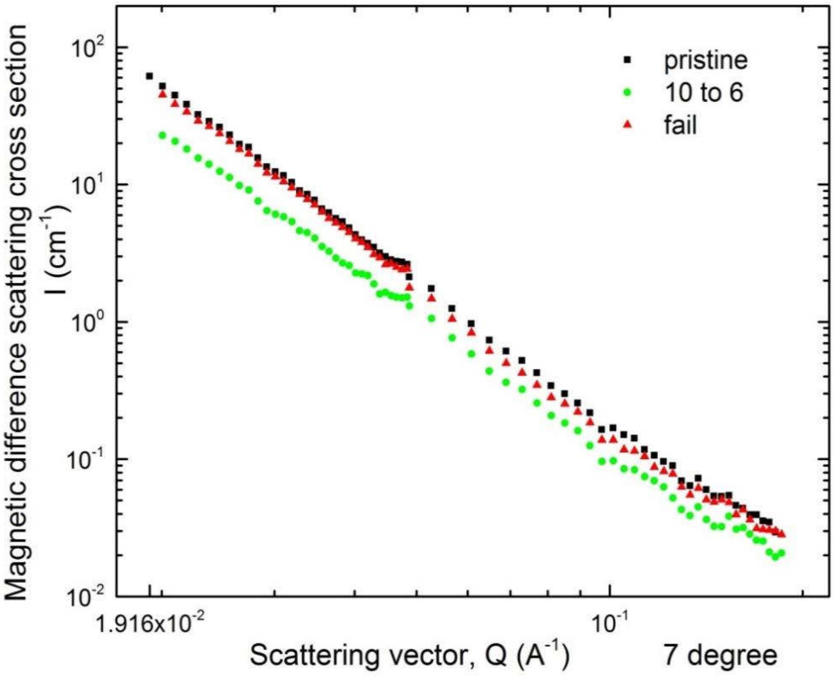

Image 48: Magnetic components of SANS profiles attained from “pristine”, “10 to 6” and “fail” specimens with 7-degree angle mask ($\boldsymbol{0.019 < Q < 0.18}$)

Due to the covering area of 5-degree horizontal-vertical mask is smaller than that of 7-degree mask, the number of detected neutron under 5-degree magnetic mask would be certainly lower than that under 7-degree magnetic mask. Therefore, the intensities of the lines, which are under 7-degree mask, are larger than those under 5-degree mask. Moreover, even using the 7-degree mask there might already be some magnetic contribution.

Nevertheless, except for the relative big difference between “10 to 6” and “pristine” steel at 7-degree angle mask, the differences between variants and “pristine” steel are not very big. Therefore, in order to make the changes of scattering curves more clear and easier for analysis, here under 5-degree (**image 49**) and 7-degree (**image 50**) magnetic masks, these two pictures show the differences values of the SANS intensity between the “10 to 6” and “pristine”, between the “fail” and “pristine” .

As expected, the relatively bigger difference between “pristine”, “10 to 6” and “fail” are attained and shown in **image 49** and **image 50**.

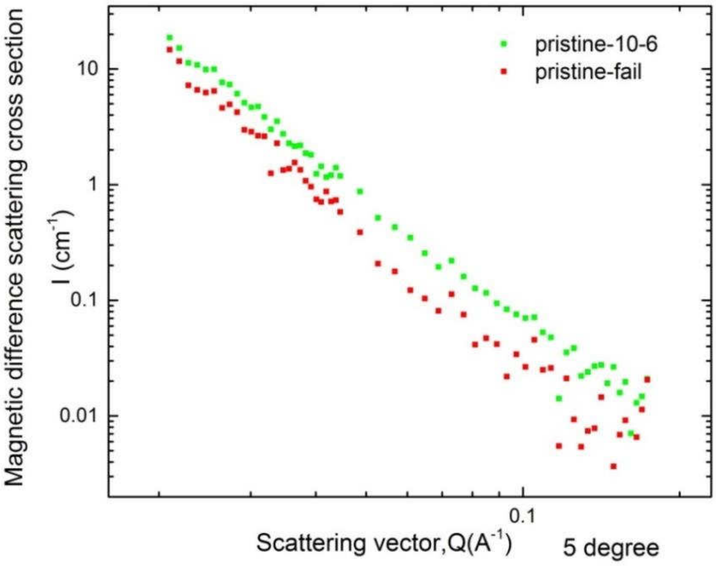

Image 49: Magnetic components of SANS profiles attained from “pristine-10 to 6” and “pristine-fail” with the 5-degree angle mask

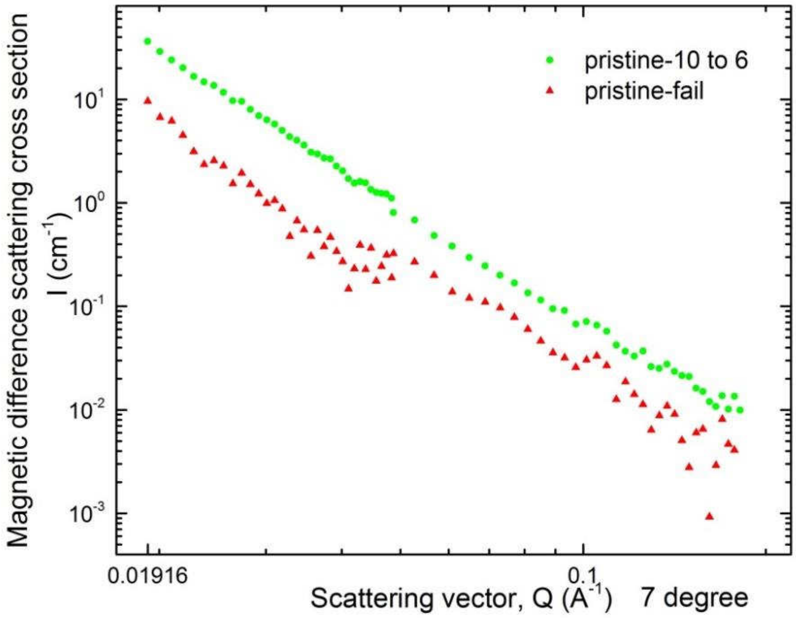

Image 50: Magnetic components of SANS profiles attained from “pristine-10 to 6” and “pristine-fail” with the 7-degree angle mask

In order to attain the specific parameters of the microstructures of the “10 to 6” and the “fail” using Sasview software, SANS scattering curves of “pristine-10 to 6” and “pristine-fail” with the 5-degree and 7-degree magnetic masks are fitted using different models.

5.3.4 Fitting images of SANS magnetic scattering profiles

In this fitting part, the absolute power law and sphere model are applied in this work. And the original points and the corresponding fitted curves are shown in from **image 51** to **image 58**. We can obviously see that the fitted curves from absolute power law model are shown relative smoother than those from sphere model as a result of different applied equations in different fitting models (the causes and relevant details are referred to section 3.2.5).

Form these fitting images, it can be seen that the fitting absolute power law shows a good adherence to the scattering of “pristine-10 to 6” compared to the sphere model, while for the scattering “pristine-fail” the sphere model possesses less fitting error.

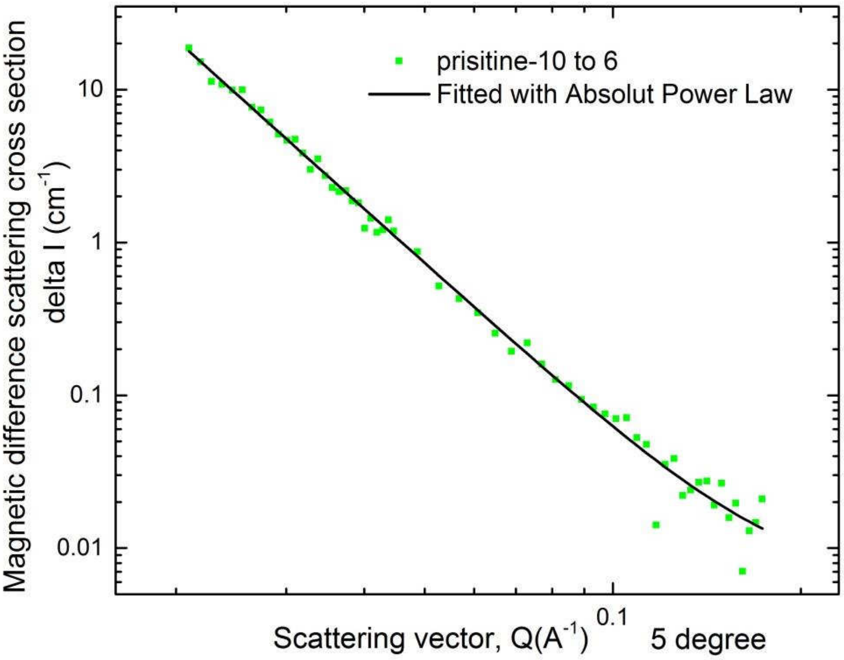

Image 52: SANS absolute power law fitting of “pristine-10 to 6" at 5-degree magnetic mask.

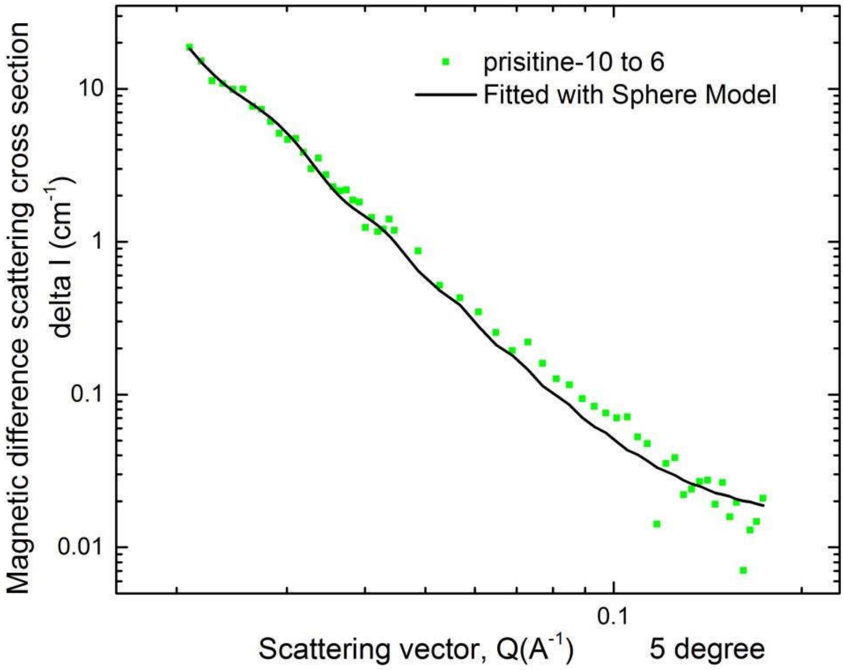

Image 53: SANS sphere model fitting of “pristine-10 to 6" at 5-degree magnetic mask

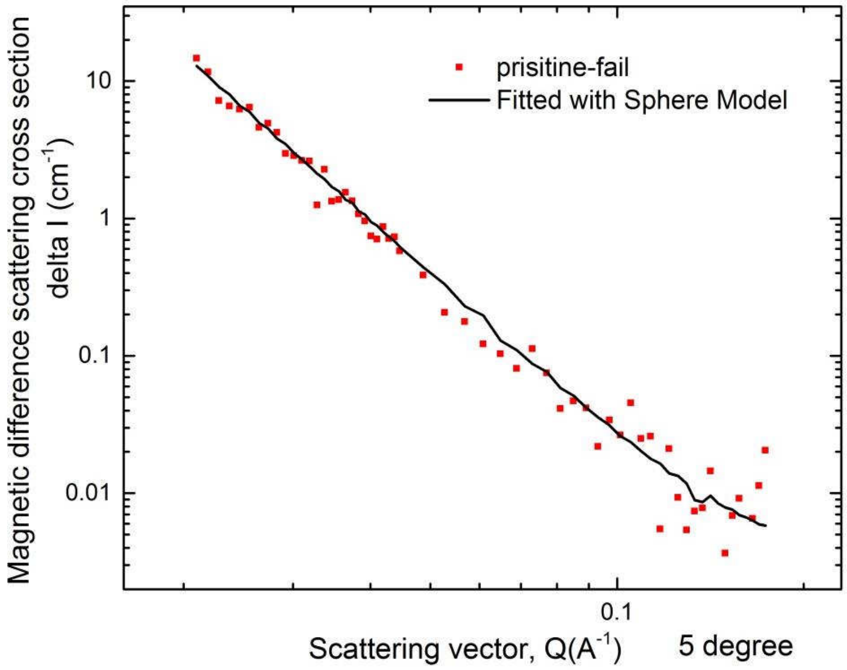

Image 54: SANS absolute power law fitting of “pristine-fail" at 5-degree magnetic mask.

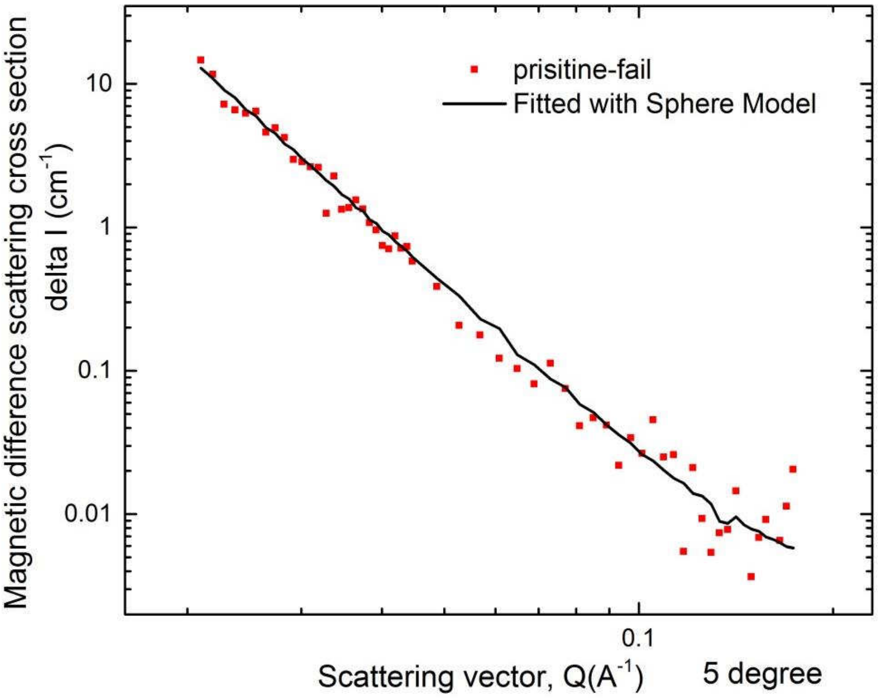

Image 55: SANS sphere model fitting of “pristine-fail" at 5 degree-magnetic mask

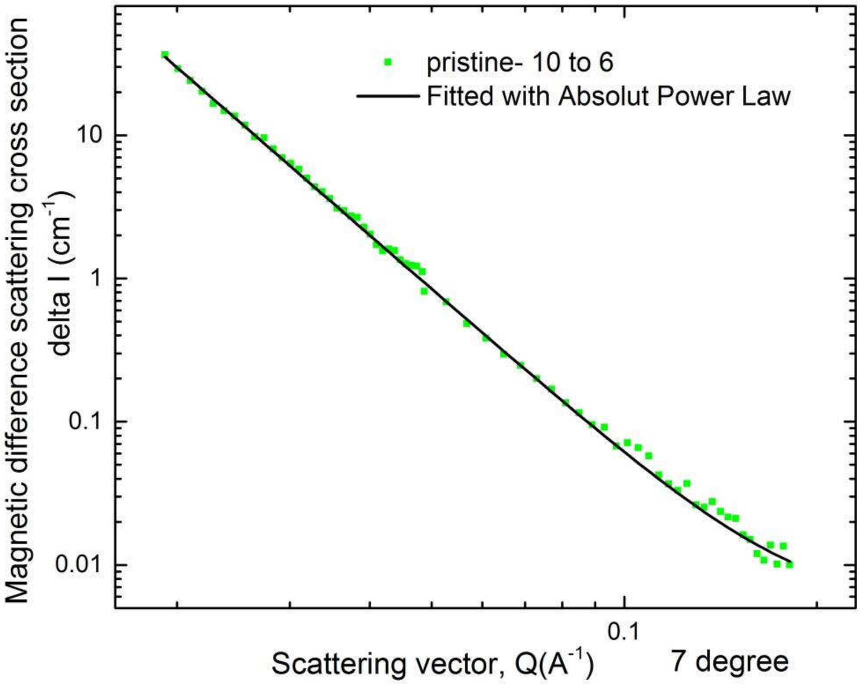

Image 56: SANS absolute power law fitting of “pristine-10 to 6" at 7-degree magnetic mask.

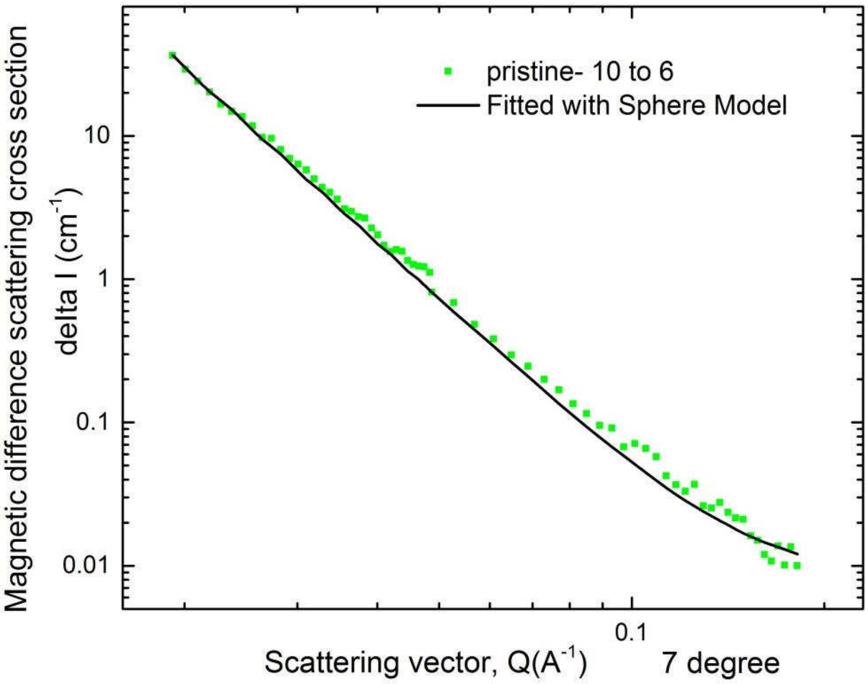

Image 57: SANS sphere model of “pristine-10 to 6" at 7-degree magnetic mask.

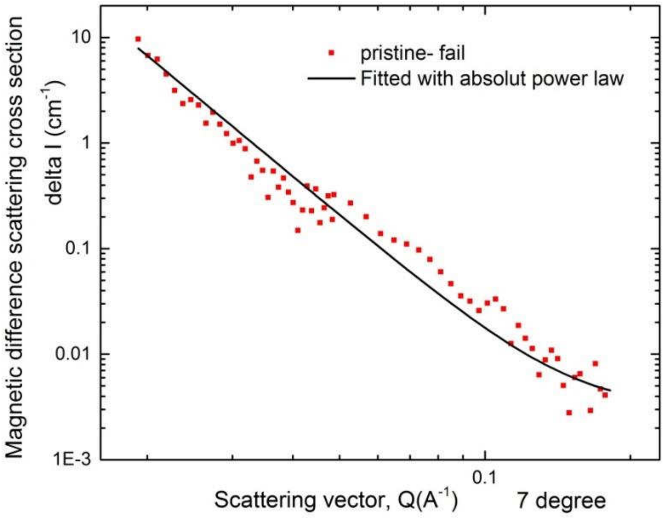

Image 58: SANS absolute power law fitting of “pristine-fail" at 7-degree magnetic mask.

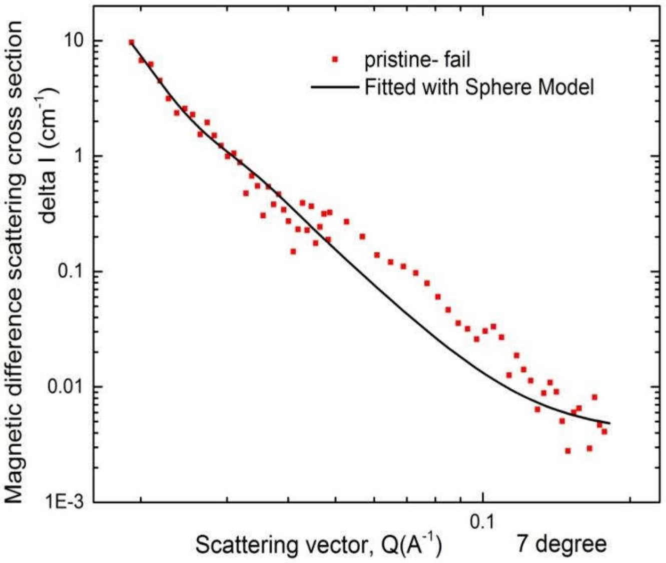

Image 59: SANS sphere model of “pristine-fail" at 7-degree magnetic mask.

5.3.5 Fitting results of SANS 2D profiles

With the help of the Sasview program, the fitted parameters can be derived accurately and shown in the following **table 12**, the physical meaning and other details of relevant parameters listed in the table are referred to section 3.4.5.

Table 11: The fitted result of absolute power law and sphere model

Fitting model		5 degree (h-v) mask		7 degree (h-v) mask	
		Pristine-10 to 6	**Pristine-fail**	**Pristine-10 to 6**	**Pristine-fail**
Absolut power law (shape-independent)	**BG (cm^{-1})**[1]	0.014 (fixed)	0.005 (fixed)	0.005 (fixed)	0.004 (fixed)
	m[2]	3.68 (±0.19)	4.37 (±0.32)	3.89 (±0.10)	4 (fixed)
	Scale[3]	1.16×10^{-5} $(\pm 8.27 \times 10^{-6})$	6.20×10^{-7} $(\pm 7.53 \times 10^{-7})$	7.24×10^{-6} $(\pm 2.90 \times 10^{-6})$	1.09×10^{-6} $(\pm 7.17 \times 10^{-8})$
Sphere Model (shape-dependent)	**BG (cm^{-1})**[6]	0.014 (fixed)	0.005 (fixed)	0.005 (fixed)	0.004 (fixed)
	Scale[7]	0.95 $(\pm 1.72 \times 10^{6})$	36.18 (fixed)	2.83 $(\pm 1.29 \times 10^{6})$	0.17 $(\pm 4.16 \times 10^{5})$
	Radius/ Å[8]	14.80 (±11.41)	67.08	56.20 (±7.80)	156.94 (±29.24)
	PD (cm^{-1}) [9]	1.82 (±1.46)	7.12×10^{5}	1.07 (±0.13)	0.25 (±0.09)
Volume fraction[4]		1.35×10^{-3}	7.31×10^{-4}	1.94×10^{-3}	4.72×10^{-4}
Special surface (cm^{-1}) [5]		$5.8(8) \times 10^{-4}$	$3.1(8) \times 10^{-5}$	$3.6(0) \times 10^{-4}$	$5.4(2) \times 10^{-5}$

[1] BG: Backgound; [2] m: Porod exponent; [3] Scale: Scale factor; [4] Volume fraction: [5] Special surface fraction: surface area per unit volume of sample; [6] BG: Background; [7] Scale: Scale factor volume fraction; [8] Radius: Radius of sphere particles; [9] PD: Polydispersion distribution of sphere model.

5.4 Grazing-incidence small-angle X-ray scattering (GISAXS)

5.4.1 GISAXS calibration using $AgC_{22}H_{43}O_2$

$AgC_{22}H_{43}O_2$ can show several specific rings in a recorded SAXS 2D pattern, usually it is used as a reference sample as the first Debey-Scherrer ring occurs at $= 0.088A^{-1}$. Thus it is a calibration sample for the following measurements of “pristine” steel and “fail” steel, in terms of sample-detector distance and center position of primary beam.

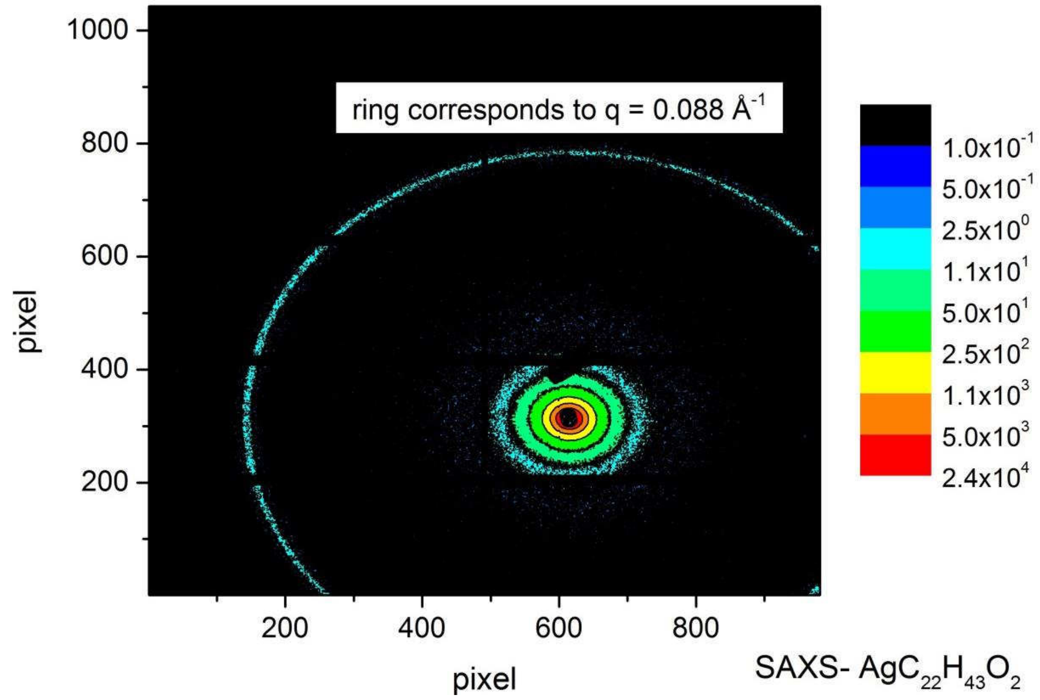

Image 60: The SAXS 2D pattern of $AgC_{22}H_{43}O_2$

In the 2D SAXS pattern of $AgC_{22}H_{43}O_2$ (see **image 59**), the number in the right colorful bar stands for the number of X-rays scattered by the sample, which are counted by a detector. Based on the right color bar, intensity in different position in SAXS pattern can be estimated.

5.4.2 GISAXS measurement of “pristine” and “fail” steel

Both pictures of **image 60** and **image 61**, since the detector used in this experiment is segmented, show homogeneous 10 pieces. And the peaks, whose directions are vertical, stand for the reflection part respectively.

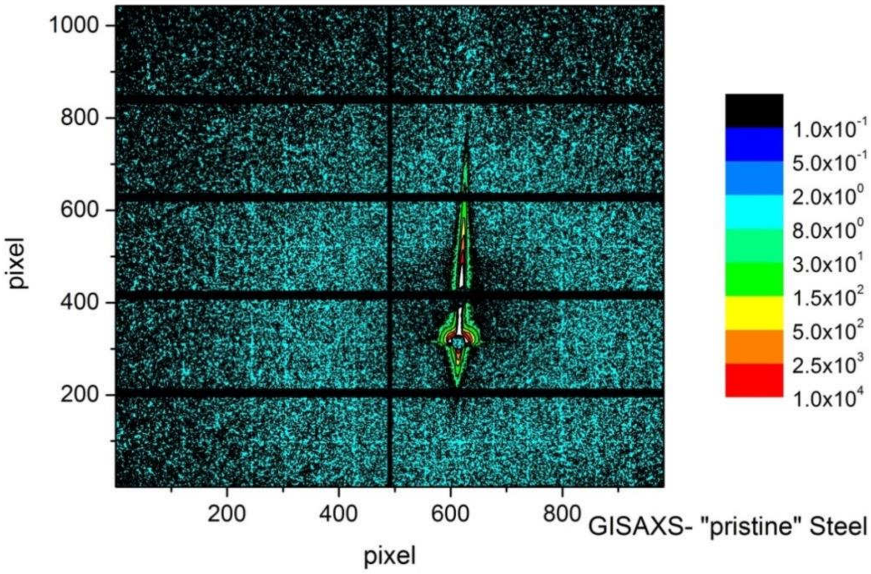

Image 61: The GISAXS 2D pattern of "pristine" steels

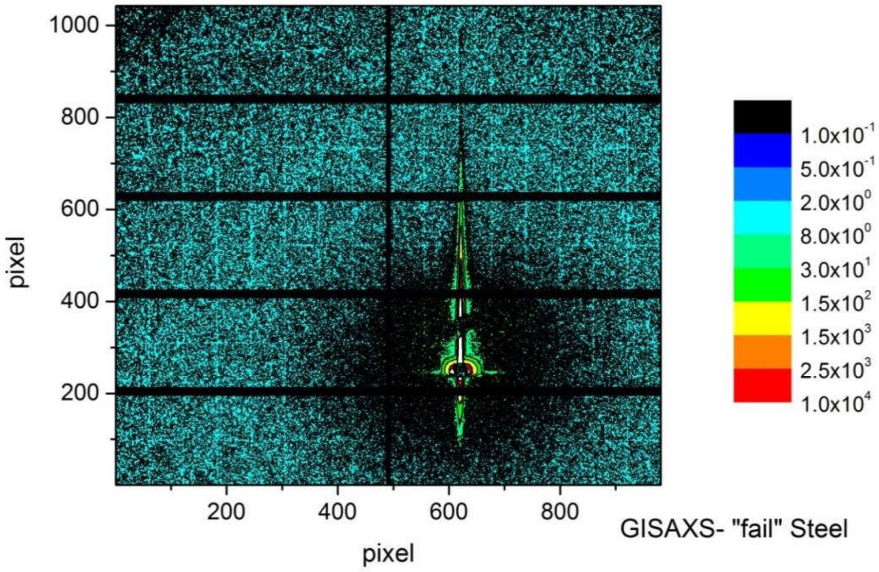

Image 62: The GISAXS 2D pattern of "fail" steels

However, both of the steel specimens have strongly absorbed the Ga Kα ray, which is a monochromatic source. And the strong absorption leads to deficient statistics. Although the energy discriminating detector levels were set above the Fe-florescence.

Within the range of the resulting statistics, there are hardly differences between the “pristine” steel and “fail” steel, as shown in **image 60** and **image 61**. Therefore, the structures, specially the cracks on the surfaces, are not detected. This is however expected as the fatigue starts within the volume for VHCF steel.

5.5 Resonant ultrasound spectroscopy (RUS)

5.5.1 Resonance profiles of $MnSi_{1.85}$, “pristine”, “10 to 6” and “fail” steel

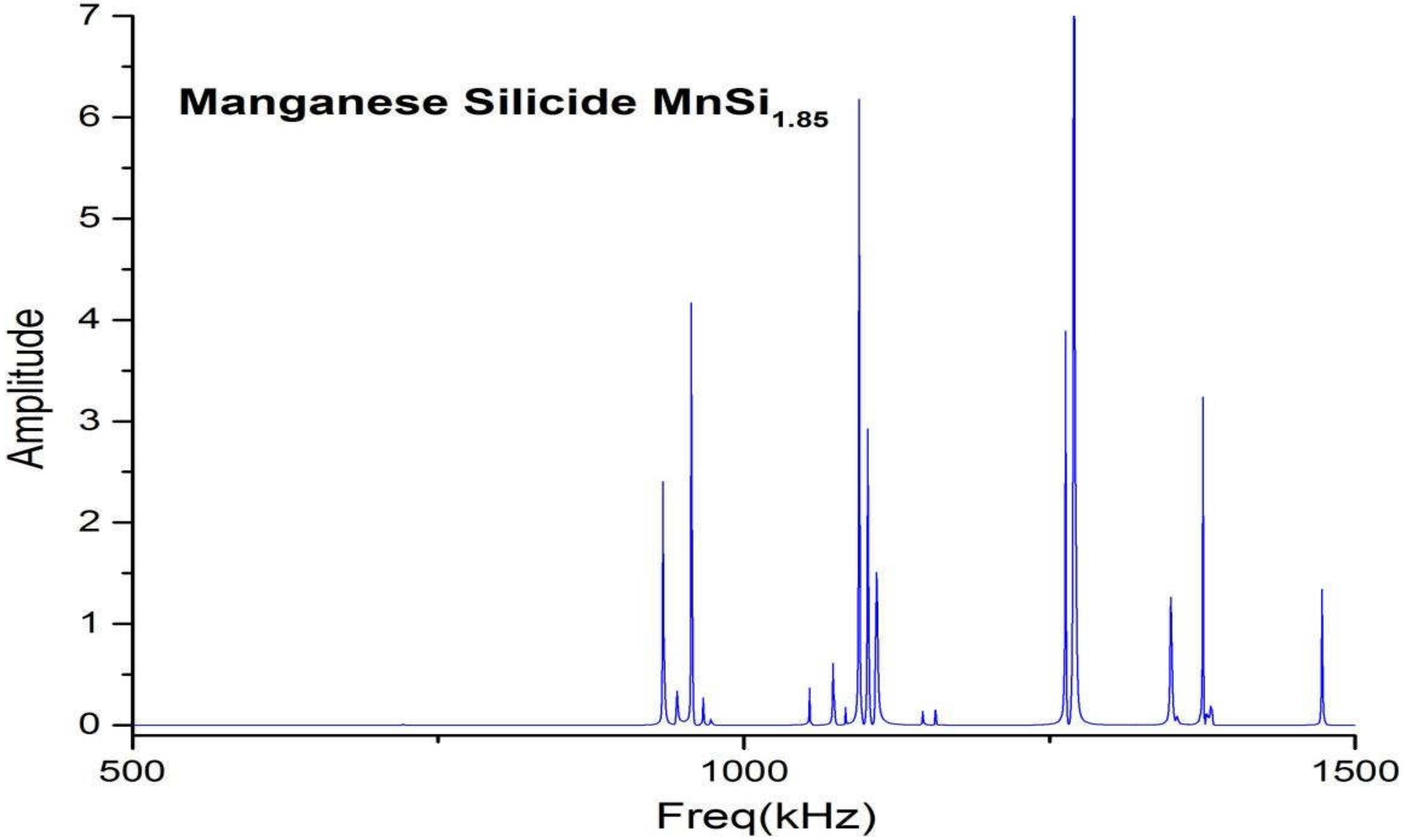

Image 63: Resonance profile of $MnSi_{1.85}$

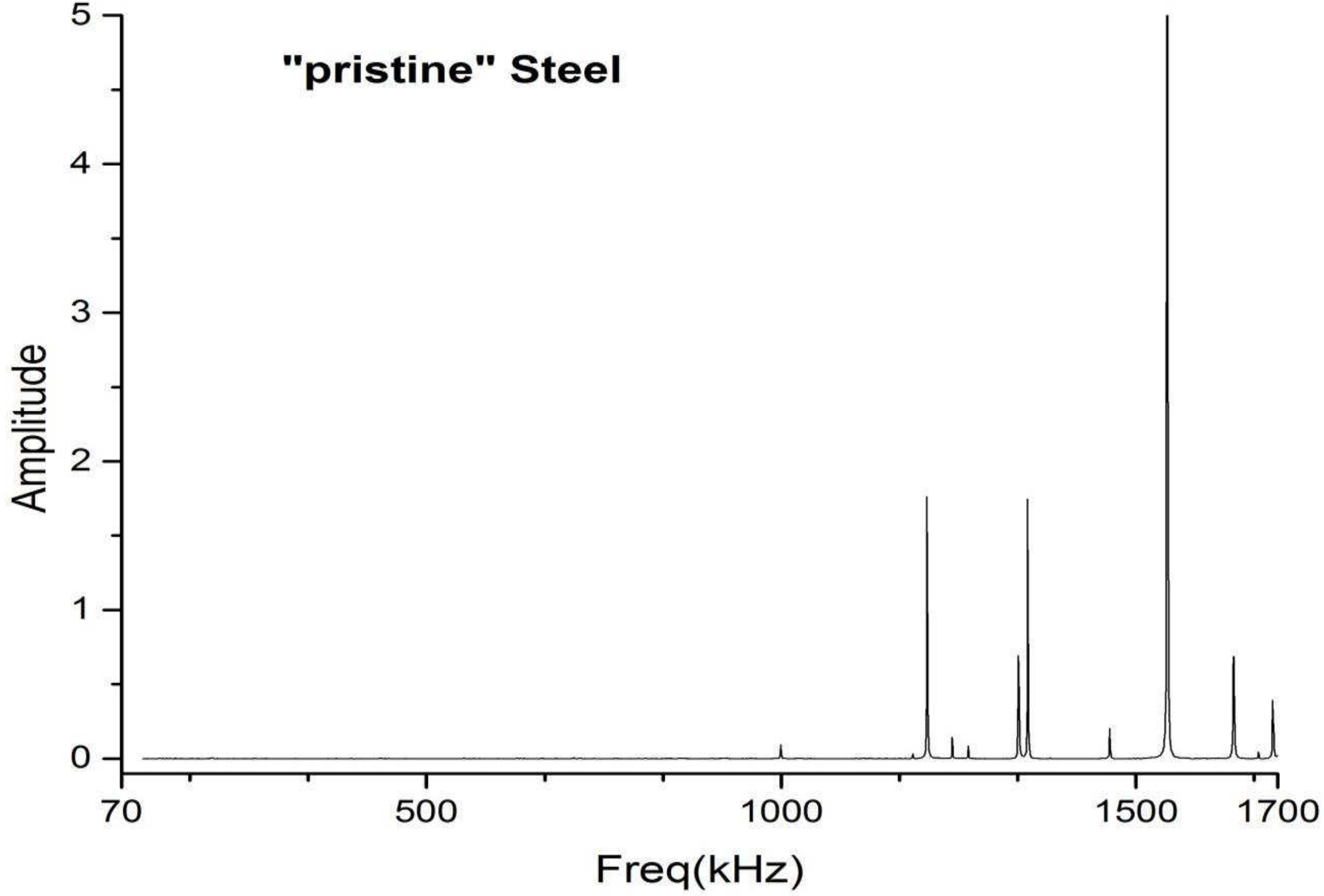

Image 64: Resonance profile of "pristine" steel

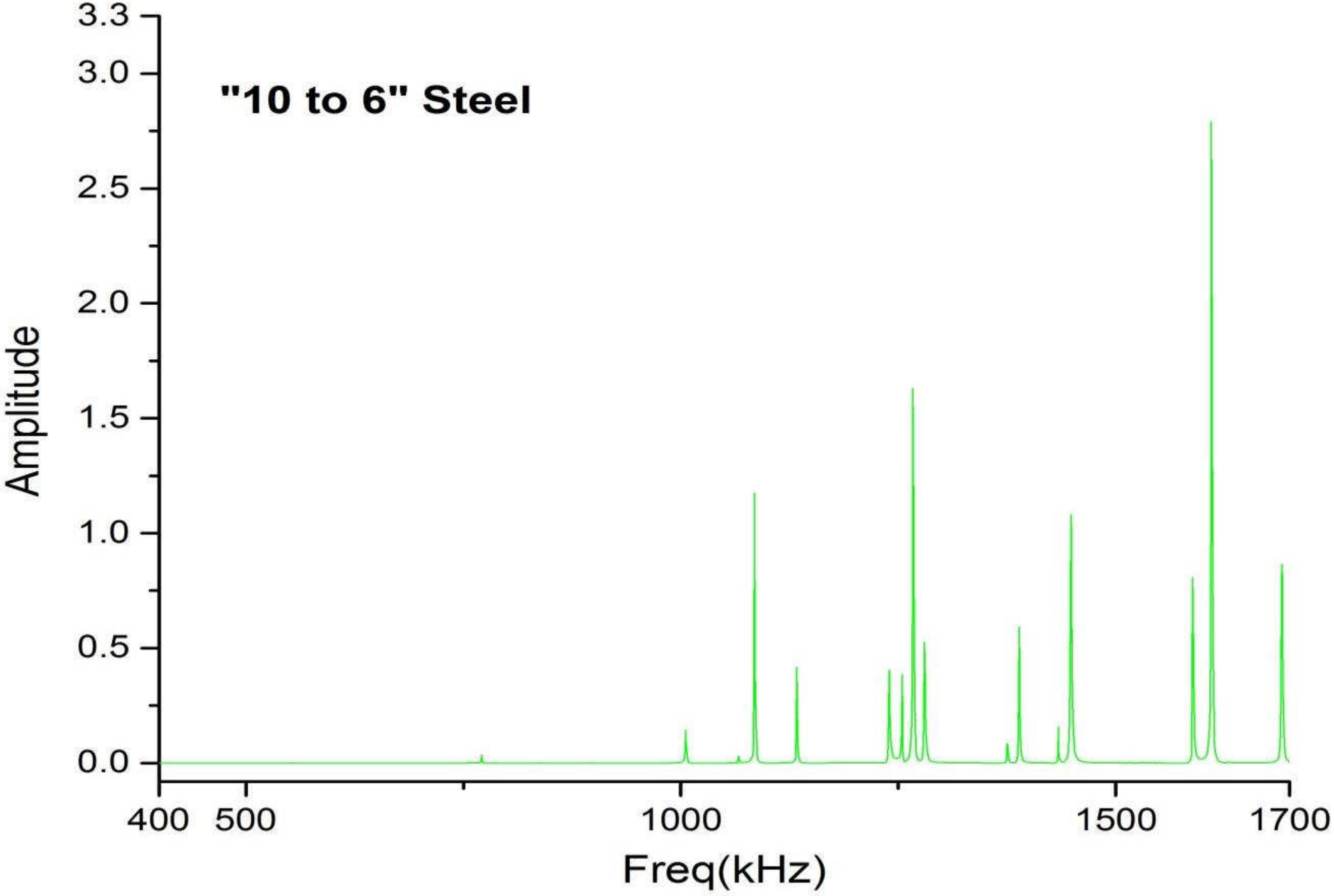

Image 65: Resonance profile of "10 to 6" steel

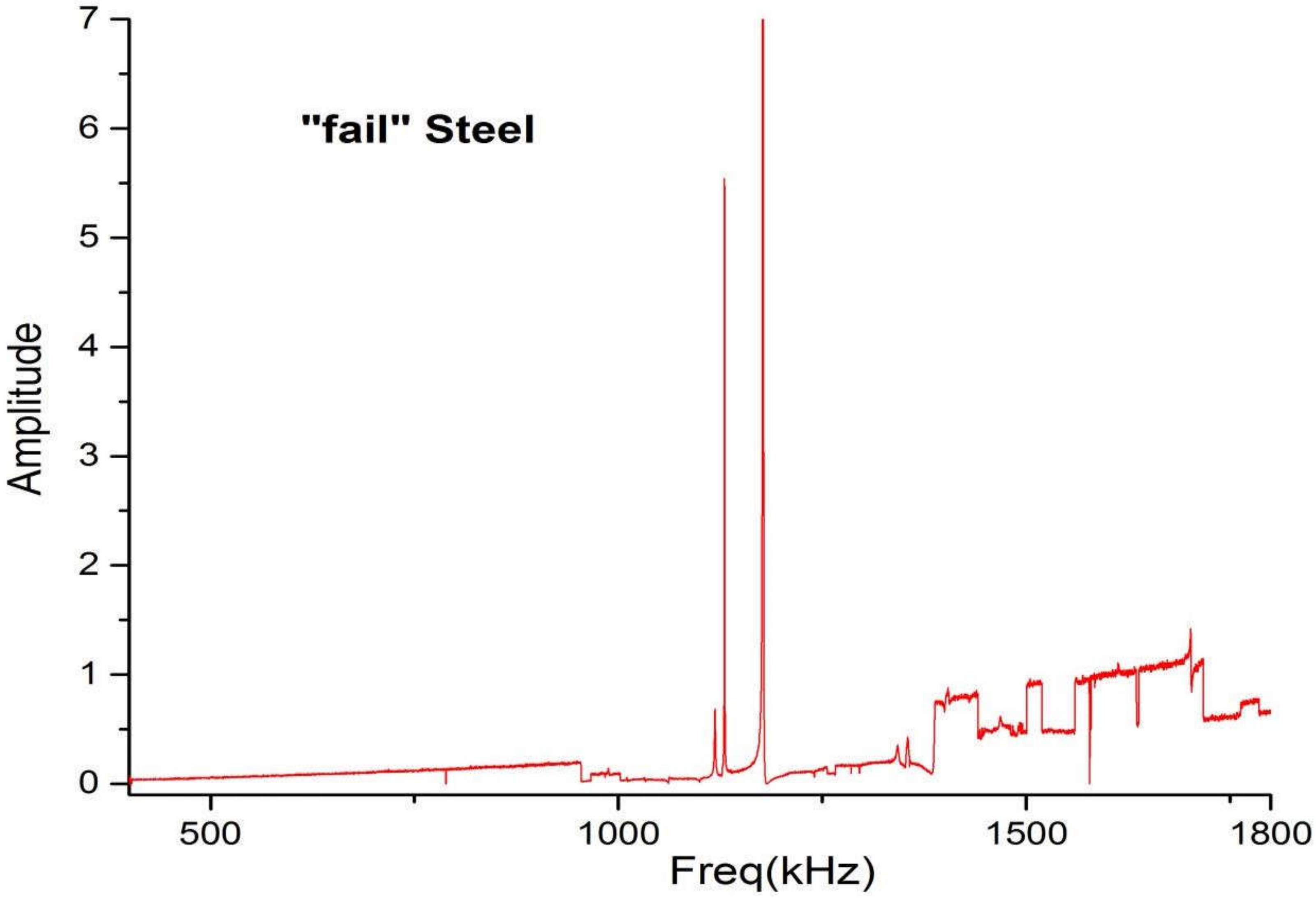

Image 66: Resonance profile of "fail" steel

From the upper images of RUS, we can see obviously that the "fail" steel resonant frequencies are not so normal like other specimens. It can be possible that, the microstructure in "fail" steel is destroyed and the order degree is decreased.

5.5.2 Resonant frequencies of $MnSi_{1.85}$, "pristine", "10 to 6" and "fail" steels

From the upper resonant ultra-sound spectroscopies, the resonant frequencies are extracted firstly and then fitted with the setting start values of the specimen's dimensions, density, the evaluated elastic moduli and shear moduli. For the standard specimen $MnSi_{1.85}$ and researched specimens of "pristine", "10 to 6" and "fail", the details of the extracted frequencies and their corresponding fitted values and errors are added in the following **table 13**-**16**.

Table 12: Measured and fitted frequencies of the rectangular parallelepiped manganese silicide $MnSi_{1.85}$. Also shown is the dependence of each frequency on each of the two fitted modulus, C_{11}(elastic modulus) and C_{44}(shear modulus).

n	f-expt	f-calc	%err	df/dc$_{11}$	df/dc$_{44}$
1	0	0.66827	0	--	0
2	0.721289	0.72597	-0.645	INC	0
3	0	0.897458	0	--	0
4	0	0.931652	0	--	0
5	0.933818	0.932406	0.151	INC	0.03
6	0.945019	0.940839	0.444	INC	0.13
7	0.957161	0.960627	-0.361	INC	0.02
8	0.966936	0.964425	0.26	INC	0.02
9	0.973535	1.009113	-3.526	INC	0.64
10	1.053782	1.060913	-0.672	INC	0
11	1.07333	1.075611	-0.212	INC	0.58
12	1.083166	1.079983	0.295	INC	0.59
13	1.090656	1.084678	0.551	INC	0.01
14	1.104522	1.103011	0.137	INC	0.02
15	1.10561	1.114746	-0.819	INC	0.3

16	1.14628	1.120011	2.345	INC	0.3
17	1.156559	1.168106	-0.988	INC	0.31
18	1.262905	1.230514	2.632	INC	0.65
19	1.269927	1.251423	1.479	INC	0.64
20	1.349206	1.319154	2.278	INC	0.02

Table 13: Measured and fitted frequencies for the rectangular parallelepiped “pristine” steel. Also shown is the dependence of each frequency on each of the two fitted modulus, C_{11}(elastic modulus) and C_{44}(shear modulus).

n	f-exp	f-theor	%err	df/dc$_{11}$	df/dc$_{44}$
1	0.706686	0.702251	0.631	0	1
2	0.922358	0.933309	-1.173	0.16	0.84
3	0.998709	0.999402	-0.069	0.21	0.79
4	0	1.014935	0	0	0
5	1.09994	1.070984	2.704	0.02	0.98
6	0	1.174881	0	0	0
7	1.182541	1.183108	-0.048	0.02	0.98
8	1.204753	1.188663	1.354	0.05	0.95
9	0	1.212823	0	0	0
10	1.239765	1.234278	0.445	0.06	0.94
11	1.263495	1.290334	-2.08	0.14	0.86
12	1.334231	1.307364	2.055	0.11	0.89
14	1.346565	1.341925	0.346	0.22	0.78
15	1.378597	1.411676	-2.343	0.11	0.89
16	1.464037	1.479597	-1.052	0.04	0.96
17	1.543731	1.523248	1.345	0.29	0.71
18	1.569959	1.571288	-0.085	0.35	0.65
19	0	1.594986	0	0	0
20	0	1.602646	0	0	0

21	1.636884	1.637822	-0.057	0.1	0.9
22	0	1.661229	0	0	0
23	1.671657	1.665303	0.382	0.46	0.54

Table 14: Measured and fitted frequencies for the rectangular parallelepiped "10 to 6" steel. Also shown is the dependence of each frequency on each of the two fitted modulus, C_{11} (elastic modulus) and C_{44} (shear modulus).

n	f-exp	f-theor	%err	df/dc$_{11}$	df/dc$_{44}$
1	0.772209	0.759524	1.67	0	1
2	1.008234	1.020983	-1.249	0.13	0.87
3	1.064347	1.055005	0.886	0	1
4	1.083588	1.096137	-1.145	0.21	0.79
5	1.131829	1.140151	-0.73	0.03	0.97
6	1.238339	1.233954	0.355	0.46	0.54
7	1.253981	1.256476	-0.199	0.17	0.83
8	1.266516	1.258576	0.631	0.02	0.98
9	1.280704	1.279294	0.11	0.03	0.97
10	1.300257	1.304461	-0.322	0.02	0.98
11	1.375768	1.368153	0.557	0.2	0.8
12	1.387817	1.384698	0.225	0.1	0.9
13	1.434137	1.415677	1.304	0.23	0.77
14	1.447557	1.478454	-2.09	0.12	0.88
15	1.58733	1.594215	-0.432	0.32	0.68
16	1.609164	1.59793	0.703	0.03	0.97
17	1.629737	1.630851	-0.068	0.37	0.63
18	1.690462	1.674282	0.966	0.48	0.52

Table 15: Measured and fitted frequencies for the rectangular parallelepiped "fail" steel. Also shown is the dependence of each frequency on each of the two fitted modulus, C_{11} (elastic modulus) and C_{44} (shear modulus).

n	f-exp	f-theor	%err	df/dc$_{11}$	df/dc$_{44}$

1	0	0.572397	0	0	0
2	0.787813	0.773876	1.801	0.07	0.93
3	0	0.814542	0	0	0
4	0	0.832756	0	0	0
5	0	0.870105	0	0	0
6	0	0.958521	0	0	0
7	0	0.969641	0	0	0
8	0.984926	0.990415	-0.554	0.07	0.93
9	0.98813	0.994738	-0.664	0.25	0.75
10	1.010678	1.001814	0.885	0.02	0.98
11	1.061298	1.061117	0.017	0.09	0.91
12	1.099835	1.066678	3.108	0.04	0.96
13	1.118575	1.109731	0.797	0.11	0.89
14	1.130458	1.14752	-1.487	0.04	0.96
15	1.176564	1.206364	-2.47	0.02	0.98
16	1.285851	1.260144	2.04	0.15	0.85
17	1.294415	1.305919	-0.881	0.18	0.82
18	0	1.316645	0	0	0
19	1.342515	1.336417	0.456	0.05	0.95
20	1.352426	1.350761	0.123	0.28	0.72

During initial generated frequency range in the experiment, it is sometimes difficult to detect the resonant phenomena due to very low resonant frequency. Additionally, some other causes such as not-parallelepiped specimen geometry or observation carelessness can also lead to the missing of experimental resonant frequencies. In this case, the zero number (see **table 13**-**16**) is applied instead of the missing frequencies, which can be recognized by the computer. In this way the fitting process can be rightly carried out to obtain expected fitted moduli.

5.5.3 RUS fitted elastic constants of $MnSi_{1.85}$, “pristine”, “10 to 6” and “fail” steel

These final fitted elastic modulus and shear modulus, compared with literature data, are presented in **table 17**.

Table 16: RUS fitted elastic modulus (E) and shear modulus (G) of the manganese silicide $MnSi_{1.85}$ as well as literature data [Ben]

	Experiment(fitted)	**Lit.data**	**Relative error(%)**
E(GPa)	277.25	284	-2.4
G(GPa)	104.91	106	-1.0

The final fitted values of the elastic moduli, the shear moduli of these three specimens and their individual root mean square (abbreviated RMS) are attained and shown in the below **table 18**.

Table 17: RUS fitted elastic modulus and shear modulus of “pristine”, “10 to 6” and “fail” steels as well as their RMS Error.

	RUS		
	“pristine”	“10 to 6”	“fail”
Elastic modulus (GPa)	220.18	240.07	287.30
Shear modulus (GPa)	76.79	81.31	74.86
RMS Error/%	1.29	0.89	1.46

Based on **table 18**, we can see that the highest elastic moduli’s value occurs to the “fail”, while the “pristine” under no cyclic load possesses the lowest elastic. The decline trend can’t be found in the elastic moduli of the specimens with the increasing cyclic load, even when the specimen’s macro-structural deformation starts, i.e. “fail”. Contrary to this trend, the shear moduli trends to reduce earlier than elastic moduli. With the 76.79 shear moduli of “pristine”, the 81.31 of “10 to 6” and the 74.86 of “fail”, the decline trend of shear moduli is already observed in this work.

6 Discussion

6.1 Mössbauer spectroscopy

The obtained Mössbauer spectra were presented previously in **image 40**. In the figure, component spectrums form the basis for a description of the individual structural phases. To obtain the phase fractions, the sextet and doublet components of the spectra were isolated and integrated numerically, i.e. their spectral weight or area was calculted. The corresponding amounts of different phases in the matrix are shown in **table 19** and **table 20**.

Table 18: The analysis of components and their individual fractions by using TMS

Component	Phase	Fraction (%)
1	Martensite	95
2		
3	iron silicide based phase	5

Table 19: The analysis of components and their individual fractions by using CEMS

Component	Phase	Fraction (%)
1	Martensite	95
2		
3	iron silicide based phase	5

The spectra in **image 40** clearly show the two patterns of the sextets and one pattern of the doulet. Firstly, this spectrum shows a broadening of the outer lines of the sextet with respect to the inner lines. This broadening phenomenon can be explained with a distribution of hyperfine magnetic fields, which is a typical feature of martensite phases [Var92]. Here they are requested to by components 1 and 2. These two components do not actually represent two distinct phases, but are rather necessary for the fitting process, as martensite usually exhibits a broad distribution of hyperfine fields [Bil01]. Thus both of these components confirm the major martensitic nature of the steel. Notably, an austenitic phase cannot be verified or is below detection limit. Component 3, exhibits a rather strong quadrupole splitting which might point to an iron silicide based phase [Fan94]. However, the actual Si content is too low in order to explain the contribution of component 3, which is about 5% to the overall spectrum whereas the potential $FeSi$ would contribute less than 1%. Thus, we attribute this significant doublet to the incorporation of Fe in Cr carbides, which may exhibit such strong quadrupole split spectra [Var92].

According to the previous description on the microstructure in the literature [Til13], the microstructure consists of a relative high martensitic component, where Cr-carbides finely distributed. The analysis outcome of this Mössbauer spectroscopy agrees mostly with this description.

From **image 39**, a comparison between the transmission and conversion electron Mössbauer spectroscopy measurements of a pristine sample is presented. The overall agreement is good although there is some difference at about 4 mm/s. This might be related to the sample preparation procedure for TMS, which might have introduced some impurities from the tools. However, this should have also an effect on the other peak positions, which is clearly not the case. Additionally, the phase analysis of Mössbauer spectroscopy itself is semi-quantitive.

All in all, one can conclude that both Mössbauer spectroscopy techniques yield essentially the same information for this specific steel. Notably, both Mössbauer spectra are affected by a "magnetic texture", which is manifest in the intense peaks at -3 mm/s and 3 mm/s, which should be weaker without "magnetic texture" [Phil11]. This means that during sample preparation for TMS, the powder particles have not been contaminated.

6.2 Small angle neutron scattering (SANS)

In **image 49** and **image 50**, we can see that the values of the differences between the “10 to 6” and “pristine”, between the “fail” and “pristine” are located in the same range of scattering cross section when 5-degree and 7-degree magnetic angle mask are used, even though the intensity using the 5-degree magnetic mask would be certainly lower than that under 7-degree magnetic mask in the previous discussion. This phenomenon proves the fact, the magnetic characters of specimens doesn't change significantly with the different angle masks.

Additionally, both profiles representing the difference between the “fail” and “pristine” with 5-degree and 7-degree magnetic masks are not two smooth lines, compared with the profiles representing the difference between the “10 to 6” and “pristine”. It can be derived that “10 to 6” has a better ordered magnetic structure, whereas “fail” is characterized with a relatively disorder magnetic microstructure on the different Q value range. According to that analysis, the conclusion can be reached, that the micro-structure is significantly changed as the original specimen or one with lower cycle number.

Apart from the other structural entities affecting the small angle scattering regime, internal cracks, if sufficient in number, could contribute to the small angle scattering. Generally, pores in magnetic materials affect the permeability via the decrease in magnetization per unit volume and via the increase in the demagnetizing field [Hid77]. In the course of a fatigue test, various voids and even cracks can be created and developed. Thus, in “10 to 6” and “fail” steel body there are more cracks existing. Furthermore, both **image 47** and **image 48** indicate “pristine” steel has a magnetic scattering relative higher by an order of magnitude in “10 to 6” and “fail” steel.

After fatigue test “10 to 6” steel is supposed to have a relative uniform cracks distribution, which has a similar demagnetization effect as small pores uniformly distributed in a solid body based on the theory as concluded in [Hid97]. Moreover martensite transformation due to mechanical deformation could also probably contribute to the big reduction of magnetic scattering for “10 to 6”. However, the contribution made by martensite transformation can be ignored due to very little deformation occurring to the specimen during fatigue test.

Moreover, in the same Literature [Hid97] it was proved that specimens with small pores distributed uniformly throughout the bulk have much more demagnetizing factor than those with a small number of pores of large size. Furthermore, the demagnetizing factor is almost proportional to porosity. In our work, the magnetic scattering of “10 to 6” steel is relative smaller than that of “fail” steel, which is similar to the phenomena in the previous work [Hid77]. An increasing cyclic loading number in fatigue test doesn’t give rise to further increasing magnetic scattering cross section. This abnormal phenomenon might be explained that void coalescence occurs in the microstructure of specimens during the fatigue loading, which has also a good adherence to the previously discussed theory [Hid97].

Based on the Absolute power law fitting model, with an exception of the fixed m value with 4 in the fitting process of “pristine-fail” under 7-degree magnetic mask, other fitted values of m are around 4. And value of the exponent provides information on the nature of the scattering centers. This m≈ 4 case (i.e.,$I \propto Q^{-4}$, the Porod law) is commonly observed [Wil09], describing the scattering from an assembly of three dimensional (3D) objects with “smooth” surfaces. Three dimensional objects with “rough” or “wrinkled” surfaces on the other hand are known to result in m < 4, this case occurs to the “pristine-10 to 6” fitting under both masks. Furthermore, the special value of m = 3 marking the transition between surface and volume fractals [Kre09]. In our case the line shown in the “pristine-10 to 6” under 7-degree magnetic mask has m = 3.89, indicating good adherence to the Porod law expected for 3D scattering centers with smooth surfaces.

For the sphere fitting model, the attained radius of “pristine-fail” is significant larger than that of “pristine-10 to 6”, that can illustrate the voids size in “fail” specimen is larger than the “10 to 6”, which shows a good adherence to the void coalescence exists in the procedure of forming a crack during the fatigue test. In addition, the SANS curves are fitted to attain the specific surfaces fraction. Since SANS is sensitive only to a certain length scales determined by accessible Q or angular range, the decline of the specific surface fraction’s value can also prove indirectly the void coalescence phenomenon. Moreover, due to extremely small absolute values of intensity, the relative error increases strongly in fitting procedures. Therefore, the fitted radii are ignored in the discussion.

6.3 Grazing-incidence small-angle X-ray scattering (GISAXS)

Within the range of the resulting statistics, there are hardly any differences between the “pristine” steel and “fail” steel, as shown in Image. Therefore, the structures, specially the cracks on the surfaces, are not detected. However, this is also not expected as the VHCF occurs and starts within the volume of a material.

6.4 Resonant ultra-sound spectroscopy (RUS)

Considering the fitted result in **table 19**, the elastic moduli of the X10CrNiMoV12-2-2 steel would increase as the cyclic load number increases. One possible factor is work hardening [Ble12]. This strengthening occurs because of dislocation movement and dislocation generation within the crystal structure of the material. And this situation in our work is close to the processes, which are known as cold working or cold forming processes. During cold working or cold forming processes the specimens are shaped at a temperature below its recrystallization temperature, usually at the room temperature, which is close to fatigue test’s temperature in this work.

Although the shape degree occurred in the fatigue test was much smaller compared to the normal cold forming, the number of dislocations caused by the cyclic loading cannot be ignorant, which can significantly resist to the new dislocations formation and movement. Furthermore, these dislocations accumulate, interact with each other, and serve as pinning points or obstacles that significantly impede their motion [Ble02]. This leads to an increase in the elastic constant and a subsequently decrease in the shear moduli, which can also good explain why the shear moduli starts to decline after the 2×10^6 cyclic loading. Additionally, the low-angle grain boundaries subsequently formed by a relative high concentration of dislocations will cause the Hall-Petch effect of the sub-grains [Wil12], which can also increase the materials’ strength but decrease its ductility.

The other possible factor is the positive effect cause by the deformation on the martensite transformation. The stress field of a plastic or elastic deformation is superimposed on the stress field of the martensite nucleus, and strengthens it.

Moreover the increased hardness and brittleness of steels after quenching from austenite is the result of martensite formation [Ble02]. Therefore the cyclic loading will also result in an increase of elastic moduli and a decrease of shear moduli. However, comparing to the work hardening effect, the martensite transformation plays a relative insignificant role due to the small amount of retained austenite.

Thus, we confirmed that not only the elastic constant but also shear constant of the martensitic steel are sensitive to the cyclic load number, and the work hardening is the dominant factor that increases the elastic constants and decreases the shear constants after a certain cyclic number.

7 Conclusions and prospects

The microstructures properties and elastic moduli of these three specimens “prisitne”, “10 to 6” and “fail” steels and their elastic moduli were studied with several methods using laboratory and large-scale facilities.

In summary, we have studied the microstructural phases of specimen by using Mössbauer spectroscopy and the incipient fatigue processes due to cyclic loading, especially the nanometer sized cracks formation in specimen body, with method of small angle neutron scattering (SANS). Moreover, the microstructures during cracks formation was further qualified with Grazing-incidence small angle X-ray scattering (GISAXS), however, the aim can’t be reached because of the insufficient statistics. Meanwhile with the research ultra-sound spectroscopy the elastic constants of the specimens in different cracks formation phases are measured in order to find out the relationship between the elastic constants and load cycle numbers.

In Mössbauer spectroscopy analysis, only the martensite phase with an amount of about 95% is determined and the incorporation of Fe in Cr carbides is assumed to exist in the body. This assumption is close to the description of X10CrNiMoV12-2-2 steel microstructure after heat treatment in literature [Til13].

In SANS measurement, only magnetic scatterings of these specimens, which show relative big profile differences, are investigated. Compared to “pristine”, the microstructure in “10 to 6” after 10^6 load cycles is changed and characterized probably with a relative high amount of small cracks, which are uniformly distributed in the body. Again compared to “pristine”, the abnormal magnetic scattering similarity between “fail” and “pristine” can be explained by the crack coalescence phenomenon, which probably can reduce the demagnetization degree caused by pores distributed in specimen. Additionally, compared to “10 to 6” the relative smaller specific surface fraction of “fail” can be explained with SANS measurement sensitivity limitation in a certain length scales. Probably because the crack size were growing up and eventually out of the length scale limitation, thus fitted parameters, such as specific surface fraction and so on, cannot be directly used to analyze the real situation in microstructure. However, these parameters can be a clue to indirectly confirm the crack coalescence phenomenon occurred during the load cycles from 10^6 to 2.7×10^6 in fatigue test, which can explain the decreasing specific surface fraction with increasing load cycle number. However, the quantitative analysis on early-stage crack formation cannot be realized from the SANS result analysis. Because very few literatures on studying crack microstructure in materials by using SANS and even less literatures especially on steel microstructure are available such as [Kim88,Pot88], the only qualitative conclusion and relevant assumptions can be abstracted to describe the crack formation at early stage in the investigated steel during fatigue test. For the further work, also extra scanning electron microscope (SEM) photos on the cross section of “pristine”, “10 to 6” and “fail” can be made to observe the crack formation.

For GISAXS experiment, insufficient result data cannot identify the microstructure and surface differences between “pristine” and “fail” steels due to the strong resource ray absorption of the specimen bodies. As a result, no useful conclusion can be reached in this part measurement. It might be the cause that the thickness of specimens is so big that the rays cannot penetrate the bodies. For the further investigation in GISAXS, the specimens, which should be grinded into a thin disc, will be set in GISAXS measurement in order to obtain a better result.

Elastic moduli of the martensitic X10CrNiMoV12-2-2 steel cubic showed a correlation with the cyclic loading number, and below 2.7×10^6 cyclic loading number, the elastic moduli increased as the cyclic number increases. However, the shear moduli have already a decline tendency when the cyclic number arrived 2×10^6. These phenomena can be good explained with cold work hardening mechanisms. However, in order to determine the exact load cyclic number, at which elastic and shear moduli start to decrease, more study by using RUS measurement at different cyclic numbers on specimens is needed.

8 List of references

[Adr95]: Adrian, R.; “Reduction of Data from SANS Instruments”
Nato ASI Series Volume (1995) 451, pp 93-105

[Aub98]: Aubertin, F.; Abada, L.; Gonser, O.; “Carbon and nitrogen in steel”
Hyperfine interactions (1998) Vol. 111, pp. 201-204

[Bal08]: Bala, P.; Krawczyk, J.; Hanc, A.; “The Mössbauer Spectroscopy Studies of ϵ to Cementite Carbides Transformation during Isothermal Heating from As-Quenched State of High Carbon Tool Steel”
Acta physica polonica A (2008) Vol.114, No.6

[Bat97]: Bathias,C.; Alami, K.; “Influence of mean stress on ti6a14v fatigue crack growth at very high frequency”
Engineering Fracture Mechanics (1997) 56 255-264

[Bay06]: Bayraktar, E; Garcias, I.; Bathias, C.; “Failure mechanisms of automotive metallic alloys in very high cycle fatigue range”
International Journal of Fatigue 28 (2006) 1590-1602

[Ben14]: Benedikt,K.; Raphael, H.; “Void formation and initial stages of very high cycle fatigue in turbine blade steel (proposal)”
Forschungzentrum Jülich (2014) Germany

[Ber67]: Bernas, H.; Campbell, I.; Fruchart, R.; “Electronic exchange and the Mössbauer effect in iron-based interstitial compounds”
Journal of Physics and Chemistry of Solids (1967) Vol.28,pp. 17-24

[Bil01]: Bilmes, P.; Solari, M.; Lorente, C.; “Characteristics and effects of austenite resulting from tempering of 13Cr–NiMo martensitic steel weld metals”
Materials Characterization 46 (2001) 285-296

[Ble12]: Bleck, W. “ Materials Characterisation”;
RWTH Aachen (2012), pp.154

[Bre11]: Brent, F.; Elton, K.; “Mössbauer Spectrometry”
John Wiley (2011) New York

[Bus06]: Busch, P.; Rauscher, M.; Smilgies, M.; Posselt, D.; Papadakis, C.; “Grazing-incidence small-angle x-ray scattering (GISAXS) as a tool for the investigation of thin nanostructured block copolymer films - The scattering cross-section in the distorted wave Born approximation”
Journal Applied Crystal (2006) 39, 433-442

[Cam95]: Campbell, J.; Kaczmarek, A.; Wang, M.; “Mechanochemical transformation of haematite to magnetite”
Nanostructure Materials (1995) 6:35-738

[Cor95]: Cortie, B.; Pollak, H.; “Embrittlement and aging at 475℃ in an experimental ferritic stainless-steel containing 38 wt.% chromium”
Material Science Engineer A (1995) 199: 153-163

[Dav01]: David, R.; “Fatigue”
Massachusetts Institute of Technology (2001) Cambridge

[Dem71]: Demarest Jr, H.; Acoust, J.; “Cube - Resonance Method to Determine the Elastic Constants of Solids”
Acoustical Society of America (1971) 49, 768

[Dyn14]: Dynamic Resonant Systems;
225 Lane 13, Powell, Wyoming 82435, USA.

[Fal94]: Faldum, T.; Meisel, W.; Gütlich, P; “Oxidic and metallic Fe/Ni multilayers prepared from Langmuir-Blodgett films”
Hyperfine Interactions (1994) 92: 1263-1269

[Fan94]: Fanciulli, M.; Weyer, G.; “Conversion Electron Mossbauer Spectroscopy Study of Iron Silicide Films Grown by MBE”
Physcia Scripta (1994) Vol. T54, 16-19

[Fra62]: Frauenfelder, H.; “The Mössbauer Effect”
Benjamin (1962) New York

[Fra64]: Frazer, D.; LeCraw, R.;
Review of Scientific Instruments (1964) 36, 1113

[Gol68]: Goldanskii, V.; Herber, R.; “Chemical Applications of Mössbauer Spectroscopy”
Academic Press Inc (1968) London

[Grg04]: Grgac, P.; Moravick, R.; Kusy, M.; Toth, I.; Miglierini, M.; Illekova, E; “Thermal stability of metastable austenite in rapidly solidified chromium-molybdenum-vanadium tool steel powder”
Materials Science and Engineering (2004) A 375-377 581-584.

[Gui55]: Guinier,A.; Fournet, G.; “Small-Angle Scattering of X-rays”
John Wiley and Sons (1955) New York

[Hey90]: Heyliger, P.; Ledbetter, H.; Austin, M.; Wolfenden, A.; “Dynamic Elastic moduli Measurements in Materials”
ASTM STP 1045, American Society for Testing and Materials (1990) Philadelphia

[Hid97]: Hideji, I.; Kiyoshi, O.; “Effects of Porosity and Grain Size on the Magnetic Properties of NiZn Ferrite”
Journal of The American Ceramic Society (1997) Vol.60, No.1-2

[Hol68]: Holland,R.; Acoust, L.; “Resonant Ultrasonund Spectroscopy”
Soc. Am. 43 (1968) 988

[Ino68]: Ino, H.; “A Study of the Mössbauer Effect during the Tempering of Iron-Carbon Martensite”
Journal of the Physical Society of Japan (1968) Vol.25, No.1

[Kim88]: Kim, S.; Weertman, J.; “Investigation of Microstructural Changes in a Ferritic Steel Caused by High Temperature Fatigue”
Metallurgical Transactions A (1988) Vol.19 A, 999

[Koh97]: Kohlbrecher,J.; Wiedenmann, A.; Wollenberger, H.; “Magnetic coupling between the different phases in nanocrystalline Fe-Si-B studied by small angle neutron scattering”
Zeitschrift für Physik (1997) B 104, 1-4

[Kov12]: Kovacs,S.; Beck, T.;Singheiser, L. “Influence of mean stresses on fatigue life and damage of a turbine blade steel in the VHCF-regime”
International Journal of Fatigue (accepted for publication) (2012)

[Kre09]: Kreyssig, A.; Prozorov, R.; Dewhurst, C.; Canfield, P.; McCallum, R.; Goldman, A.; “Probing Fractal Magnetic Domains on Multiple Length Scales in $Nd_2Fe_{14}B$”
Physcial Review Letters (2009) 102, 047204

[Kru97]: Kruijer, S.; Keune, W.; Dobler, M.; Reuther, H.; “Depth analysis of phase formation in Si after high-dose Fe ion-implantation by depth-selective conversion electron Mössbauer spectroscopy”
Applied Physics Letters (1997) 70: 2696-2698

[Lar06]: Larica, C.; Mercader, R.; Partiti, C.; Gancedo, J.; Proceedings of the 10th Latin American Conference on the Applications of the Mössbauer Effect
LACAME (2006) Rio de Janeiro, Brazil

[Lev89]: Levine, J.; Cohen, J.; Chung, Y.; Georgopoulos, P.; “Grazing-incidence small-angle X-ray scattering: new tool for studying thin film growth”
Journal Applied Crystal (1989) 22, 528-532

[Lev93]: Levine, J.; Chung, Y.; Georgopoulos, P.; Cohen, J.; “GISAXS - Glancing incidence small angle X-ray scattering”
Journal Physics IV France (1993) 3-C8, 411-417

[Mey12]: Dr. Meyer, A.; “Glancing incidence small angle X-ray scattering”
Institute of Physical Chemistry (1993) University of Hamburg

[Mig97]: Migliori,A.; Sarrao, L.; “Resonant Ultrasonund Spectroscopy”
John Wiley and Sons (1997) New York

[Mor68]: Moriya, T.; “Mössbauer Effect in Iron-Carbon Martensite Structure”
Journal of the Physical Society of Japan (1968) Vol.24, No.1

[Phi11]: Philipp, G.; Eckhard, B.; Alfred, T.; “Mössbauer Spectroscopy and Transition Metal Chemistry”
Springer Heidelberg Dordrecht London New York (2011) ISBN 978-3-540-88427-9

[Pol01]: Polian, A.; Thanh, D.; Richet, P.; “Elastic properties of a-SiO_2 up to 2300 Kfrom Brillouin scattering measurements”
Europhysics Letters (2002) 57 (3), pp.375-381

[Pot88]: Potton, J.; Daniell, G.; Rainford, B.; “A New Method for the Determination of Particle Size Distributions from Small-Angle Neutron Scattering Measurements”
Journal Applied Crystal (1988) 21, 891-897

[Ron68]: Ron, M.; Shechter, H.; Niedzwidz, O.; “Precipitation of Iron Carbides in Tempered Martensite”
Journal Applied Physics (2000) Vol. 39 pp.265

[Ron71]: Ron, M.; Mathalone, Z.; “Hyperfine Interactions of 57Fe in Fe3C”
Physcial Review B (1971) Vol. 4, pp. 774-777

[Rud14]: Rudolf, M.; Wiki link
http://de.wikipedia.org/wiki/Rudolf_M%C3%B6%C3%9Fbauer, seen on 8th, September, 2014

[Rüc14]: Rücker, U.; Kentzinger, E.; Hölzle, M.; “World‘s best laboratory X-ray diffractometer for GISAXS”
Jülich Forschungszentrum (2014) Gernany

[Sch76]: Schwartz, H.; “Ferrous alloy phase transformations”
In Applications of Mössbauer Spectroscopy (1976) Vol.1. pp. 37-81

[Sei00]: Sei, O.; Soon-Jun, K.; Hongsug, O.; Sunghak, L; Keun, H; “Phase Analysis of Two Steel Work Rolls Using Mössbauer Spectroscopy”
Metallurgical and materials transiactions A (2000) Vol. 31 A

[Sei98]: Sei, J.; “Characterization of iron oxides commonly formed as corrosion products on steel”
Hyperfine Interactions (1998) 112(1): 59-66

[Sim76]: Simmons, W.; Leidheiser, H.; “Corrosion and interfacial reactions”
In Applications of Mössbauer Spectroscopy (1976) Vol.1. pp. 92-93

[Skr84]: Skrzpek, S.; Kolawa, E.; Sawicki, J.; Tyliszczak, T.; “A study of the retained austenite phase transformation in low alloy steel using conversion electron Mössbauer spectroskopy and X-ray diffraction”
Materials Science and Engineering (1984) 66 145-149.

[Smi14]: Smilgies, D.; GISAXS and GIWAXS
http://staff.chess.cornell.edu/~smilgies/gisaxs/GISAXS.php , seen on 8th, September, 2014

[Sog76]: Soga, N.; Anderson, O.; “Resonant ultrasonund spectroscopy for materials studies and non-destructive testing”
Ultrasonics (1996) 34, 473-47

[Til13]: Tilmann, B.; Stephan, K.; Lorenz, S.; “Influence of high mean stresses on lifetime and damage of the martensitic steel X10CrNiMoV12-2-2 in the

VHCF-regime”
International Conference of Fracture (2013) Beijing, China

[Var92]: Vardavoulias, M.; Papadimitriou, G.; “Mossbauer Spectra and Hyperfine Parameters of Iron- Chromium Carbides in Ferritic Stainless Steels”
Physica status solidi (a) (1992) 134, 183

[Vis91]: Visscher, W.; Migliory, A.; Bell, T.; Reinert, R.;
Journal of the Acoustical Society of America (1991) 90, 2154.

[Wan02]: Wang, Q.; Bathias, C.; Kawagoishi, N.; Chen, Q.; “Effect of inclusion on subsurface crack initiation and gigacycle fatigue strength”
International Journal of Fatigue 24 (2002) 1269-1274

[Wil09]: Willis,B.; Carlile, C.; “Experimental Neutron Scattering”
Oxford University Press (2009) Oxford

[Wil12]: William, D. C.; David, R.; “Fundamentals of Materials Science and Engineering”
4 edtion Wiley (2012) pp.252

9 List of images and tables

List of images

List of tables